ANOMALOUS HIGGS BOSON COUPLINGS IN VECTOR BOSON FUSION

A Dissertation by

Tinghua Chen

Master of Science, Wichita State University, 2018

Bachelor of Science, Emporia State University, 2016

Submitted to the Department of Mathematics, Statistics, and Physics
and the faculty of the Graduate School of
Wichita State University
in partial fulfillment of
the requirements for the degree of
Doctor of Philosophy

July 2023

ANOMALOUS HIGGS BOSON COUPLINGS IN VECTOR BOSON FUSION

The following faculty members have examined the final copy of this dissertation for form and content, and recommend that it be accepted in partial fulfillment of the requirement for the degree of Doctor of Philosophy with a major in Applied Mathematics.

Terrance Figy, Committee Chair

Holger Meyer, Committee Member

Mathew Muether, Committee Member

Thomas DeLillo, Committee Member

Sergio Salinas, Committee Member

Accepted for the Fairmount College of Liberal Arts and Sciences

Andrew Hippisley, Dean

Accepted for the Graduate School

Coleen Pugh, Dean

DEDICATION

To my parents, my wife, and my dear friends.

The Revolution is not yet done; All my Comrades must strive on.
- From Sun Yat-sen's will

ACKNOWLEDGEMENTS

I am deeply grateful to all the people who have supported and encouraged me throughout this incredible journey toward completing my Ph.D. in Applied Mathematics. Their invaluable assistance and unwavering belief in my abilities have been instrumental in making this dissertation possible. There are many people who I would like to thank for helping make this dissertation possible. First and foremost, I would like to thank my dissertation advisor, Prof. Terrance Figy, for the continued help, guidance, and wealth of knowledge throughout this project. I appreciate all your words of encouragement. I am indebted to the members of my dissertation committee, Prof. Mathew Muether, Prof. Holger Meyer, Prof. Sergio Salinas, and Prof. Thomas DeLillo. Their participation and constructive feedback have enriched my work. A special mention is reserved for Dr. Simon Plätzer. Our collaboration led to a published journal paper, which significantly contributed to a vital section of this dissertation. The support and resources provided by BeoShock [1] and Beocat [2] have been invaluable in facilitating my research. I extend my gratitude to the Department of Mathematics, Statistics, and Physics for fostering a stimulating academic environment. I would also like to acknowledge the financial support received from the Department of Mathematics, Statistics, and Physics and BeoShock HPC, which has played a crucial role in enabling me to carry out my research. Thank you all for being an integral part of this unforgettable chapter in my life.

ABSTRACT

The discovery of the Higgs boson at the Large Hadron Collider (LHC) in 2012 marked a significant milestone in particle physics. Since then, extensive investigations have been carried out to unravel the properties of the Higgs boson and understand its interactions with other fundamental particles.

Monte Carlo simulations play an important role in studies of particle physics. They generate theoretical predictions and can be compared with experimental data to test our understanding of physics.

In this dissertation, the anomalous Higgs boson coupling to vector bosons was implemented in `VBFNLO` for Higgs boson plus three jets via VBF at the next-to-leading order (NLO) accuracy. I present results for a number of collider observables that are sensitive to the CP structure, whether in different CP scenarios and in the Standard Model. I also investigate the effects of NLO multijet merging and NLO QCD corrections matched to a parton shower on selected observables through the framework provided by Herwig 7.

TABLE OF CONTENTS

Chapter Page

TABLE OF CONTENTS (continued)

Chapter Page

LIST OF TABLES

LIST OF FIGURES

Figure Page

LIST OF FIGURES (continued)

Figure Page

LIST OF FIGURES (continued)

Figure Page

LIST OF SYMBOLS

p_T	Transverse Momentum
y	Rapidity
$\Delta y_{j_1 j_2}$	Rapidity Gap between Jet 1 and Jet 2
$m_{j_1 j_2}$	Invariant Mass of Jet 1 and Jet 2
$\Delta\phi_{j_f j_b}$	Azimuthal Angle Difference Between Forward Jet and Backward Jet
$\lvert\Delta\phi_{j_1 j_2}\rvert$	Absoulte Value of Azimuthal Angle Difference Between Jet 1 and Jet 2
$g^{\mu\nu}$	Metric Tensor
$\sqrt{s}$	Center-of-mass Energy
Γ	Decay Rate
σ	Cross Section
E	Energy of a Particle

CHAPTER 1
INTRODUCTION

The quest to unravel the fundamental mysteries of the universe has captivated the human intellect for centuries. In this pursuit, particle physicists have made groundbreaking discoveries that have significantly advanced our understanding of the fundamental building blocks of matter and the forces that govern their interactions. The Standard Model (SM) [6–8] of particle physics was developed in the seventies in the past century, has successfully explained most of the experimental results and also precisely predicted a variety of phenomena in particle physics [9]. Among these remarkable discoveries, the identification and subsequent verification of the Higgs boson have emerged as one of the most pivotal achievements in recent years. The Higgs boson was proposed by Peter Higgs [10] and François Englert [11] in 1964, providing a mechanism to explain the origin of mass and the spontaneous breaking of electroweak symmetry. On 4 July 2012, both ATLAS and CMS experiments at CERN's Large Hadron Collider (LHC) announced they had each observed a new particle in the mass region around 125 GeV- 126 GeV [12, 13]. In the following year, after analyzing two and a half times more data, physicists confirmed that the new particle discovered was the Higgs boson [14]. In the current measurement of the Higgs boson production by ATLAS Run 2 [3], the VBF cross section is measured with a precision of 12%, and the gluon fusion process is measured with a precision of 7%. The other production processes include WH, ZH, ttH, and tH have also been observed. The results are shown on the left of Fig. 1.1. The branching fractions of the different Higgs boson decay modes are measured with a precision ranging from 10% to 12%, and the results are shown in Fig. 1.1 (right). The results of the current measurements are compatible with the predictions of the SM.

While the present measurements on properties of the Higgs boson exhibit compatibility with the predictions of the SM [15], the precision of the experiment is not sufficient to exclude the possibility of anomalous couplings, which leaves room for new

physics (NP) resulting in modified Higgs couplings with the SM particles. For example, the SM does not explain the baryon asymmetry problem. It refers to a reasonable assumption that matter and antimatter were initially present in equal quantities during the early stages of the universe [16]. However, our everyday experience solely involves interactions with matter, not antimatter [17]. The baryon asymmetry problem leads to the study of CP violation [18]. Higgs boson production through vector boson fusion (VBF) is an ideal process to test CP violations. In the case of CP symmetry conservation, the behavior patterns of detected jets and leptons remain unchanged when particles are exchanged with their antiparticles and their flight directions are reversed. Conversely, if CP symmetry is violated, particles and antiparticles should behave differently.

The anomalous Higgs boson coupling via VBF can be derived from the effective field theory approach and the corresponding anomalous couplings have been implemented in `VBFNLO` [19–22], which is a Monte Carlo program, at the next-to-leading order (NLO) quantum chromodynamics (QCD) accuracy [23]. The NLO matched parton shower effects for VBF have been investigated in Ref. [24] by implementing the Higgs Characterisation (HC) model [25] in `FEYNRULES` [26, 27] and passed to `MADGRAPH5_AMC@NLO` framework [27]. In order to study the higher-order effects and multiplicities of jets, one needs to calculate the matrix elements for the Higgs boson plus three jets at NLO accuracy. In this dissertation, anomalous Higgs couplings for HVV ($V = W, Z$) vertex are studied and implemented in the Monte Carlo program, `VBFNLO`, for Higgs production plus three jets at NLO. The general-purpose Monte Carlo event generator, Herwig 7 [28–31] which is interfaced with `VBFNLO` as one of the matrix element providers via the Binoth one-loop accord [32, 33] provided the numerical computation tool for this study. By utilizing the matching and merging framework provided by the Herwig 7, the phenomenological results are presented for Higgs boson production in SM and anomalous couplings via the VBF.

The layout of this dissertation is the following: Chapter 2 sets the stage for theoretical background, introduces the model-building ingredients of the SM, and gives the

general description of NLO QCD calculations on parton-level at hadron colliders, including the Catani-Seymour subtraction method [34] using in the NLO calculation. Chapter 3 discussed the merged and matched framework in Herwig 7 and contains results from Ref. [35]. In Chapter 4, the HVV anomalous couplings and technical details of the implementation in `VBFNLO` are presented. Subsequently, the discussion of the validation and numerical checks of the code is performed in Chapter 5. Chapter 6 is devoted to the phenomenological study of the Higgs boson plus two jets using the matching and merging framework. Finally, Chapter 7 closes with a conclusion and future study of this dissertation.

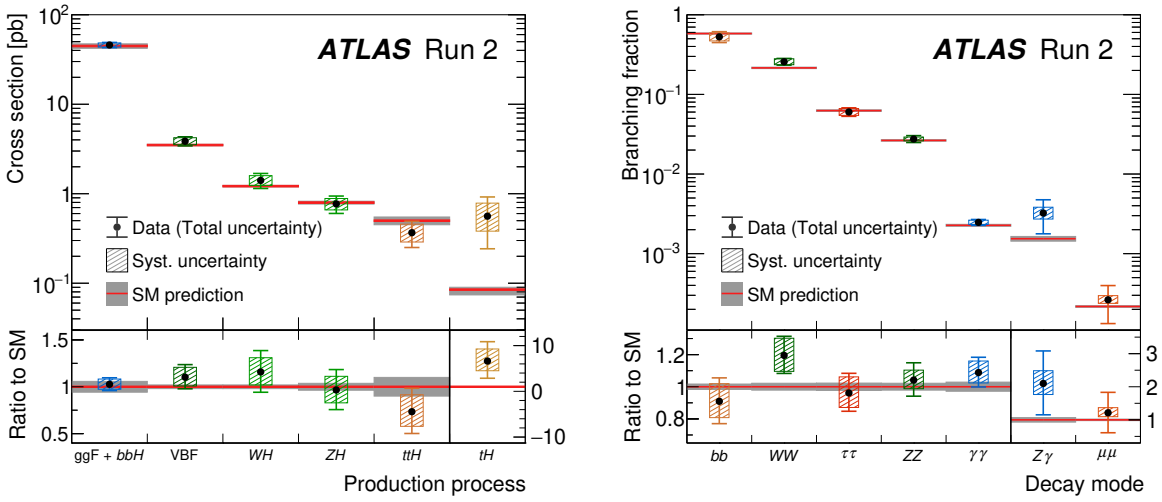

Figure 1.1: Cross sections for different Higgs boson production processes (left) and branching fractions for different Higgs boson decay modes (right). The lower panels show the ratios of the measured values to their SM predictions. The vertical bar on each point shows the 68% confidence interval. The vertical bar on each point shows the 68% confidence interval. Figure from Ref. [3].

CHAPTER 2
THE THEORETICAL BACKGROUND

This chapter presents a short overview of the theoretical basis of the dissertation. I start with a brief introduction of the SM decomposed into its two interaction sectors: Electroweak and QCD. Much of this chapter's notation is taken from the book " The Black Book of Quantum Chromodynamics" [36] by Frank Krauss, Joey Huston, and John Campbell, which I highly recommend. After that, the calculation of leading order (LO) and NLO and the related concepts are introduced. A brief discussion of the Catani-Seymour subtraction method [34] is appended.

2.1 The Standard Model

The Standard Model of particle physics is a remarkable theoretical framework that describes the fundamental building blocks of the universe and the forces that govern their interactions. It provides a comprehensive understanding of the subatomic world by unifying three of the four known fundamental forces: the electromagnetic force, the weak nuclear force, and the strong nuclear force. The construction of the SM relies on the gauge invariance and can be described with the gauge symmetry groups $SU(3)_c \times SU(2)_L \times U(1)_Y$ [7, 8, 37], where the $SU(3)_c$ is the gauge group of Quantum Chromodynamics (QCD) which is, and $SU(2)_L \times U(1)_Y$ the gauge group of electroweak (EW) interactions. Besides the Higgs boson, the particle content of the SM can be split into gauge bosons, mediating the interactions, and fermions, which make up the matter content of the SM and themselves are divided into color-charged quarks and colorless leptons.

2.1.1 The Standard Model Before Electroweak Symmetry Breaking

The electromagnetic and weak interactions between quarks and leptons are described by the Glashow-Weinberg-Salam electroweak theory [7, 8, 37], which is a Yang-Mills theory [38] based on the symmetry group $SU(2)_L \times U(1)_Y$. The matter field has three generations of left-handed and right-handed chiral fermions, carry spin $\frac{1}{2}$ and

with the field components, $\psi_{L,R} = \frac{1}{2}(1 \mp \gamma_5)\psi$. The quantum number conserved corresponding to $SU(2)_L$ is weak isospin T_3. The electric charge Q can be computed from the weak quantum numbers according to

$$Q = T_3 + \frac{Y}{2}, \tag{2.1}$$

where Y is the weak hypercharge quantum number associated with gauge group $U(1)_Y$. The fermions with right-handed chirality are in doublets, while the fermions with left-handed chirality are in singlets,

$$\begin{aligned}
&L^{(1)}_{L,i} = \begin{pmatrix} \nu_e \\ e \end{pmatrix}_{L,i}, \quad L^{(2)}_{L,i} = \begin{pmatrix} \nu_\mu \\ \mu \end{pmatrix}_{L,i}, \quad L^{(3)}_{L,i} = \begin{pmatrix} \nu_\tau \\ \tau \end{pmatrix}_{L,i}; \\
&Q^{(1)}_{L,i} = \begin{pmatrix} u \\ d \end{pmatrix}_{L,i}, \quad Q^{(2)}_{L,i} = \begin{pmatrix} c \\ s \end{pmatrix}_{L,i}, \quad Q^{(3)}_{L,i} = \begin{pmatrix} t \\ b \end{pmatrix}_{L,i}; \\
&u^{(1)}_{R,i} = u_{R,i}, \quad u^{(2)}_{R,i} = c_{R,i}, \quad u^{(3)}_{R,i} = t_{R,i}; \\
&d^{(1)}_{R,i} = d_{R,i}, \quad d^{(2)}_{R,i} = s_{R,i}, \quad d^{(3)}_{R,i} = b_{R,i}; \\
&l^{(1)}_{R,i} = e_{R,i}, \quad l^{(2)}_{R,i} = \mu_{R,i}, \quad l^{(3)}_{R,i} = \tau_{R,i};
\end{aligned} \tag{2.2}$$

where i represents the color charge in the fundamental representations, and the number superscript represents different generations of fermions. The assignment of the quantum numbers to the fermions is shown in Tab. 1, for the fermions of the first generation, which second and third generation fermions have identical quantum numbers [39–41].

Table 1: The electroweak quantum numbers for the first generation fermions.

	T_3	Y	Q
ν_{eL}	$\frac{1}{2}$	-1	0
e_L	$-\frac{1}{2}$	-1	-1
u_L	$\frac{1}{2}$	$\frac{1}{3}$	$\frac{2}{3}$
d_L	$-\frac{1}{2}$	$\frac{1}{3}$	$-\frac{1}{3}$
e_R	0	-2	1
u_R	0	$\frac{4}{3}$	$\frac{2}{3}$
d_R	0	$-\frac{2}{3}$	$-\frac{1}{3}$

The gauge invariant derivatives on the fermions are given by

$$
\begin{aligned}
D_\mu Q^{(I)}_{L,i,\alpha} &= \Big(\partial_\mu + ig_s\frac{\lambda^a_{ij}}{2}G^a_\mu\delta_{\alpha\beta} + ig_2\frac{\sigma^a_{\alpha\beta}}{2}W^a_\mu\delta_{ij} + ig_1\frac{Y}{2}B_\mu\delta_{ij}\delta_{\alpha\beta}\Big)Q^{(I)}_{L,j,\beta} \\
D_\mu u^{(I)}_{R,i} &= \Big(\partial_\mu + ig_s\frac{\lambda^a_{ij}}{2}G^a_\mu + ig_1\frac{Y}{2}B_\mu\delta_{ij}\Big)u^{(I)}_{R,j} \\
D_\mu d^{(I)}_{R,i} &= \Big(\partial_\mu + ig_s\frac{\lambda^a_{ij}}{2}G^a_\mu + ig_1\frac{Y}{2}B_\mu\delta_{ij}\Big)d^{(I)}_{R,j} \\
D_\mu L^{(I)}_{L,\alpha} &= \Big(\partial_\mu + ig_s\frac{\sigma^a_{\alpha\beta}}{2}W^a_\mu + ig_1\frac{Y}{2}B_\mu\delta_{\alpha\beta}\Big)L^{(I)}_{L,\beta} \\
D_\mu l^{(I)}_R &= \Big(\partial_\mu + ig_1\frac{Y}{2}B_\mu\Big)l^{(I)}_R,
\end{aligned}
\tag{2.3}
$$

where i and j is the color indices, α and β are weak isospin indices. The λ are Gell-Mann matrices, which are explicitly shown in Eq. 2.46. σ are the Pauli matrices which are explicitly shown in Eq. 2.5. Here g_s,g_2, and g_1 are the coupling constant of $SU(3)_C$, $SU(2)_L$, and $U(1)_Y$, respectively. The gauge field indicates there are eight gluons G^a_μ, three weak isospin bosons W^a_μ, and the weak hypercharge B_μ. The gauge field B_μ corresponds to $U(1)_Y$ group with generator Y. For $SU(2)_L$ group, there are three gauge field $W^a_{\mu\nu}$ with the

generators τ_a, where $a = 1, 2, 3$. The generators τ_a are given by half of the Pauli matrices,

$$\tau_a = \frac{1}{2}\sigma_a, \tag{2.4}$$

$$\sigma_1 = \begin{pmatrix} 0 & 1 \\ 1 & 0 \end{pmatrix}, \quad \sigma_2 = \begin{pmatrix} 0 & -i \\ i & 0 \end{pmatrix}, \quad \sigma_3 = \begin{pmatrix} 1 & 0 \\ 0 & -1 \end{pmatrix}, \tag{2.5}$$

and the commutation relation is given by,

$$[\sigma_a, \sigma_b] = i\epsilon_{abc}\sigma_c. \tag{2.6}$$

Here ϵ_{abc} is the completely anti-symmetric Levi-Civita symbol.

The SM Lagrangian without mass terms for fermions and gauge bosons is given by

$$\mathcal{L}_{\text{SM}} = \mathcal{L}_{\text{matter}} + \mathcal{L}_{\text{gauge}} \tag{2.7}$$

where

$$\mathcal{L}_{\text{matter}} = \sum_{I=1}^{3} \left[\bar{Q}_L^{(I)} \not{D} Q_L^{(I)} + \bar{u}_R^{(I)} \not{D} u_R^{(I)} + \bar{d}_R^{(I)} \not{D} d_R^{(I)} + \bar{L}_L^{(I)} \not{D} L_L^{(I)} + \bar{l}_R^{(I)} \not{D} l_R^{(I)} \right], \tag{2.8}$$

$$\mathcal{L}_{\text{guage}} = -\frac{1}{4} G^a_{\mu\nu} G^{a,\mu\nu} - \frac{1}{4} W^a_{\mu\nu} W^{a,\mu\nu} - \frac{1}{4} B^a_{\mu\nu} B^{\mu\nu} \tag{2.9}$$

The field strength tensors are given by,

$$G^a_{\mu\nu} = \partial_\mu G^a_\nu - \partial_\nu G^a_\mu + i g_s f^{abc} G^b_\mu G^c_\nu, \tag{2.10}$$

$$W^a_{\mu\nu} = \partial_\mu W^a_\nu - \partial_\nu W^a_\mu + g_2 \epsilon^{abc} W^b_\mu G^c_\nu, \tag{2.11}$$

$$B_{\mu\nu} = \partial_\mu B_\nu - \partial_\nu B_\mu. \tag{2.12}$$

This Lagrangian is invariant under the local $SU(3)_C \times SU(2)_L \times U(1)_Y$ gauge transformations but violates the gauge invariance if one adds the mass term of form $m^2 A^2$.

For example,

$$B_\mu B^\mu \to B'_\mu B'^\mu = B_\mu B^\mu \frac{2}{g} B^\mu \partial_\mu \theta + \frac{1}{g^2}(\partial_\mu \theta)(\partial^\mu \theta) \neq B_\mu B^\mu \tag{2.13}$$

In addition, if one includes explicitly a mass term $m\bar{\psi}\psi$ for fermions in Lagrangian, for example [40],

$$-m_e \bar{e} e = -m_e \bar{e}\Big[\frac{1}{2}(1-\gamma_5) + \frac{1}{2}(1+\gamma_5)\Big] e = -m_e(\bar{e}_R e_L + \bar{e}_L e_R) \tag{2.14}$$

is not invariant under the weak isospin symmetry transformation since e_L is a member of an $SU(2)_L$ doublet but e_R is a member of a singlet. The Feynman rules for gauge bosons interacting with fermions are shown in Fig. 2.1, where the chirality $\tau = \pm$.

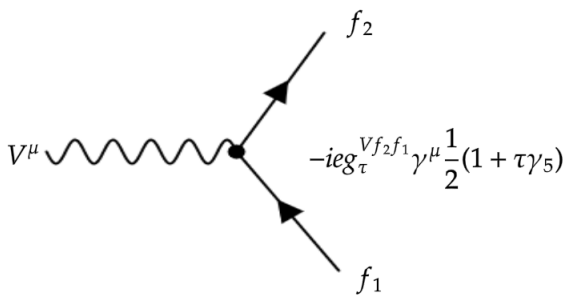

Figure 2.1: qqV vertex for fermions and gauge bosons.

In the following sections, I will briefly sketch the spontaneous symmetry breaking and the Higgs mechanism, which solve the problem of gauge invariant mass generation in an elegant way.

2.1.2 Spontaneous Symmetry Breaking

Consider the Lagrangian,

$$\mathcal{L} = \frac{1}{2}(\partial_\mu \phi)^2 - (\frac{1}{2}\mu^2\phi^2 + \frac{1}{4}\lambda\phi^4), \tag{2.15}$$

where λ is a constant and $\lambda > 0$ [42]. The $\mathcal{L}$ is invariant under the transformation $\phi \to -\phi$. If one plots the graph of potential $V(\phi) = \frac{1}{2}\mu^2\phi^2 + \frac{1}{4}\lambda\phi^4$, there will be two possibilities : $\mu^2 > 0$ and $\mu^2 < 0$. If $\mu^2 < 0$, the Lagrangian has the wrong sign for the mass term. Unlike the case in which $\mu^2 > 0$, the potential has two minima that satisfies [42],

$$\frac{\partial V}{\partial \phi} = \phi(\mu^2 + \lambda\phi^2) = 0, \tag{2.16}$$

where

$$\phi_{min} = \pm v, \tag{2.17}$$

and $v = \sqrt{-\mu^2/\lambda}$. In this case, the minimum energy is not at $\phi = 0$. It corresponds to $\phi = v$ or $\phi = -v$. One could rewrite $\phi(x)$ as

$$\phi(x) = v + \eta(x), \tag{2.18}$$

where $\eta(x)$ represents the quantum fluctuations about this minimum. Substituting into Lagrangian equation (2.15),

$$\mathcal{L}' = \frac{1}{2}(\partial_\mu \eta)^2 - \lambda v^2\eta^2 - \lambda v\eta^3 - \frac{1}{4}\lambda\eta^4 + const. \tag{2.19}$$

so the mass term is $m_\eta = \sqrt{2\lambda v^2} = \sqrt{-2\mu^2}$ and the higher order terms of η represent the interaction of the couplings [42]. The way to "generate" mass through the field is known as "spontaneous symmetry breaking."

2.1.3 The Higgs Mechanism

Let's first introduce a complex scalar $\Phi = (\phi^+, \phi^0)^T$, which is coupled to the $SU(2)_L \times U(1)$ through the gauge invariant derivative $D_\mu \Phi_\beta$. The $D_\mu \Phi_\beta$ reads [36]

$$D_\mu \Phi_\beta = (\partial_\mu \delta_{\alpha\beta} + i g_2 \frac{\sigma^\alpha_{\alpha\beta}}{2} W^\alpha_\mu + i g_1 \frac{Y}{2} B_\mu \delta_{\alpha\beta}) \Phi_\beta, \tag{2.20}$$

where α and β labels weak isospin of the doublet Φ. The quantum numbers of this doublet, Φ, are:

$$T_3 = \pm \frac{1}{2}, \quad Y = \frac{1}{2}. \tag{2.21}$$

Then there are two new terms added to the Lagrangian in Eq. 2.7:

$$\mathcal{L}_H = (D_\mu \Phi)^\dagger (D^\mu \Phi) + \mu^2 \Phi^\dagger \Phi - \lambda (\Phi^\dagger \Phi)^2, \tag{2.22}$$

$$\mathcal{L}_{HF} = -f_u^{IJ} \bar{Q}_L^{(I)} \tilde{\Phi} u_R^J - f_d^{IJ} \bar{Q}_L^{(I)} \Phi d_R^J - f_e^{IJ} \bar{L}_L^{(I)} \Phi l_R^J, \tag{2.23}$$

where $\mathcal{L}_{HF}$ describes the Yukawa interactions with fermions. Here μ^2 and λ are real numbers, and f^{IJ} are arbitrary matrices in generation space. For $\mu^2 < 0$, a vacuum expectation value v will be developed by the neutral component of the field Φ,

$$\langle \Phi \rangle_0 = \begin{pmatrix} 0 \\ \frac{v}{\sqrt{2}} \end{pmatrix}. \tag{2.24}$$

For simplicity, by choosing the unitary gauge, the Higgs doublet then becomes,

$$\Phi_{\text{unitary}} = U(\xi)\Phi = \begin{pmatrix} 0 \\ \frac{v+\eta(x)}{\sqrt{2}} \end{pmatrix}. \tag{2.25}$$

The set of transformations is introduced as

$$\Big(\sum_{i=\pm,3} W_\mu^i \tau^i\Big)' = U(\xi)\Big[\sum_{i=\pm,3} W_\mu^i \tau^i\Big]U^{-1}(\xi) + \frac{i}{g_2}\Big[\partial_\mu U(\xi)\Big]U^{-1}(\xi),$$
$$B'_\mu = B_\mu,$$
$$\Psi'_L = U(\xi)\Psi_L,$$
$$\Psi'_R = U(\xi)\Psi_R. \tag{2.26}$$

It is clear that the Higgs potential is invariant under such transformation, and the phase will be canceled out,

$$(\Phi^\dagger\Phi) \to (\Phi^\dagger\Phi) = \Phi^\dagger U^\dagger(\xi)U(\xi)\Phi = (\Phi^\dagger\Phi). \tag{2.27}$$

Therefore, after the transformation, the Higgs potential reads,

$$\mathcal{L}_{\text{H.pot}} = -\frac{2\lambda v^2}{2}\eta^2 - \lambda v\eta^3 - \frac{\lambda}{4}\eta^4 + \text{const}, \tag{2.28}$$

where the η is the Higgs field. While this field gives the mass term of

$$m_H = v\sqrt{2\lambda}. \tag{2.29}$$

The kinematic Lagrangian reads,

$$\mathcal{L}_\eta = \frac{1}{2}(\partial_\mu\eta)(\partial^\mu\eta), \tag{2.30}$$
$$\mathcal{L}_M = m_W^2 W_\mu^- W^{+,\mu} + \frac{1}{2}m_Z^2 Z_\mu Z^\mu, \tag{2.31}$$
$$\mathcal{L}_I = \frac{m_W^2}{v^2}(\eta^2 + 2v\eta)W_\mu^- W^{+,\mu} + \frac{m_Z^2}{2v^2}(\eta^2 + 2v\eta)Z_\mu Z^\mu. \tag{2.32}$$

The new gauge filed A_μ and Z_μ for photon and Z boson is given by

$$A_\mu = \sin\theta_W W_\mu^3 + \cos\theta_W B_\mu, \tag{2.33}$$

$$Z_\mu = \cos\theta_W W_\mu^3 - \sin\theta_W B_\mu \tag{2.34}$$

It can be shown that the photon is massless, and the mass of W and Z gauge bosons is

$$m_W = \frac{v g_2}{2}, \tag{2.35}$$

$$m_Z = \frac{v}{2}\sqrt{g_1^2 + g_2^2}. \tag{2.36}$$

And the weak mixing angle is

$$\tan\theta_W = \frac{g_1}{g_2}, \tag{2.37}$$

$$\cos\theta_W = \frac{m_W}{m_Z} = \frac{g_2}{\sqrt{g_1^2 + g_2^2}}. \tag{2.38}$$

The Feynman rule for HVV vertex is shown in Fig. 2.2, where V represents vector bosons, W and Z.

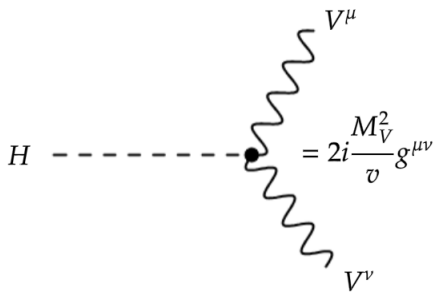

Figure 2.2: Feynman rules for HVV vertex.

After applying the transformation to the Yukawa interaction, as shown in Eq. 2.26,

the fields become

$$\mathcal{L}_{HF} = \frac{v+\eta}{\sqrt{2}}\Big[f_u^{IJ}\bar{u}_L^{(I)}u_R^{(J)} + f_d^{IJ}\bar{d}_L^{(I)}d_R^{(J)} + f_l^{IJ}\bar{l}_L^{(I)}l_R^{(J)}\Big]. \tag{2.39}$$

The arbitrary mass matrices $f_{u,d,l}^{IJ}$ which are denoted as M for simplicity, can be diagonalized using the bi-unitary transformation,

$$M_{\text{diag}} = S^\dagger M T, \tag{2.40}$$

where S and T are unitary matrices and M_{diag} is diagonal with non-zero eigenvalues. Then the mass term can be diagonalized through

$$\bar{\psi}_L M \psi_R = (\bar{\psi}_L S)(S^\dagger M T)(T^\dagger \psi_R) = \bar{\psi}'_L M_{\text{diag}} \psi'_R \tag{2.41}$$

The unitary transformation will rotate the right-handed quarks to their mass eigenstates,

$$\bar{\psi}_R^I \gamma^\mu \psi_R^I = \bar{\psi}_R'^K \gamma^\mu T_{KI} T^\dagger_{IL} \psi_R'^L = \bar{\psi}_R'^K \gamma^\mu \delta_{KL} \psi_R'^L = \bar{\psi}_R'^K \gamma^\mu \psi_R'^K. \tag{2.42}$$

This also applies to the left-handed fermions for neutral interactions, but there is relic dependence in the charged current, which is expressed in terms of the Cabibbo-Kobayashi-Maskawa (CKM) matrix,

$$\bar{u}_L^I \gamma^\mu d_L^I = \bar{u}_L'^K \gamma^\mu S^\dagger_{u,KI} S_{d,IL} d_L'^L = \bar{u}_L'^K \gamma^\mu V_{KL}^{(\text{CKM})} d_L'^L, \tag{2.43}$$

where the absolute value of the CKM matrix read [4]

$$V_{KL}^{(\mathrm{CKM})} = \begin{pmatrix} V_{ud} & V_{us} & V_{ub} \\ V_{cd} & V_{cs} & V_{cb} \\ V_{td} & V_{ts} & V_{tb} \end{pmatrix} = \begin{pmatrix} 0.97435 \pm 0.0001 & 0.22500 \pm 0.0006 & 0.00369 \pm 0.0001 \\ 0.22486 \pm 0.00067 & 0.97349 \pm 0.00016 & 0.04182^{+0.00085}_{-0.0007} \\ 0.00857^{+0.00020}_{-0.00018} & 0.04110^{+0.00083}_{-0.00072} & 0.999118^{+0.000031}_{-0.00003} \end{pmatrix}. \tag{2.44}$$

In the `VBFNLO`, the CKM matrix is taken to be diagonal in the calculations.

2.1.4 Quantum Chromodynamics

Quantum Chromodynamics is the gauge field theory that describes the strong interactions of colored quarks and gluons. It obeys the $SU(3)$ non-abelian gauge invariance, in which $SU(3)$ is the special unitary group in 3 dimensions, and all elements are the set of unitary 3×3 matrices with determinant equal to one [4, 36, 43, 44]. The QCD Lagrangian is given by

$$\mathcal{L} = \sum_q \bar{\psi}_{q,a}(i\gamma^\mu \partial_\mu \delta_{ab} - g_s \gamma^\mu t^C_{AB} A^C_\mu - m_q \delta_{ab})\psi_{q,b} - \frac{1}{4} F^A_{\mu\nu} F^{A\mu\nu}, \tag{2.45}$$

where γ^μ are the Dirac γ matrices, $\psi_{q,a}$ are quark-filed spinors for quark with flavor q and mass m_q. The color index a runs from 1 to 3, also denoted as red, green, blue, and green, which are carried by quarks. The anti-quarks carry the anti-color quantum numbers. The sum over q in Lagrangian runs over the different quark flavors. The A^C_μ corresponds to the gluon fields with color index C runs from 1 to 8. t^C_{ab} denoted as eight generators of the

$SU(3)$ group and proportional to Hermitian and traceless Gell-Mann matrices λ^a,

$$\lambda_1 = \begin{pmatrix} 0 & 1 & 0 \\ 1 & 0 & 0 \\ 0 & 0 & 0 \end{pmatrix}, \lambda_2 = \begin{pmatrix} 0 & -i & 0 \\ i & 0 & 0 \\ 0 & 0 & 0 \end{pmatrix}, \lambda_3 = \begin{pmatrix} 1 & 0 & 0 \\ 0 & -1 & 0 \\ 0 & 0 & 0 \end{pmatrix}, \lambda_4 = \begin{pmatrix} 0 & 0 & 1 \\ 0 & 0 & 0 \\ 1 & 0 & 0 \end{pmatrix},$$
$$\lambda_5 = \begin{pmatrix} 0 & 0 & -i \\ 0 & 0 & 0 \\ i & 0 & 0 \end{pmatrix}, \lambda_6 = \begin{pmatrix} 0 & 0 & 0 \\ 0 & 0 & 1 \\ 0 & 1 & 0 \end{pmatrix}, \lambda_7 = \begin{pmatrix} 0 & 0 & 0 \\ 0 & 0 & -i \\ 0 & i & 0 \end{pmatrix}, \lambda_8 = \frac{1}{\sqrt{3}} \begin{pmatrix} 1 & 0 & 0 \\ 0 & 1 & 0 \\ 0 & 0 & -2 \end{pmatrix}. \quad (2.46)$$

Here λ also satisfies the commutation relation,

$$[\lambda_A, \lambda_B] = i f_{ABC} \lambda_C. \quad (2.47)$$

The f_{ABC} are the structure constants of $SU(3)$ and given by

$$\begin{aligned} & f_{123} = 1, \\ & f_{147} = f_{165} = f_{246} = f_{257} = f_{345} = f_{376} = \frac{1}{2}, \\ & f_{458} = f_{678} = \frac{\sqrt{3}}{2}. \end{aligned} \quad (2.48)$$

The quantity g_s is the QCD coupling constant. The filed tensor $F^A_{\mu\nu}$ is

$$F^A_{\mu\nu} = \partial_\mu A^A_\nu - \partial_\nu A^A_\mu - g_s f_{ABC} A^B_\mu A^C_\nu. \quad (2.49)$$

Some useful color algebra relations are,

$$t^A_{ab} t^A_{ab} = C_F \delta_{ac}, \quad (2.50)$$

$$f_{ACD} f_{BCD} = C_A \delta_{AB}, \quad (2.51)$$

$$t^A_{ab} t^A_{ab} = T_R \delta_{AB}, \quad (2.52)$$

where

$$C_F = \frac{N_C^2 - 1}{2N_C} = \frac{4}{3}, \tag{2.53}$$

$$C_A = N_C = 3, \tag{2.54}$$

$$T_R = \frac{1}{2}. \tag{2.55}$$

Here C_F is the Casimir color factor associated with gluon emission from a quark, C_A is the color factor associated with gluon emission from a gluon, T_R is the color factor associated with a gluon split to quark anti-quark pair. The Feynman rule for gluon interaction with quarks is shown in Fig. 2.3, where a, b, and c are color indices.

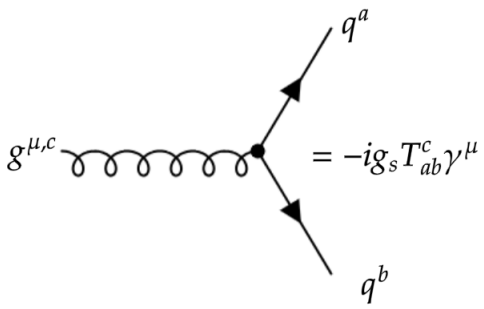

Figure 2.3: Feynman rules for gluon interacts with quarks.

When making predictions in the framework of QCD, the observables are expressed in terms of the renormalized coupling $\alpha_s(\mu_R^2 \approx Q^2)$, where μ_R is the renormalization scale introduced during the renormalization process. The coupling satisfies the following equation [4],

$$\mu_R^2 \frac{d\alpha_s}{d\mu_R^2} = \beta(\alpha_s) = -(b_0\alpha_s^2 + b_1\alpha_s^3 + b_2\alpha_s^4 + \cdots), \tag{2.56}$$

where

$$
\begin{aligned}
b_0 &= \frac{33 - 2n_f}{12\pi}, \\
b_1 &= \frac{17C_A^2 - n_f T_R(10C_A + 6C_F)}{24\pi^2} = \frac{153 - 19n_f}{24\pi^2}, \\
b_2 &= \frac{2857 - \frac{5033}{9}n_f + \frac{325}{27}n_f^2}{128\pi^3}.
\end{aligned} \tag{2.57}
$$

Here b_0 is denoted as the 1-loop β function coefficient, b_1 is the 2-loop β function coefficient, and b_3 is the 3-loop β function coefficient. The n_f is the number of quark flavors, which is 6 in the SM. The value of strong coupling is usually specified by giving the reference scale Q^2, then to the first order accuracy [36],

$$
\alpha_s(Q^2) = \alpha_s(Q^2)\frac{1}{1 + b_0\alpha_s(Q^2)\ln\frac{\mu_R^2}{Q^2}}. \tag{2.58}
$$

The negative sign of the Eq. 2.56, combined with $b_0 > 0$, is the origin of the asymptotic freedom [45, 46], which the strong coupling increases with increasing distance or decreasing scale and decreases with the decreasing distance or increasing scale. As $Q^2 \to \infty$, α_s goes to zero, which means that quarks and gluons almost interact as free particles for high energy. In the other direction, as $Q^2 \to 0$, α_s goes to infinity. One could write the solution involving another scale Λ,

$$
\alpha_s(\mu_R^2) = \frac{4\pi}{\beta_0 \ln\frac{Q^2}{\Lambda^2}}\Big[1 - \frac{2\beta_1}{\beta_0^2}\frac{\ln[\ln(Q^2/\Lambda^2)]}{\ln(Q^2/\Lambda^2)}\Big]. \tag{2.59}
$$

where $\Lambda \approx 250$ GeV is called the QCD scale. A standard choice is $\mu_R = M_Z$, the strong coupling is $\alpha_s \approx 0.118$ [4]. A summary plot of measurements of α_s as a function of Q is shown in Fig. 2.4 [4].

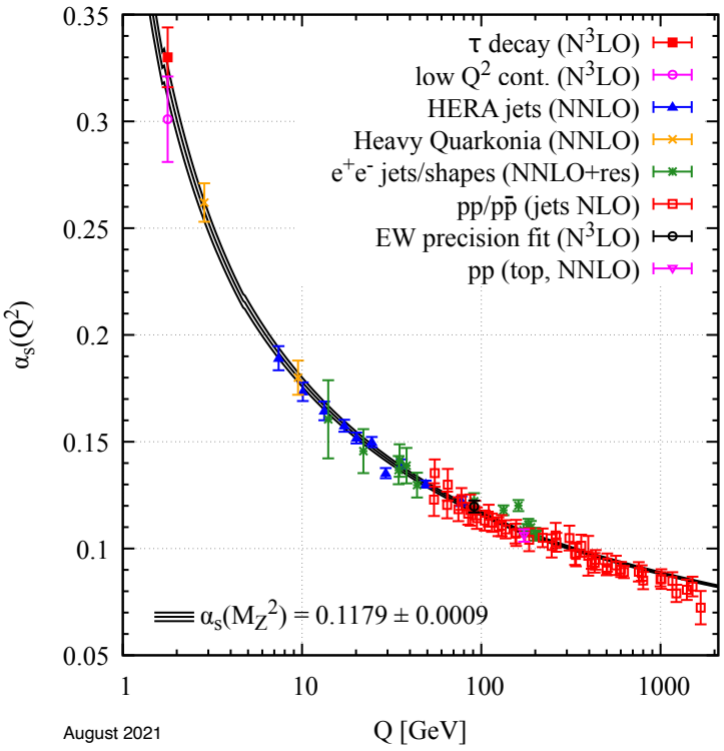

Figure 2.4: Summary of measurements of α_s as a function of the energy scale Q. NNLO represents next-to-next-to-leading order, NNLO+res represents NNLO matched to a resummed calculation, and N3LO represents next-to-NNLO. Figure taken from Ref. [4].

2.2 Factorization Formula for QCD Cross Sections

Many processes of interest involve large invariant momentum transfer that can be described using the factorization formula. Cross sections for a scattering subprocess of n body final state at hadron colliders can be computed in collinear factorization through [36, 47]

$$\begin{aligned}\sigma_{h_1h_2\to n} &= \sum_{a,b}\int_0^1 dx_a dx_b \int f_{a/h_1}(x_a,\mu_F) f_{b/h_2}(x_b,\mu_F)\, d\hat{\sigma}_{ab\to n}(\mu_F,\mu_R) \qquad (2.60)\\ &= \sum_{a,b}\int_0^1 dx_a dx_b \int d\Phi_n\, f_{a/h_1}(x_a,\mu_F) f_{b/h_2}(x_b,\mu_F)\\ &\qquad \times \frac{1}{2\hat{s}}|\mathcal{M}_{ab\to n}|^2(\Phi_n;\mu_F,\mu_R)\,,\end{aligned}$$

where $f_{a/h}(x,\mu)$ denote the parton distribution functions (PDFs). At the leading order they represent the probability for resolving a parton of flavor a with momentum fraction x in the parent hadron h at the factorization scale μ_F [48]. Here parton a and b are taken as massless particles. $\hat{\sigma}_{ab\to n}$ is the parton-level cross section for initial partons a and b product final state n. It depends on the momenta given by the final-state phase space Φ_n, factorization scale μ_F and renormalization scale μ_R. The $|\mathcal{M}_{ab\to n}|^2(\Phi_n;\mu_F,\mu_R)$ is amplitude squared, which can be evaluated as a square of sum over sub-amplitudes corresponding to subprocesses [49]. $d\Phi_n$ is the differential phase space element over the n final-state particles,

$$d\Phi_n = \prod_{i=1}^{n} \frac{d^4p_i}{2\pi^4}(2\pi)\delta(p_i^2 - m_i^2)(2\pi)^4\delta^4\Big(p_a + p_b - \sum_i p_i\Big)\Theta(E_i), \tag{2.61}$$

where p_a and p_b are the initial-state momenta [49].

The LO is only reliable for the shape of distributions due to large higher-order corrections. An accurate simulation often requires at least the NLO calculation. A cross section calculated at NLO depends on three parts, the LO or Born part, virtual corrections, and real emissions [36]. At NLO,

$$\begin{aligned}
\sigma_n^{(NLO)} &= \sum_{a,b}\int_0^1 dx_a dx_b f_{a/h_1}(x_a,\mu_F) f_{b/h_2}(x_b,\mu_F)\int d\hat{\sigma}^{NLO}_{ab\to n}(\mu_F,\mu_R) \\
&= \int d\Phi_{\mathcal{B}}\Big[\mathcal{B}_n(\Phi_{\mathcal{B}};\mu_F,\mu_R) + \mathcal{V}_n(\Phi_{\mathcal{B}};\mu_F,\mu_R)\Big] \\
&+ \int d\Phi_{\mathcal{R}}\mathcal{R}_n(\Phi_{\mathcal{R}};\mu_F,\mu_R)
\end{aligned} \tag{2.62}$$

where

$$\begin{aligned}
\mathcal{B}_n(\Phi_{\mathcal{B}};\mu_F,\mu_R) &= \bar{\sum_h}|\mathcal{M}_n^{(b)}(\Phi_{\mathcal{B}},h;\mu_F,\mu_R)|^2 \\
\mathcal{V}_n(\Phi_{\mathcal{B}};\mu_F,\mu_R) &= 2\bar{\sum_h}\mathfrak{Re}|\mathcal{M}_n^{(b)}(\Phi_{\mathcal{B}},h;\mu_F,\mu_R)\mathcal{M}_n^{\star(b+1)}(\Phi_{\mathcal{B}},h;\mu_F,\mu_R)| \\
\mathcal{R}_n(\Phi_{\mathcal{R}};\mu_F,\mu_R) &= 2\bar{\sum_h}|\mathcal{M}_{n+1}^{(b+1)}(\Phi_{\mathcal{R}},h;\mu_F,\mu_R)|^2
\end{aligned} \tag{2.63}$$

For phase space elements,

$$\begin{aligned}
d\Phi_{\mathcal{B}} &= dx_a dx_b f_{a/h_1}(x_a,\mu_F) f_{b/h_2}(x_b,\mu_F)\frac{1}{2\hat{s}_{ab}}d\Phi_n \\
d\Phi_{\mathcal{R}} &= dx_{a\prime} dx_{b\prime} f_{a\prime/h_1}(x_{a\prime},\mu_F) f_{b\prime/h_2}(x_{b\prime},\mu_F)\frac{1}{2\hat{s}_{a\prime b\prime}}d\Phi_n \\
d\Phi_n &= \prod_{i=1}^{n}\frac{d^4p_i}{2\pi^4}(2\pi)\delta(p_i^2-m_i^2)(2\pi)^4\delta^4\Big(p_a+p_b-\sum_i p_i\Big)\Theta(E_i)
\end{aligned} \tag{2.64}$$

To analyze the experimental data from the hadron collider, it would be beneficial to measure the distributions of final-state quarks and gluons. Unfortunately, due to the confinement of color charge, these particles are not the final-state particles of the reaction. Instead, the final-state particles are colorless. The jet provides a tool to study the footprint of the hadron collisions and should have the following event properties [50]:

- It is well-defined and can be easily measured from the hadronic final state.
- The order-by-order calculations in perturbation theory are easy to compute from the partonic final state.
- It is important to closely correlate the distributions of the final state quarks and gluons.

A precise algorithmic jet definition, or called jet algorithm will need to classify the jet final state of a collision and reconstruct its total momentum [49]. Many algorithms have been developed to satisfy the requirement of theoretical calculations and experiments. For a

thorough review of jet algorithms, see Ref. [36].

A jet observables in a given m-patron configuration and in all $m+1$-parton configurations should have the same value [34]. If the function F_J^m gives the value of a certain jet observable in terms of the momenta of the n final-state partons, then it should have

$$F_J^{m+1} \to F_J^m \tag{2.65}$$

The Born-level cross section $d\sigma^B$ can be written in terms of jet defining function $F_J^{(m)}$ as

$$d\sigma^B = d\Phi^{(m)} |\mathcal{M}_m|^2 F_J^{(m)} \tag{2.66}$$

where $d\Phi^{(m)}$ is the phase space of m-parton final state, and $\mathcal{M}_m$ is the matrix element. Then the real emission $d\sigma^R$ is

$$d\sigma^R = d\Phi^{(m+1)} |\mathcal{M}_{m+1}|^2 F_J^{(m+1)}. \tag{2.67}$$

2.3 The Dipole Subtraction Method

In the calculation of the NLO cross section, one obstacle is the occurrence of divergences. There are many ways to solve this problem. This section will introduce one widely used method in Monte Carlo event generator, which is called the Catani-Seymour subtraction method [34]. For a typical NLO jet cross section, one can write

$$\sigma = \sigma^{LO} + \sigma^{NLO}. \tag{2.68}$$

The LO cross section can be computed by integrating exclusive born level cross section $d\sigma^B$ over the phase space

$$\sigma^{LO} = \int_m d\sigma^B. \tag{2.69}$$

Then consider the exclusive cross section $d\sigma^R$ with $m+1$ partons in the final state. Adding the one-loop correction $d\sigma^V$ to the process with m partons in the final state, it can be written as

$$\sigma^{NLO} \equiv \int d\sigma^{NLO} = \int_{m+1} d\sigma^R + \int_m d\sigma^V \ . \tag{2.70}$$

In the above equation, phase space integral over $d\sigma^R$ and $d\sigma^V$ is individually divergent in four-dimensional space-time $d = 4$. When combined in Eq. 2.70, their sum becomes finite. To perform numerical integration of the phase space, it is necessary to regulate the divergences of $d\sigma^R$ and $d\sigma^V$ separately. By employing dimensional regularization, in which the integrations are carried out in $d = 4 - 2\epsilon$ dimensions, the divergences are replaced by double poles, $1/\epsilon^2$ (soft and collinear), as well as single poles, $1/\epsilon$ (soft, collinear, or ultraviolet). Ultraviolet divergences in $d\sigma^V$ can be absorbed into coupling constants through the renormalization procedure. The general idea of the subtraction method is to use the identity

$$d\sigma^{NLO} = \left[d\sigma^R - d\sigma^A\right] + d\sigma^A + d\sigma^V \ \ , \tag{2.71}$$

where $d\sigma^A$ is a proper approximation of $d\sigma^R$ which must have the same pointwise singular behavior in d dimensions as $d\sigma^R$. $d\sigma^A$ is a local counterterm for $d\sigma^R$. Now introducing the phase space integration,

$$\sigma^{NLO} = \int_{m+1} \left[d\sigma^R - d\sigma^A\right] + \int_{m+1} d\sigma^A + \int_m d\sigma^V, \tag{2.72}$$

where the first term on the right side of Eq. 2.72 can be integrated numerically in the limit $\epsilon \to 0$.

Now, all singularities converge to the last two terms on the right-hand side of Eq. 2.72. One can compute the integration of $d\sigma^A$ over the one-parton subspace analytically and combine those singularities with those in $d\sigma^V$, and then the divergences

will be canceled. The final structure of the calculation is as follows:

$$\sigma^{NLO} = \int_{m+1} \left[d\sigma^R - d\sigma^A \right] + \int_m \left[d\sigma^V + \int_1 d\sigma^A \right]. \tag{2.73}$$

The symbolic factorization formulae of the Catani-Seymour method for the arbitrary process is

$$d\sigma^A = \sum_{\text{dipoles}} d\sigma^B \otimes dV_{\text{dipole}}, \tag{2.74}$$

where $d\sigma^B$ denotes an appropriate color and spin projection of the born-level exclusive cross section. The symbol $\otimes$ denotes properly defined phase space convolutions and sums over color and spin indices. The dipole factors dV_{dipole} are independent of the process and should match the singular behavior of $d\sigma^R$. As the $m+1$ parton state in $d\sigma^R$ approaches the soft and/or collinear region, the dipole factor in $d\sigma^A$ approaches the same region with an equivalent probability to that of $d\sigma^R$. Then one can map the $m+1$ parton phase space to an m parton phase space times a single-parton phase space. Thus,

$$\int_{m+1} d\sigma^A = \sum_{\text{dipoles}} \int_m d\sigma^B \otimes \int_1 dV_{\text{dipole}} = \int_m \left[d\sigma^B \otimes \mathbf{I} \right] \tag{2.75}$$

where the universal factor $\mathbf{I}$ is defined as

$$\mathbf{I} = \sum_{\text{dipoles}} \int_1 dV_{\text{dipole}}. \tag{2.76}$$

The dipole factor $\mathbf{I}$ contains the $1/\epsilon$ and $1/\epsilon^2$ poles with equal value and opposite signs as in the $d\sigma^V$. After canceling all divergences, one can take the limit $\epsilon \to 0$ and perform the integration analytically in four space-time dimensions. Here are the two contributions, $\sigma^{NLO\,\{m+1\}}$ and $\sigma^{NLO\,\{m\}}$ are separately finite and integrable. The final structure is as

follows,

$$\begin{aligned}\sigma^{NLO} &= \sigma^{NLO\,\{m+1\}} + \sigma^{NLO\,\{m\}} \\ &= \int_{m+1} \left[\left(d\sigma^R \right)_{\epsilon=0} - \left(\sum_{\text{dipoles}} d\sigma^B \otimes \, dV_{\text{dipole}} \right)_{\epsilon=0} \right] + \int_m \left[d\sigma^V + d\sigma^B \otimes \boldsymbol{I} \right]_{\epsilon=0} \quad .\end{aligned} \tag{2.77}$$

The Catani-Seymour method provides the general formalism to calculate the NLO QCD corrections. The Higgs boson production via VBF is calculated in Ref. [51]. The NLO QCD corrections to Higgs boson production in association with three jets via vector boson fusion were calculated and implemented in `VBFNLO` in Ref. [22].

CHAPTER 3
MATCHING AND MERGING

In this Chapter, based on Ref. [35], we perform our first investigation into the NLO predictions for electroweak Higgs production that has been merged with a dipole shower using the full set of tree-level and one-loop matrix elements available via the `HJets` matrix element library. The Ref. [35] was published in: Chen, Tinghua, Terrance M. Figy, and Simon Plätzer. "NLO multijet merging for Higgs production beyond the VBF approximation." The European Physical Journal C 82, no. 8 (2022): 704. All equations and figures are taken from Ref. [35].

3.1 The Matching in Herwig 7

Matching parton showers to next-to-leading order QCD has become the de-facto standard for reliable simulations at hadron colliders. The term "matching" refers to a methodology that subtracts the expansion of the parton shower to $\mathcal{O}(\alpha_s)$ from the fixed-order NLO calculation, thereby ensuring that the resulting distribution after showering accurately represents NLO effects to $\mathcal{O}(\alpha_s)$. Regarding scale setting within the matching algorithms applied in Herwig 7, a comprehensive discussion can be found in the Ref. [52] with various options, all of which are applicable to the Herwig 7 parton showers as documented in Ref. [30, 53, 54]. In the current investigation, we have adopted the default setting known as the "resummation profile." This particular choice features a narrowly smeared step function towards the hard scale, ensuring that it does not introduce spuriously small variations.

The Herwig 7 framework offers a comprehensive platform for interfacing external matrix element providers, such as `HJets` [55–58] and `VBFNLO` 3, with the `Matchbox` module [30]. The `Matchbox` module enables the assembly of fully differential next-to-leading order (NLO) cross sections from these external matrix elements. Through the `Matchbox` module Herwig 7 is able to match NLO matrix elements to both the angular ordered [54] and dipole showers [30, 53] using either a subtractive

(MC@NLO-type [59]) matching algorithm or a multiplicative (Powheg-type [60]) matching algorithm. In this chapter, our primary focus lies on the dipole shower matched via the subtractive matching paradigm. This choice is motivated by the objective of employing merging algorithms of different jet multiplicities, which, inside of Herwig 7 are currently only available with the dipole shower algorithm. A detailed discussion on differences between shower algorithms and matching schemes has extensively been discussed in [61] in the context of Higgs production via VBF.

3.2 The Unitary Merging Algorithm

As opposed to matching, merging algorithms do facilitate the combination of several jet multiplicities with the parton shower. At leading order, stability with respect to the resolution which separates hard jet production from parton shower radiation is achieved by carefully crafting this resolution to be compatible with the shower phase space and order. No spurious logarithms of the merging scale are then expected to arise since the shower is considered to be a good approximation to tree-level real emission matrix elements in the transition region. This is not true anymore at NLO, and a new paradigm of merging needs to be employed which is correcting for the lack of perturbative information contained in the parton shower. These unitarized merging algorithms preserve certain features of inclusive cross sections [62–64], and thus generate approximate NNLO contributions which are required for a stable merging. The full implementation of the unitary merging algorithm used by Herwig 7 was described in Ref. [65], and does not enforce the reproduction of inclusive cross sections exactly, but only subtracts contributions which are classified as logarithmically enhanced if they are accessible by a possible parton shower history. The process is otherwise considered to contribute a new, hard jet configuration from which the parton shower is evolving in a vetoed manner such as not to double count contributions both in real emission as well as virtual and unresolved corrections. At the same time, this approach allows the merging algorithm to deal with processes that involve jets already at the level of the hard process. In our studies, the merging scale ρ_s is smeared according to

Eq. (40), $\rho_s = \rho_C \cdot (1 + (2 \cdot r - 1) \cdot \delta)$ of Ref. [65] . The central merging scale is set as $\rho_C = 25$ GeV with $\delta = 0.1$ for results investigating the impact of varying the factorization and renormalization scales. We use the CMW scheme [65, 66] for the merged simulations with the modified strong coupling set to $\alpha'_S(q) = \alpha_S(k_g(q))$ where $k_g = \exp(-K_g/b_0)$, $K_g = C_A\left(\frac{67}{18} - \frac{1}{6}\pi^2\right) - \frac{5}{9}N_F$, and $b_0 = 11 - 2/3N_F$.

3.3 Simulation Results

In this section, I will present the matching and merging simulation results by using Herwig 7. The matrix elements used in this study were provided via the external matrix element providers: `HJets 1.2` for full calculation and `VBFNLO 3` for VBF approximation. The `HJets 1.2` module [55–58] provides tree-level matrix elements for $2 \to h + 2, 3, 4$ partons and one-loop matrix elements for $2 \to h + 2, 3$ partons for electroweak Higgs boson production in association with jets. The color algebra is computed by the library `ColorFull` [67] and the one-loop integrals are performed based on the tensor loop integral reduction methods described in Ref. [68]. The matrix elements programmed in `VBFNLO 3.0.0` beta 5 [19–22] were used to compute tree-level and one-loop matrix elements in the VBF approximation via the Binoth one-loop accord [32, 33].

The merging calculation performed in this section includes: $h(2^\star, 3^\star, 4)$, $h(2^\star, 3)$, $h(2, 3)$, $h(2^\star, 3, 4)$, and $h(2, 3, 4)$. The matching process includes $h(3^\star) \bigoplus \text{PS}$ and $h(2^\star) \bigoplus \text{PS}$. The input parameters for the Monte Carlo event generator are described in Ref. [35], and in Chapter 6.

In the context of electroweak Higgs boson production, the fundamental process at the Born level is described by $pp \to hjj$, where the tree-level $2 \to h + 2$ partonic matrix elements (MEs) are denoted as $h(2)$. To account for additional partonic multiplicities in a leading-order merged setup, we incorporate tree-level MEs accordingly. Specifically, we represent the merging of MEs involving n partons as $h(2, 3, 4, \ldots, n)$ with $n \geq 2$. This notation represents the inclusion of tree-level MEs for partonic processes with $h + 2$, $h + 3$, $h + 4$, and up to $h + n$ partons.

In simulations involving the merging of higher-order matrix elements, we introduce an additional $\star$ symbol to indicate each multiplicity n as $n^\star$. This notation signifies that, in addition to the tree-level MEs, the one-loop correction is included. For instance, the notation $h(2^\star, 3, 4)$ represents the production of a Higgs boson with up to 2 additional partonic emissions, where one-loop MEs are applied for the $h + 2$ parton processes. The special case of $h(2^\star, 3)$ corresponds to the "matching through merging" limit within the merging approach implemented in HERWIG 7, which achieves the same level of accuracy as NLO matching. A detailed discussion on merging can be found in the previous section for more details. In scenarios where applying subtractive matching to connect an NLO calculation with a dipole parton shower, the NLO matched setup is denoted for $pp \to hjj$ as $h(2^\star) \bigoplus \text{PS}$ and $pp \to hjjj$ as $h(3^\star) \bigoplus \text{PS}$.

Fig. 3.1 and Fig. 3.2 show results for the splitting scales $\sqrt{d_2}$ and $\sqrt{d_3}$ of the k_T jet algorithm [69, 70]. The splitting scales are resolution scales $\sqrt{d_k}$ of the k_T jet algorithm at which the event switches from k jet event to a $k + 1$ jet event. The Fig. 3.1 presents results for the merged setup $h(2^\star, 3^\star, 4)$ with the central merging scale ρ_C set to the following values: $15, 25, 35$ GeV. In the transition region between the $h + n$ parton MEs and the $h + (n + 1)$ parton MEs near $\sqrt{d_n} \approx 25$ GeV, there is 10% variation for $n = 2, 3$. Fig. 3.2 shows results comparing the merged setups and matched setups against the merged setup $h(2^\star, 3^\star, 4)$. The matched results $h(2^\star) \bigoplus \text{PS}$ and matching by merging setup $h(2^\star, 3)$ have a similar pattern after $\sqrt{d_2} \approx 125$ GeV and $\sqrt{d_3} \approx 125$ GeV. The matched results $h(2^\star) \bigoplus \text{PS}$ and $h(3^\star) \bigoplus \text{PS}$ complement each other to some extent. The generation cut of 10 GeV on transverse momentum for the $h(3^\star) \bigoplus \text{PS}$ leads to a suppression around $\sqrt{d_2} \approx 10$ GeV and $\sqrt{d_3} \approx 10$ GeV. Furthermore, the matched $h(3^\star) \bigoplus \text{PS}$ result is missing the $h + 2$ jet events. The merged calculation is clearly reproduced by the matched ones in the regions where the respective jet multiplicity is resolved and the fixed order, hard jet multiplicity, provides a reliable prediction. However, the merged description is able to interpolate in between the different multiplicities.

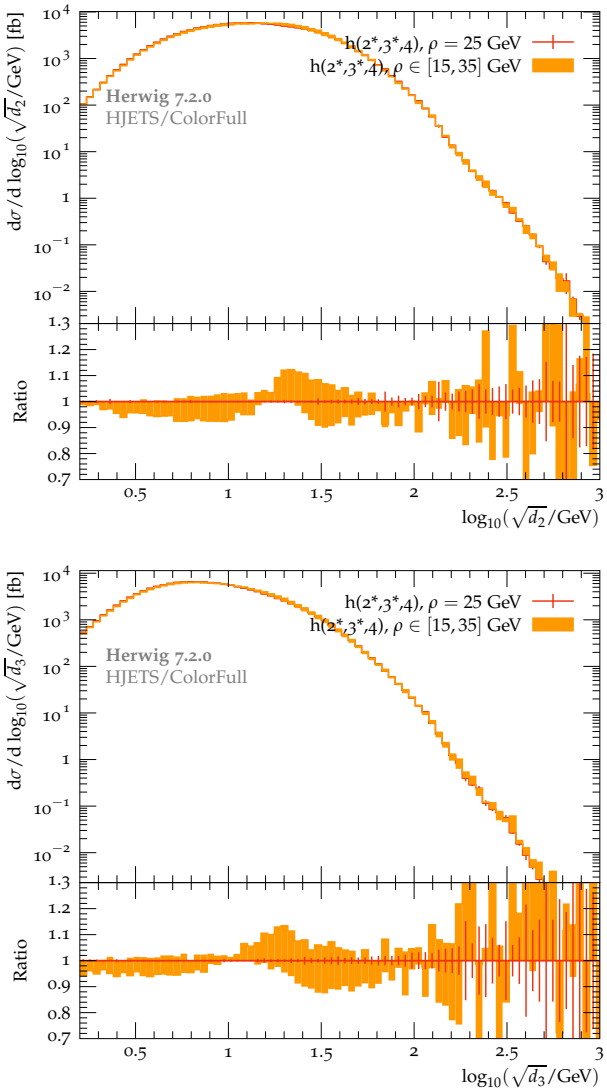

Figure 3.1: Comparison plots for $\sqrt{d_2}$ (top) and $\sqrt{d_3}$ (bottom). The theory band in orange results from varying the merging scale for the prediction of $h(2^\star, 3^\star, 4)$.

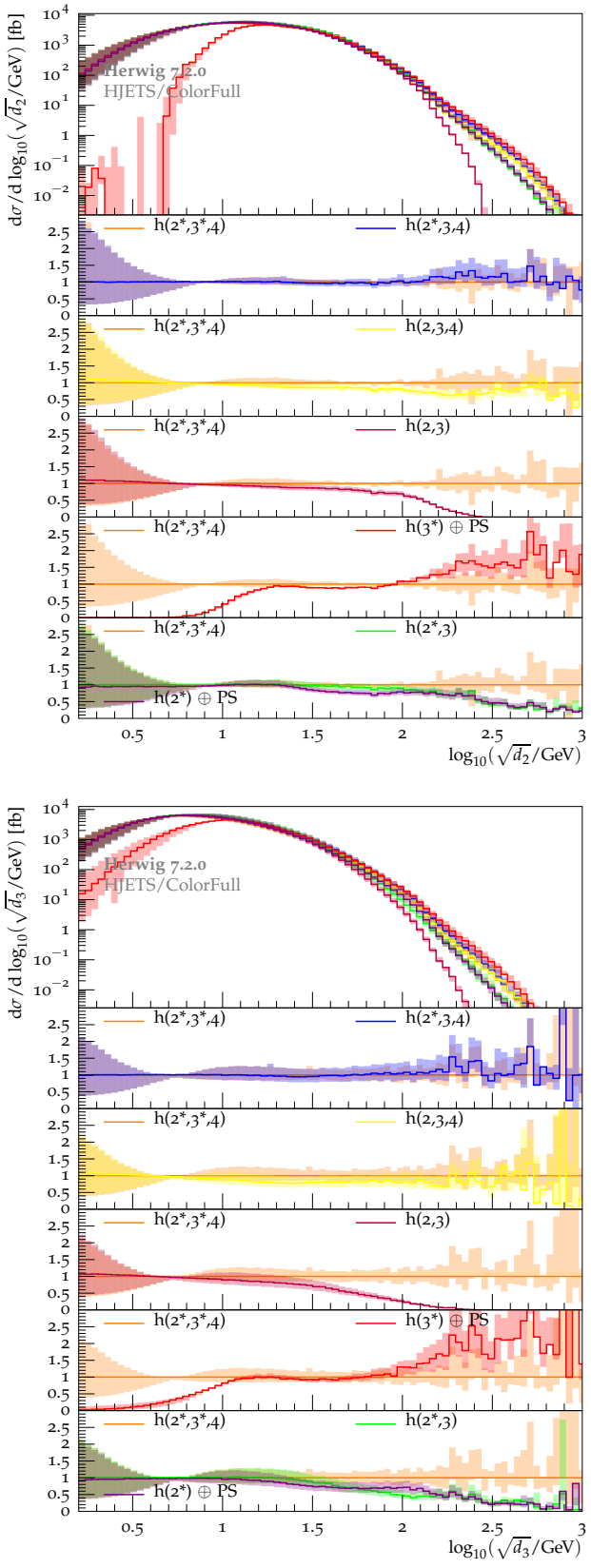

Figure 3.2: Comparison plots for $\sqrt{d_2}$ (top) and $\sqrt{d_3}$ (bottom) for predictions of $h(2^\star, 3^\star, 4)$, $h(2^\star, 3, 4)$, $h(2, 3, 4)$, $h(2^\star, 3)$, $h(2, 3)$, $h(3^\star) \bigoplus \text{PS}$, and $h(2^\star) \bigoplus \text{PS}$ with $h(2^\star, 3^\star, 4)$ being the reference in the ratio plots.

Here the renormalization scale to be $\mu_R = \xi_R \mu_0$ and the factorization scale to be $\mu_F = \xi_F \mu_0$ with ξ_F and ξ_R denoting the scale factors. The error bands shown in the figures are due to the variation of the renormalization and factorization scale factors ξ_F and ξ_R with $\xi_F = \xi_R = 1/2, 1$ and 2.

Fig. 3.3 and Fig. 3.4 show cross sections binned according to the exclusive number of identified jets N_{jets} and the exclusive number of identified gap jets $N_{\text{jets}}^{\text{gap}}$ for INCL selection cuts and TIGHT selection cuts. In the ratio plots, all results are divided by the result of the merged setup $h(2^\star, 3^\star, 4)$. The matched setup $h(2^\star) \bigoplus \text{PS}$ when compared to the $h(2^\star, 3^\star, 4)$ agrees up until two identified jets and 0 identified gap jets. Further the $h(2^\star) \bigoplus \text{PS}$ result appears to underestimate the theoretical errors. As shown in the bottom plot of Fig. 3.3 and Fig. 3.4, the merged setups using the `HJets` MEs are compared against `VBFNLO` MEs using TIGHT selection cuts. The reference in ratio plots is the prediction using the `HJets` MEs. There is a good agreement for the binned cross section in the exclusive number of jets up to 4 jets and for the binned cross section in the number of exclusive gap jets up to 2 gap jets. The hard sub-processes using `VBFNLO` and `HJets` MEs are assigned different colour flows in the large-N_c limit, since the full calculation takes into account all contributing topologies. Since the dipole shower evolution is intimately connected to the hard sub-process colour flow, different hard sub-process colour flows result in different shower histories. The TIGHT selection cuts essentially allow extra jets in the gap between the leading two jets. Both $h + 3$ and $h + 4$ parton events allow for extra jets in the gap between the jets even after the strict TIGHT selection cuts. One should note that the rate is quite small in these higher multiplicity bins.

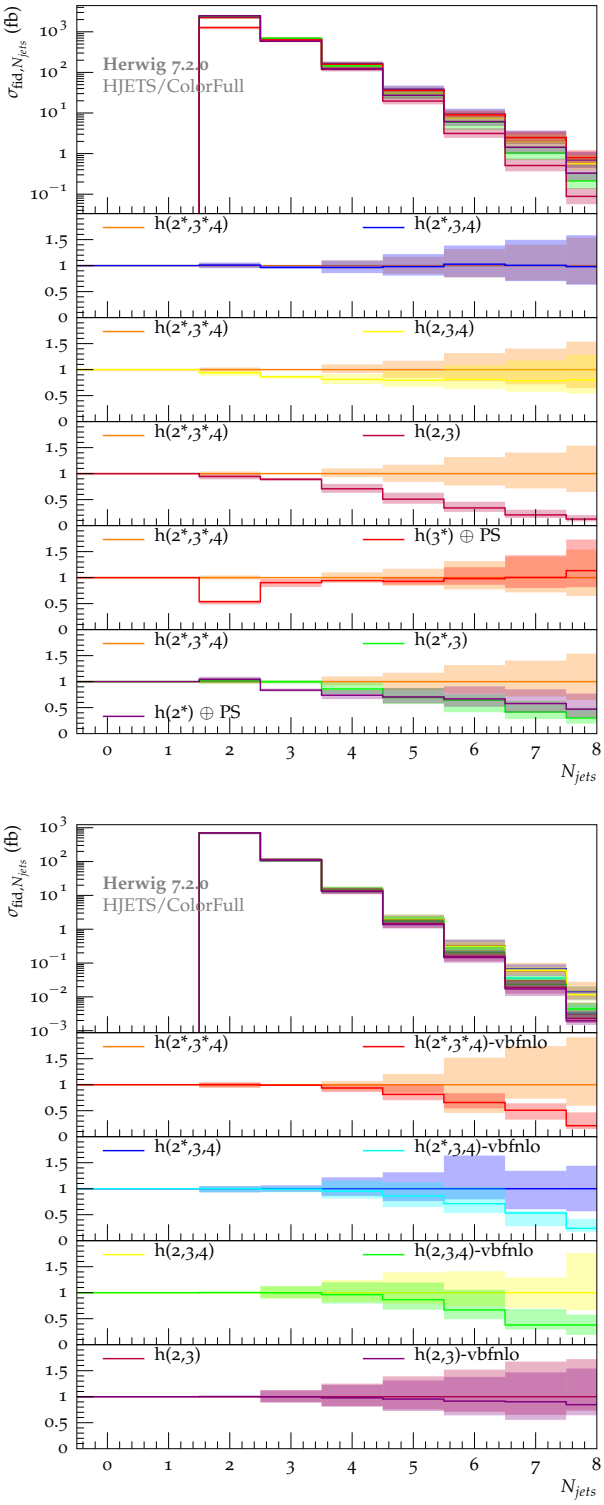

Figure 3.3: Exclusive number of jets with INCL (top) and TIGHT (bottom) selection cuts for the predictions of $h(2^\star, 3^\star, 4)$, $h(2^\star, 3, 4)$, $h(2, 3, 4)$, $h(2^\star, 3)$, $h(2, 3)$, $h(3^\star) \bigoplus \mathrm{PS}$, and $h(2^\star) \bigoplus \mathrm{PS}$. $h(2^\star, 3^\star, 4)$ is the reference in the ratio plots for the top plot. In the bottom plot, setups using `VBFNLO` MEs are compared against setups using `HJets` MEs. Shown in the figures are theory error bands due to the variation of the factorization and renormalization scales.

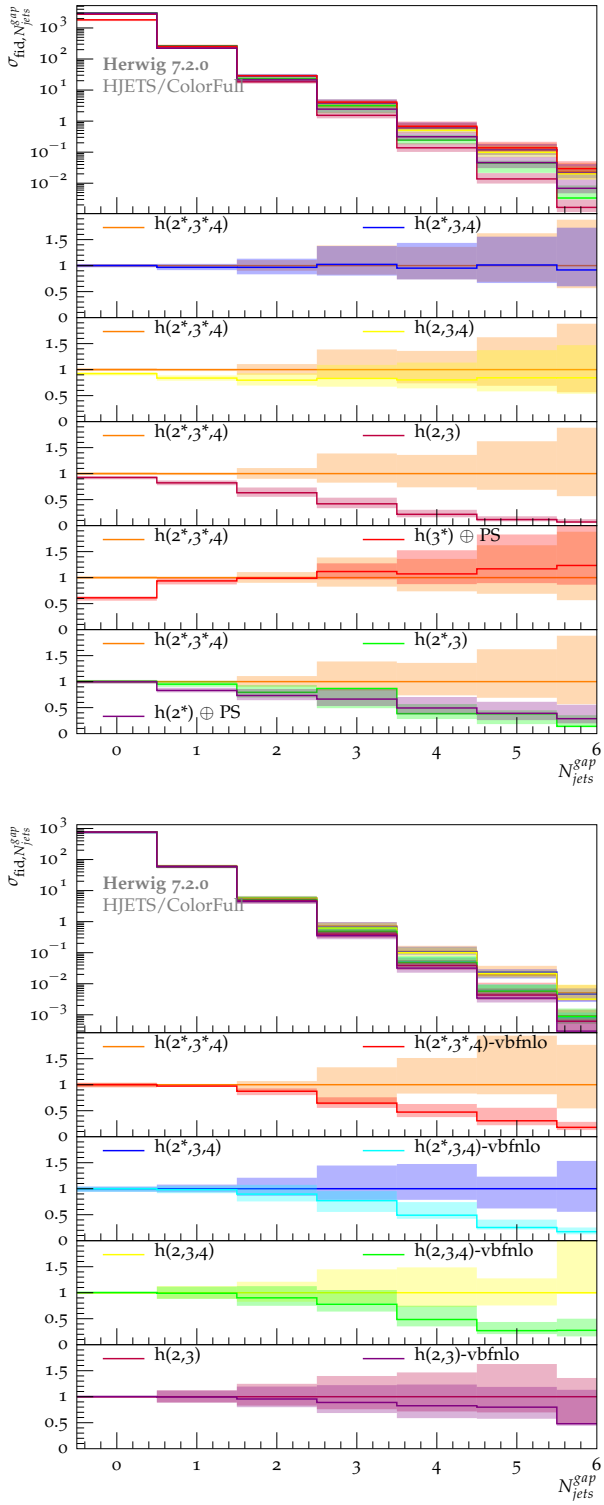

Figure 3.4: Exclusive number of gap jets with INCL (top) and TIGHT (bottom) selection cuts for the predictions of $h(2^\star, 3^\star, 4)$, $h(2^\star, 3, 4)$, $h(2, 3, 4)$, $h(2^\star, 3)$, $h(2, 3)$, $h(3^\star) \bigoplus \mathrm{PS}$, and $h(2^\star) \bigoplus \mathrm{PS}$. $h(2^\star, 3^\star, 4)$ is the reference in the ratio plots for the top plot. In the bottom plot, setups using `VBFNLO` MEs are compared against setups using `HJets` MEs. Shown in the figures are theory error bands due to the variation of the factorization and renormalization scales.

Define the quantity named rapidity, which is denoted with y,

$$y = \frac{1}{2}\ln\left(\frac{E + p_z}{E - p_z}\right), \tag{3.1}$$

where E is the energy of particles, and p_z is the momentum of particles in the z-axis. The transverse momentum, p_T is defined by

$$p_T = \sqrt{p_x^2 + p_y^2}, \tag{3.2}$$

where p_x and p_y are the momentum component for x-axis and y-axis. Another useful quantity is the invariant mass for two jets, defined as

$$m_{j_1 j_2} = \sqrt{(p_{j_1} + p_{j_2})^2}, \tag{3.3}$$

where p_{j_1} and p_{j_2} are the four-momentum of the first leading jet and the second leading jet. In Fig. 3.5, the distributions in the rapidity difference of the leading two jets $\Delta y_{j_1 j_2}$ and the invariant mass of the leading two jets $m_{j_1 j_2}$ are shown. There is good agreement between the matched setup $h(2^\star) \bigoplus \mathrm{PS}$ and merged setups $h(2^\star, 3^\star, 4)$, $h(2^\star, 3, 4)$ and $h(2^\star, 3)$ with the exception of a region between 100 GeV and 150 GeV in the invariant mass of leading two jets which is no more that 10%. The leading order merged setups $h(2, 3, 4)$ and $h(2, 3)$ deviate as expected.

Shown in the top row of Fig. 3.6 using INCL selection cuts are the kinematic distributions in the transverse momentum of third leading jet p_{T,j_3} and the centrality of the third jet $z^*_{j_3}$ defined as

$$z^*_{j_3} = \frac{y_{j_3} - \frac{y_{j_1} + y_{j_2}}{2}}{|\Delta y_{j_1 j_2}|}. \tag{3.4}$$

For the transverse momentum and the centrality of the third jet, the matched setup $h(2^\star) \bigoplus \mathrm{PS}$ when compared to $h(2^\star, 3^\star, 4)$ deviate by up to 20%. This feature is shared by the matching by merging setups $h(2^\star, 3)$. It is quite obvious that relying on the parton

shower alone without including the $h + 4$ parton hard scattering matrix elements fails to describe the higher jet multiplicities beyond 2. In the bottom plot of Fig. 3.6 using LOOSE selection cuts there are deviations between predictions based on `VBFNLO` MEs and the `HJets` MEs the largest deviations when using NLO MEs. All predictions deviate at the level 40% around $z_{j_3} = 0$. This is the result of the missing s-channel contributions in the `VBFNLO` predictions.

The kinematic distributions for transverse momentum of the Higgs boson plus two leading jets p_{T,hj_1j_2} from matched and merged setups are presented in Fig. 3.7. The p_{T,hj_1j_2} is defined by

$$p_{T,hj_1j_2} = \Big(p_h + p_{j_1} + p_{j_2}\Big)_T, \tag{3.5}$$

where p_h, p_{j_1}, p_{j_2} label the momentum of the Higgs boson, the momentum of the first leading jet and the momentum of the second leading jet. The subscript T represents the transverse component of the momentum sum. The distributions in p_{T,hj_1j_2} shows an enhancement when comparing NLO matched result $h(2^\star) \bigoplus \mathrm{PS}$ to the NLO merged $h(2^\star, 3^\star, 4)$ result. The theory error is underestimated by the NLO matched $h(2^\star) \bigoplus \mathrm{PS}$ predictions. The matching by merging setups $h(2, 3)$ and $h(2^\star, 3)$ follow a similar pattern to the $h(2^\star) \bigoplus \mathrm{PS}$ setup. When comparing merged setups using the `HJets` MEs against the `VBFNLO` MEs for the LOOSE selection cuts, the deviations show in the tail of the p_{T,hj_1j_2} distribution. This suggests that applying an overall K factor to predictions using LO merged setup may not describe the physics very well.

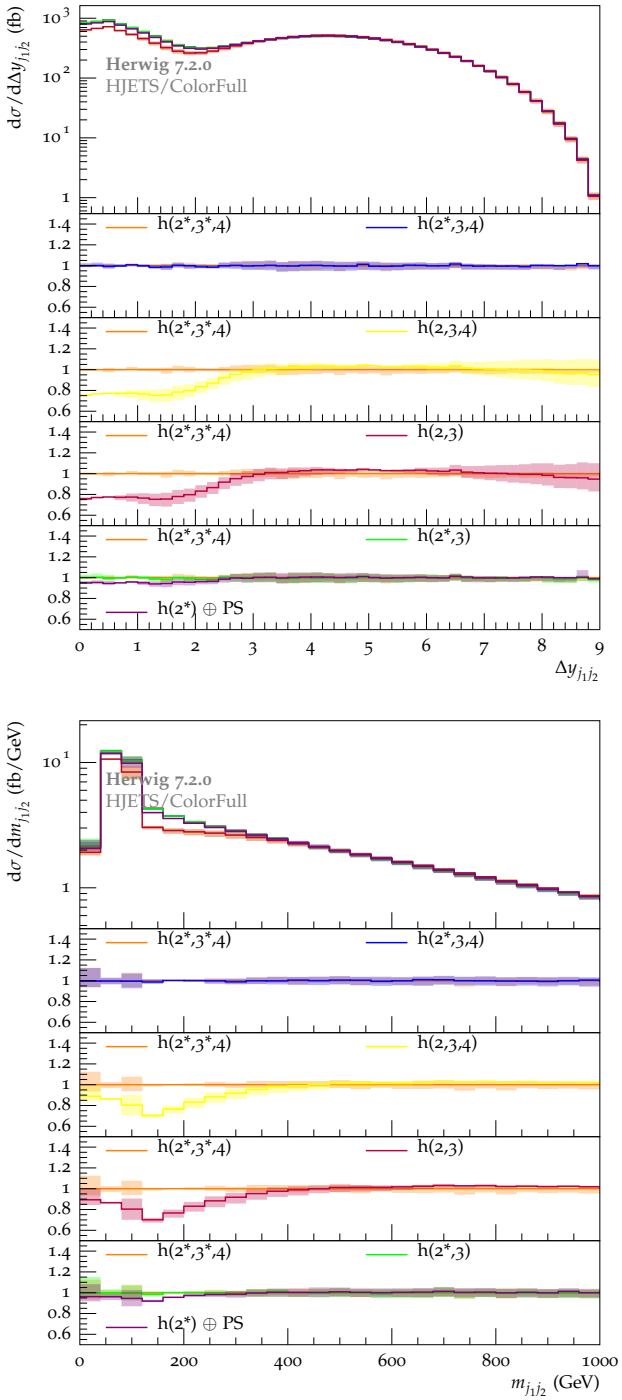

Figure 3.5: Shown is the distribution of 2 jets observables with INCL selection cuts: rapidity gap $\Delta y_{j_1 j_2}$ (top) and invariant mass $m_{j_1 j_2}$ (bottom) of the two tagging jets. The prediction is $h(2^\star, 3^\star, 4)$, $h(2^\star, 3, 4)$, $h(2, 3, 4)$, $h(2^\star, 3)$, $h(2, 3)$, $h(3^\star) \bigoplus \mathrm{PS}$, and $h(2^\star) \bigoplus \mathrm{PS}$ with $h(2^\star, 3^\star, 4)$ being the reference in the ratio plots. Shown in the figures are theory error bands due to the variation of the factorization and renormalization scales.

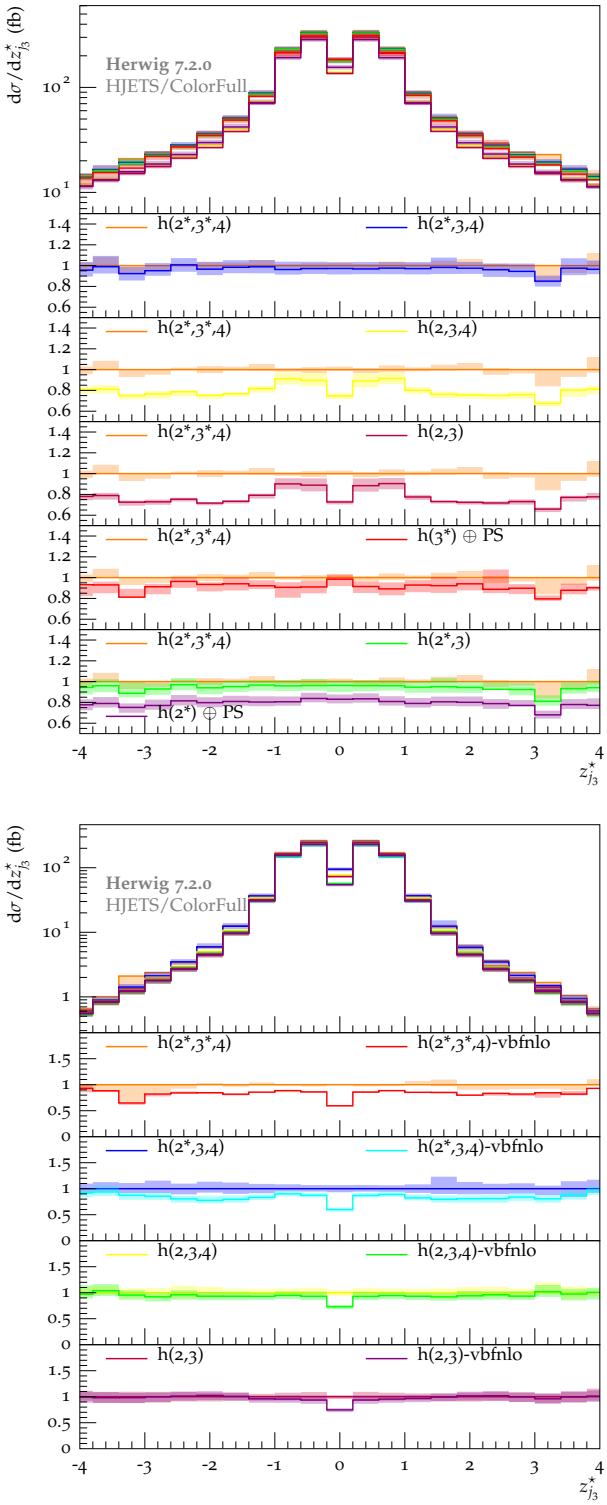

Figure 3.6: Shown are kinematic distributions for the Zeppenfeld variable $z^{\star}_{j_3}$. The top plot shows predictions $h(2^{\star},3^{\star},4)$, $h(2^{\star},3,4)$, $h(2,3,4)$, $h(2^{\star},3)$, $h(2,3)$, $h(3^{\star})\bigoplus\mathrm{PS}$, and $h(2^{\star})\bigoplus\mathrm{PS}$ are compared to the $h(2^{\star},3^{\star},4)$ prediction (INCL selection cuts). The bottom plot compares the merged setups using `VBFNLO` MEs against the setups using `HJets` MEs using LOOSE selection cuts. Shown in the figures are theory error bands due to the variation of the factorization and renormalization scales.

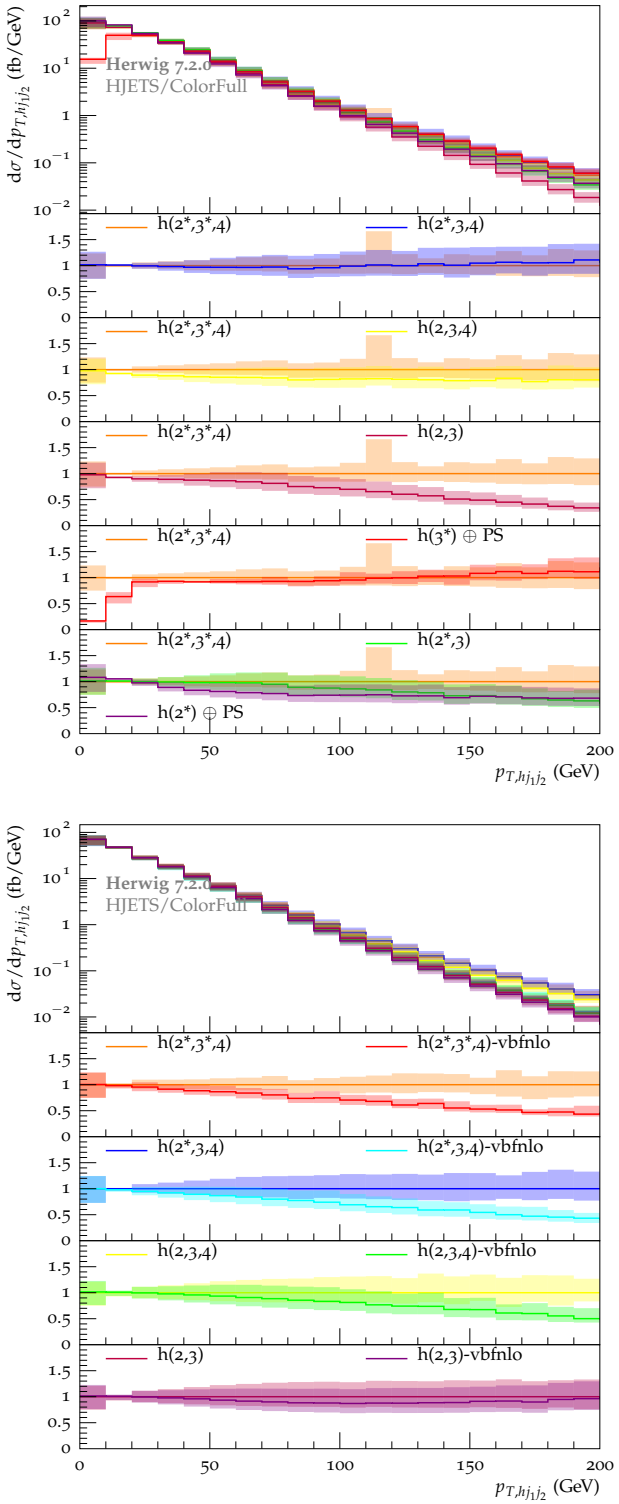

Figure 3.7: Shown are distributions for the transverse momentum of the Higgs boson plus two leading jets system p_{T,hj_1j_2}. The top plot show predictions $h(2^\star, 3^\star, 4)$, $h(2^\star, 3, 4)$, $h(2, 3, 4)$, $h(2^\star, 3)$, $h(2, 3)$, $h(3^\star) \bigoplus \text{PS}$, and $h(2^\star) \bigoplus \text{PS}$ are compared to the $h(2^\star, 3^\star, 4)$ prediction (INCL selection cuts). The bottom plot compares the merged setups using `VBFNLO` MEs against the setups using `HJets` MEs for LOOSE selection cuts. Shown in the figures are theory error bands due to the variation of the factorization and renormalization scales.

CHAPTER 4
ELEMENTS OF CALCULATIONS

In this chapter, first, I will introduce the generalized tensor structure of the HVV vertex and then follow with the introduction of the parameterization that `VBFNLO` supported. The helicity amplitude formalism will be introduced and the leading order calculation will be shown as an example. I will present the code structure of `VBFNLO` and the subroutines I developed for Higgs boson anomalous coupling associated with three jets at NLO in order to perform the anomalous coupling effect for Higgs boson production via VBF using the merging and matching framework in Herwig 7.

4.1 Anomalous Couplings

Vector boson fusion at the LHC can provide key information on the strength and structure of the Higgs couplings to the vector bosons. In `VBFNLO`, the general tensor structure of the HVV vertex can be written as the following equation in the massless quark limit [23, 71]

$$T^{\mu\nu}(q_1,q_2) = a_1(q_1,q_2)\; g^{\mu\nu} + a_2(q_1,q_2)\; [q_1\cdot q_2 g^{\mu\nu} - q_2^{\mu} q_1^{\nu}] + a_3(q_1,q_2)\; \varepsilon^{\mu\nu\rho\sigma} q_{1\rho} q_{2\sigma}\;, \qquad (4.1)$$

where $\varepsilon^{\mu\nu\rho\sigma}$ is the totally antisymmetric Levi-Civita tensor with convention $\varepsilon_{0123} = 1$. In the above equation, the constant a_1 represents the SM HVV couplings with $a_2 = a_3 = 0$, while the constant a_2 and a_3 could represent the new physics. q_1 and q_2 are the four momenta of the intermediate weak bosons (W, Z).

The anomalous coupling terms a_2 and a_3 can be derived from the effective Lagrangian and can be written as the following equation:

$$\begin{aligned}\mathcal{L}_{eff} \;=\; & \frac{g_{5e}^{HWW}}{\Lambda_{5e}} H W^{+}_{\mu\nu} W^{-\mu\nu} + \frac{g_{5o}^{HWW}}{\Lambda_{5o}} H \tilde{W}^{+}_{\mu\nu} W^{-\mu\nu} + \\ & \frac{g_{5e}^{HZZ}}{2\Lambda_{5e}} H Z_{\mu\nu} Z^{\mu\nu} + \frac{g_{5o}^{HZZ}}{2\Lambda_{5o}} H \tilde{Z}_{\mu\nu} Z^{\mu\nu}\;. \end{aligned} \qquad (4.2)$$

Here the subscript e or o represents the CP-even or CP-odd nature of the individual operators. In this dissertation, I will neglect possible contributions from $H\gamma\gamma$ and $H\gamma Z$ couplings which can appear in $SU(2) \times U(1)$ invariant formulations [72, 73] and have only focused on the HZZ and HWW contributions.

In general, a_i from Eq. 4.1 are also called the form factors. It can be derived from the effective Lagrangian of Eq. 4.2,

$$a_2(q_1, q_2) = -\frac{2}{\Lambda_{5e}} g_{5e}^{HWW} \ , \qquad a_3(q_1, q_2) = \frac{2}{\Lambda_{5o}} g_{5o}^{HWW} \tag{4.3}$$

for the HWW vertex, and

$$a_2(q_1, q_2) = -\frac{2}{\Lambda_{5e}} g_{5e}^{HZZ} \ , \qquad a_3(q_1, q_2) = \frac{2}{\Lambda_{5o}} g_{5o}^{HZZ} \tag{4.4}$$

for the HZZ vertex. The `VBFNLO` code supports form factors in general form:

$$a_i(q_1, q_2) = a_i(0, 0) \ \frac{M^2}{q_1^2 - M^2} \ \frac{M^2}{q_2^2 - M^2}. \tag{4.5}$$

When the transferred momentum $\sqrt{-q_i^2}$ is smaller than mass scale M, the anomalous coupling effects could probe for NP. On the other hand, when the momentum carried by the virtual gauge boson reaches the mass scale, the anomalous couplings are suppressed.

For the anomalous couplings, `VBFNLO` also supports the parameterization used by L3 collaboration [74], which the Lagrangian [23, 75] is

$$\begin{aligned}
\mathcal{L}_{eff} = & \ g_{H\gamma\gamma} H A_{\mu\nu} A^{\mu\nu} + g_{HZ\gamma}^{(1)} A_{\mu\nu} Z^{\mu} \partial^{\nu} H + g_{HZ\gamma}^{(2)} H A_{\mu\nu} Z^{\mu\nu} \\
& + g_{HZZ}^{(1)} Z_{\mu\nu} Z^{\mu} \partial^{\nu} H + g_{HZZ}^{(2)} H Z_{\mu\nu} Z^{\mu\nu} + g_{HWW}^{(2)} H W_{\mu\nu}^{+} W_{-}^{\mu\nu}, && (4.6) \\
& + g_{HWW}^{(1)} (W_{\mu\nu}^{+} W_{-}^{\mu} \partial^{\nu} H + W_{\mu\nu}^{-} W_{+}^{\mu} \partial^{\nu} H) + \tilde{g}_{H\gamma\gamma} \ H \tilde{A}_{\mu\nu} A^{\mu\nu} && (4.7) \\
& + \tilde{g}_{HZ\gamma} \ H \tilde{A}_{\mu\nu} Z^{\mu\nu} + \tilde{g}_{HZZ} \ H \tilde{Z}_{\mu\nu} Z^{\mu\nu} + \tilde{g}_{HWW}^{(2)} \ H \tilde{W}_{\mu\nu}^{+} W_{-}^{\mu\nu}. && (4.8)
\end{aligned}$$

where $X_{\mu\nu} = \partial_\mu X_\nu - \partial_\nu X_\mu$, and the corresponding fields for photon, Z, W and Higgs boson denoted as A_μ, Z_μ, W_μ and H. Since I have focused on the HWW and HZZ vertex in this study, I will exclusively present the anomalous couplings related to the HWW and HZZ vertex below. The CP-even couplings [20, 76–78] are

$$g^{(1)}_{HZZ} = \frac{e}{m_W \sin\theta_W}(\Delta g_1^Z \cos 2\theta_W + \Delta\kappa_\gamma \tan^2\theta_W), \tag{4.9}$$

$$g^{(2)}_{HZZ} = \frac{e}{2m_W \sin\theta_W}(d\cos^2\theta_W + d_B \sin^2\theta_W), \tag{4.10}$$

$$g^{(1)}_{HWW} = \frac{em_W}{\sin\theta_W m_Z^2}\Delta g_1^Z, \tag{4.11}$$

$$g^{(2)}_{HWW} = \frac{e}{\sin\theta_W m_W} d. \tag{4.12}$$

The parameters d, d_B, Δg_1^Z and $\Delta\kappa_\gamma$ can be set as input in `anom_HVV.dat`. The CP-odd couplings [20] are

$$\tilde{g}^{(1)}_{HZZ} = \frac{e}{m_W \sin\theta_W}(\tilde{\kappa}_\gamma \tan^2\theta_W), \tag{4.13}$$

$$\tilde{g}^{(2)}_{HZZ} = \frac{e}{2m_W \sin\theta_W}(\tilde{d}\cos^2\theta_W + \tilde{d}_B \sin^2\theta_W), \tag{4.14}$$

$$\tilde{g}^{(1)}_{HWW} = 0, \tag{4.15}$$

$$\tilde{g}^{(2)}_{HWW} = \frac{e}{\sin\theta_W m_W}\tilde{d}. \tag{4.16}$$

The CP-odd part has a similar form as the CP-even part. All the parameters $\tilde{d}$, $\tilde{d}_B$, and $\tilde{\kappa}_\gamma$ are the input values in `anom_HVV.dat` but there is no $\tilde{g}_1^Z$. These can be related to the form

factors in Eq. 4.1 as follows:

$$
\begin{aligned}
a_2^{HZZ} &= -2(2g_{HZZ}^{(2)} + g_{HZZ}^{(1)}) \\
&= -\frac{2e}{m_W \sin\theta_W}(d\cos^2\theta_W + d_B \sin^2_{\theta_W} + \Delta g_1^Z \cos 2\theta_W + \Delta_{\kappa_\gamma}\tan^2\theta_W), \qquad (4.17)\\
a_3^{HZZ} &= 2(2\tilde{g}_{HZZ}^{(2)} + \tilde{g}_{HZZ}^{(1)}) = \frac{2e}{m_W \sin\theta_W}(\tilde{d}\cos^2\theta_W + \tilde{d}_B \sin^2_{\theta_W} + \tilde{\kappa_\gamma}\tan^2\theta_W), \qquad (4.18)\\
a_2^{HWW} &= -2(2g_{HWW}^{(2)} + g_{HWW}^{(1)}) = -\frac{2e}{m_W \sin\theta_W}(d + \cos^2\theta_W \Delta g_1^Z), \qquad (4.19)\\
a_3^{HWW} &= 2\tilde{g}_{HWW}^{(2)} = \frac{2e}{m_W \sin\theta_W}\tilde{d}. \qquad (4.20)
\end{aligned}
$$

The third parameterization which `VBFNLO` supported is described in Ref. [20, 73, 79], the effective Lagrangian is

$$
\mathcal{L}_{eff} = \frac{f_{WW}}{\Lambda_6^2}\mathcal{O}_{WW} + \frac{f_{BB}}{\Lambda_6^2}\mathcal{O}_{BB} + \frac{f_W}{\Lambda_6^2}\mathcal{O}_W + \frac{f_B}{\Lambda_6^2}\mathcal{O}_B + \text{CP-odd part} \qquad (4.21)
$$

where the operator $\mathcal{O}$ is defined in dimension 6. The above Lagrangian can be written as

$$
\begin{aligned}
\mathcal{L}_{eff} = \frac{em_W}{\sin\theta_W \Lambda_6^2}\Big[&-\frac{\sin^2\theta_W}{2}(f_{BB} + f_{WW})HA_{\mu\nu}A^{\mu\nu} + \frac{\sin\theta_W}{2\cos\theta_W}(f_W - f_B)A_{\mu\nu}Z^\mu\partial^\nu H \\
&+ \tan\theta_W(\sin^2\theta_W f_{BB} - \cos^2\theta_W f_{WW})HA_{\mu\nu}A^{\mu\nu} \\
&+ \frac{1}{2\cos^2\theta_W}(\cos^2\theta_W f_W + \sin^2\theta_W f_B)Z_{\mu\nu}Z^\mu\partial^\nu H \\
&- \frac{1}{2\cos^2\theta_W}(\sin^4\theta_W f_{BB} + \cos^4\theta_W f_{WW})HZ_{\mu\nu}Z^{\mu\nu} \\
&+ \frac{1}{2}f_W(W^+_{\mu\nu}W^-_- + W^-_{\mu\nu}W^\mu_+)\partial^\nu H - f_{WW}HW^+_{\mu\nu}W^\mu_-\Big] + \text{CP-odd part.} \qquad (4.22)
\end{aligned}
$$

Here are the parameters in Eq. 4.13-4.16 can be related as

$$d = -\frac{m_W^2}{\Lambda_6^2} f_{WW}, \quad d_B = -\frac{m_W^2}{\Lambda_6^2} \tan^2\theta_W f_{BB}, \tag{4.23}$$

$$\Delta\kappa_\gamma = \frac{m_W^2}{2\Lambda_6^2}(f_B + f_W), \quad \Delta g_1^Z = \frac{m_W^2}{2\Lambda_6^2} f_W, \tag{4.24}$$

$$\tilde{d} = -\frac{m_W^2}{\Lambda_6^2} \tilde{f}_{WW}, \quad \tilde{d}_B = -\frac{m_W^2}{\Lambda_6^2} \tan^2\theta_W \tilde{f}_{BB}, \tag{4.25}$$

$$\tilde{\kappa}_\gamma = \frac{m_W^2}{2\Lambda_6^2} \tilde{f}_B \tag{4.26}$$

The form factor a_i is given by the following equations,

$$a_2^{HZZ} = \frac{2em_W}{\Lambda_6^2 \sin\theta_W}\Big[\cos^2\theta_W f_{WW} + \Big(\tan^2\theta_W - \sin^2\theta_W\Big) f_{BB} - \frac{1}{2} f_W - \frac{1}{2\tan^2\theta_W} f_B\Big], \tag{4.27}$$

$$a_3^{HZZ} = -\frac{2em_W}{\Lambda_6^2 \sin\theta_W}\Big[\cos^2\theta_W \tilde{f}_{WW} + \Big(\tan^2\theta_W - \sin^2\theta_W\Big) \tilde{f}_{BB} - \frac{1}{2} f_W - \frac{1}{2\tan^2\theta_W} \tilde{f}_B\Big], \tag{4.28}$$

$$a_2^{HWW} = \frac{2em_W}{\Lambda_6^2 \sin\theta_W}\Big(f_{WW} - \frac{1}{2} f_W\Big), \tag{4.29}$$

$$a_2^{HWW} = -\frac{2em_W}{\Lambda_6^2 \sin\theta_W} \tilde{f}_{WW}, \tag{4.30}$$

Again, in the above formulas, only the terms involving in HWW and HZZ vertex is shown.

4.2 Leading Order Calculation

The calculation of the SM Higgs boson plus jets production has been implemented in `VBFNLO` by Prof. Terrance Figy [5, 22]. For the generic process of Higgs boson plus three jets,

$$q(p_1) + Q(p_3) \to q(p_2) + Q(p_4) + g(q) + H(P), \tag{4.31}$$

the born amplitude can be decomposed into two color structures: the gluon emission off the 21 quark line $\mathcal{M}_{B,21}$ and the gluon emission off the 43 quark line $\mathcal{M}_{B,43}$, as shown in

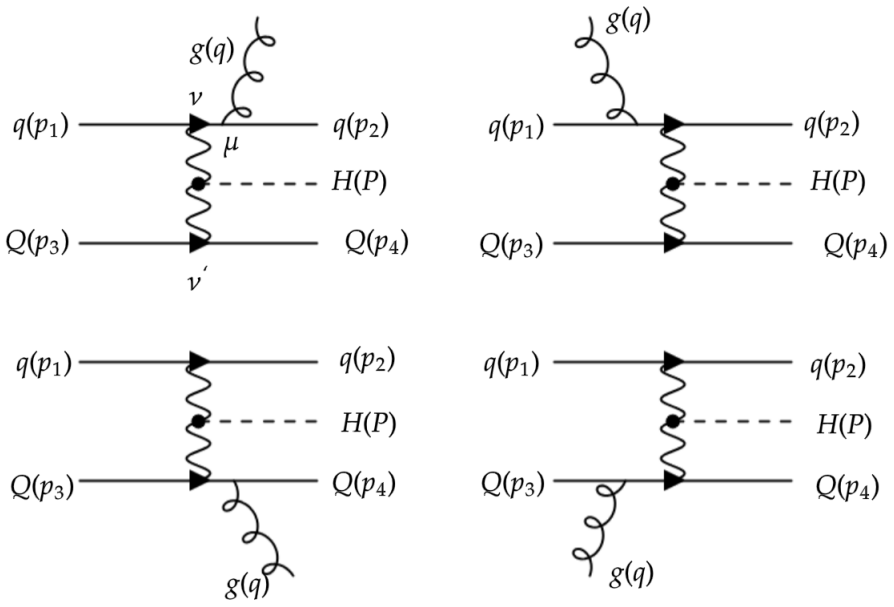

Figure 4.1: Feynman diagrams for $Hjjj@LO$, which the gluon emits from 21 quark line (top row) and emits from 43 quark line (bottom row). The straight line represents quark, the wavy line represents gauge boson (W, Z), the dotted line represents the Higgs boson, and the curly line represents gluon. The black dot represents the HVV vertex.

Fig. 4.1,

$$\mathcal{M}_B(p_1 i_1, p_2 i_2, p_3 i_3, p_4 i_4, q, a) = t^a_{i_2 i_1} \delta_{i_4 i_3} \mathcal{M}_{B,21} + t^a_{i_4 i_3} \delta_{i_2 i_1} \mathcal{M}_{B,43}. \tag{4.32}$$

Here the index a is the color index for gluon, i_1, i_2, i_3, i_4 is the color index for the external quarks, which has the momenta p_1, p_2, p_3, p_4. Also,

$$\mathcal{M}_{B,21} = \mathcal{M}_{B,21}(p_2, q, p_1; p_4, p_3) = \mathcal{M}^{\mu}_{B,21} \epsilon_{\mu}, \tag{4.33}$$

$$\mathcal{M}_{B,43} = \mathcal{M}_{B,43}(p_4, q, p_3; p_2, p_1) = \mathcal{M}^{\mu}_{B,43} \epsilon_{\mu}, \tag{4.34}$$

where ϵ_μ is the polarization vector of the external gluon. The momentum of the gluon is represented by q. Here p_1 is incoming and p_2 is outgoing and the momenta flow is chosen to point in the direction of the arrow in all diagrams. On the other hand, all boson

momenta (q for gluons, k_i for vector bosons where $i = 1, 2$) are chosen to be outgoing.

To calculate the color sub-amplitude which is shown in the top row of Fig. 4.1, one could cut the diagram into two parts: the upper part which contains the 21 quark line with gluon emission and attach the vector boson V_1 with the momentum k_1, the lower part which contains the 43 quark line and attaches the vector boson V_2 with momentum k_2. Both upper parts and lower parts can be calculated separately by applying the Feynman rules in Fig. 2.1 and Fig. 2.3 and then applying the Feynman rules for HVV vertex in Fig. 2.2 (for SM case). The upper part reads

$$\mathcal{M}^{\mu}_{B,21,upper} = -e\bar{\psi}(p_2)g_s\gamma^{\mu}g^{Vf_2f_1}_{\tau_1}[\gamma^{\nu}P_{\tau_1}\frac{(\not{p}_2+\not{k}_1)}{(p_2+k_1)^2}\gamma^{\mu}+\gamma^{\mu}\frac{(\not{p}_2+\not{q})}{(p_2+q)^2}\gamma^{\nu}P_{\tau_1}]\psi(p_1)D_{V_1}(k_1^2), \tag{4.35}$$

where $k_1 = p_1 - q - p_2$, and the chirality projector is $P_{\tau} = \frac{1}{2}(1 + \tau\gamma_5)$. The $\frac{(\not{p}_2+\not{k}_1)}{(p_2+k_1)^2}$ and $\frac{(\not{p}_2+\not{q})}{(p_2+q)^2}$ denotes the quark propagators. The vector boson propagator is

$$D_V(q^2) = \begin{cases} \frac{1}{k^2-m_V^2}, & k^2 - m_V^2 < 0 \\ \frac{1}{k^2-m^2+im_V\Gamma_V}, & k^2 - m_V^2 > 0 \end{cases} \tag{4.36}$$

The lower part is

$$\mathcal{M}^{\mu}_{B,21,lower} = -e\bar{\psi}(p_4)g^{Vf_4f_3}_{\tau_3}\gamma^{\nu'}P_{\tau_3}\psi(p_3)D_{V_2}(k_2^2), \tag{4.37}$$

where $k_2 = p_3 - p_4$. Then combine the $\mathcal{M}^{\mu}_{B,21,upper}$ and $\mathcal{M}^{\mu}_{B,21,lower}$ by applying the SM HVV Feyman rule, $g^{\nu\nu'}$, the final results reads,

$$\begin{aligned}\mathcal{M}^{\mu}_{B,21} = e^2 g^{Vf_2f_1}_{\tau_1}g^{Vf_4f_3}_{\tau_3}g_{HVV}g_s\bar{\psi}(p_2)[\gamma^{\nu}P_{\tau_1}\frac{(\not{p}_2+\not{k}_1)}{(p_2+k_1)^2}\gamma^{\mu} \\ + \gamma^{\mu}\frac{(\not{p}_2+\not{q})}{(p_2+q)^2}\gamma^{\nu}P_{\tau_1}]\psi(p_1)\bar{\psi}(p_4)\gamma_{\nu}P_{\tau_3}\psi(p_3)D_{V_1}(k_1^2)D_{V_2}(k_2^2),\end{aligned} \tag{4.38}$$

Similarly, for the gluon emission off the 43 quark line that is shown as the bottom row of

Feynman diagrams in Fig. 4.1, the sub-amplitude can be written as

$$\mathcal{M}^{\mu}_{B,43} = e^2 g^{Vf_2f_1}_{\tau_1} g^{Vf_4f_3}_{\tau_3} g_{HVV} g_s \bar{\psi}(p_4)[\gamma^{\nu} P_{\tau_3} \frac{(\not{p}_4 + \not{k}_2)}{(p_4+k_2)^2}\gamma^{\mu} + \gamma^{\mu}\frac{(\not{p}_4 + \not{q})}{(p_4+q)^2}\gamma^{\nu} P_{\tau_3}]\psi(p_3)\bar{\psi}(p_2)P_{\tau_1}\psi(p_1)D_{V_1}(k_1^2)D_{V_2}(k_2^2), \tag{4.39}$$

where $k_1 = p_1 - p_2, \quad k_2 = p_3 - q - p_4$.

4.3 The Helicity Amplitude Method

In `VBFNLO`, the LO matrix element can be calculated by using the helicity amplitude formalism [80]. Physical particles in a process may have momenta with opposite signs to those in the corresponding Feynman diagrams. I will use the same notation as in Ref. [80], which denotes the physical momenta as $\bar{p}$, and then momentum flow in Feynman diagrams is $p_i = S_i \bar{p}_i$, with $S_i = +$ for quarks and $S_i = -$ for antiquarks. In helicity amplitude method, four component Dirac spinors $\psi(\bar{p}, \bar{\sigma})$ ($= u(\bar{p}, \bar{\sigma})$ or $v(\bar{p}, \bar{\sigma})$) can be expressed by two-component Weyl spinors $\psi_{\pm}$,

$$\psi_{\pm} = \begin{pmatrix} \psi_- \\ \\ \psi_+ \end{pmatrix}, \quad \bar{\psi} = (\psi_+^{\dagger}, \psi_-^{\dagger}), \tag{4.40}$$

where

$$\begin{aligned} u(\bar{p}, \bar{\sigma})_{\pm} &= \omega_{\pm\bar{\sigma}}(\bar{p})\chi_{\bar{\sigma}}(\bar{p}), \\ v(\bar{p}, \bar{\sigma})_{\pm} &= \pm\bar{\sigma}\omega_{\mp\bar{\sigma}}(\bar{p})\chi_{-\bar{\sigma}}(\bar{p}). \end{aligned} \tag{4.41}$$

The $\bar{\sigma}$ is the helicity of the fermion with $\bar{p}^\mu = (\bar{E}, \bar{p}_x, \bar{p}_y, \bar{p}_z)$, and $\chi_{\bar{\sigma}}(\bar{p})$ is the normalized helicity eigenspinor denote as,

$$\chi_+(\bar{p}) = [2|\bar{\mathbf{p}}|(|\bar{\mathbf{p}}| + \bar{p_z})]^{-1/2} \begin{pmatrix} |\bar{\mathbf{p}}| + \bar{p_z}) \\ \bar{p_x} + i\bar{p_y} \end{pmatrix}, \tag{4.42}$$

$$\chi_-(\bar{p}) = [2|\bar{\mathbf{p}}|(|\bar{\mathbf{p}}| + \bar{p_z})]^{-1/2} \begin{pmatrix} -\bar{p_x} + i\bar{p_y} \\ |\bar{\mathbf{p}}| + \bar{p_z}) \end{pmatrix}, \tag{4.43}$$

where

$$\omega_\pm(\bar{p}) = [\bar{E} \pm |\bar{\mathbf{p}}|]^{1/2} \tag{4.44}$$

Then both u and v spinors in the massless fermions limit that $\omega_-(\bar{p})$ vanishes can be expressed as

$$\psi(\bar{p}, \bar{\sigma})_\pm = S\delta_{\sigma,\pm}\sqrt{2\bar{E}}\chi_\sigma(\bar{p}), \tag{4.45}$$

in which $\sigma = S\bar{\sigma}$. For the helicity eigenstates, the shorthand notation corresponding to external fermion leg i is

$$\begin{aligned} |i\rangle &= \chi_{\sigma_i}(\bar{p}_i), \\ \langle i| &= \chi^\dagger_{\sigma_i}(\bar{p}_i). \end{aligned} \tag{4.46}$$

The emission of a vector boson V with momentum k and polarization vector e^μ, attached to the external fermion i, is described by

$$\begin{aligned} |k, i\rangle &= (\not{p}_i - \not{k}_i)_{-\sigma_i}(\not{\epsilon})_{\sigma_i}\chi_{\sigma_i}(\bar{p}_i)\frac{1}{(p_i - k)^2}, \\ \langle i, k| &= \chi^\dagger_{\sigma_i}(\bar{p}_i)(\not{\epsilon})_{\sigma_i}(\not{p}_i + \not{k})_{-\sigma_i}\frac{1}{(p_i + k)^2} \end{aligned} \tag{4.47}$$

Then the color sub-amplitude $\mathcal{M}_{B,21,lower}$ (see Eq. 4.37) can be written as

$$\mathcal{M}_{B,21,lower} = -eg_{\sigma_3}^{Vf_4f_3} S_4 S_3 \delta_{\sigma_4\sigma_3} 2\sqrt{\bar{p}_4^0 \bar{p}_3^0} D_{V_2}(k_2^2) \langle 4|3\rangle = F_1 j_{21,\nu'}, \tag{4.48}$$

where

$$F_1 = -eg_{\sigma_3}^{Vf_4f_3} S_4 S_3 \delta_{\sigma_4\sigma_3} D_{V_2}(k_2^2), \tag{4.49}$$

and the upper part of the color sub-amplitude (see Eq. 4.35[1]) can be written as

$$\begin{aligned}\mathcal{M}_{B,21,upper} &= -eg_s g_{\sigma_1}^{Vf_2f_1} S_2 S_1 \delta_{\sigma_2\sigma_1} 2\sqrt{\bar{p}_2^0 \bar{p}_1^0} D_{V_1}(k_1^2)[\langle 2| (\not{\epsilon})_{\sigma_1} |k_1, 1\rangle + \langle 2, k_1| (\not{\epsilon})_{\sigma_1} |1\rangle] \\ &= F_2 e_{21,\nu}, \end{aligned} \tag{4.50}$$

where

$$F_2 = -eg_s g_{\sigma_1}^{Vf_2f_1} S_2 S_1 \delta_{\sigma_2\sigma_1} D_{V_2}(k_1^2). \tag{4.51}$$

Then apply the HVV vertex in SM, the final expression for color sub-amplitude (see the top row of Fig. 4.1) is

$$\mathcal{M}_{B,21} = F_3 g^{\nu\nu'} e_{21,\nu} j_{21,\nu'} \tag{4.52}$$

where

$$F_3 = g_{HVV} F_1 F_2 = e^2 g_s g_{HVV} g_{\sigma_1}^{Vf_2f_1} g_{\sigma_3}^{Vf_4f_3} S_2 S_1 S_4 S_3 \delta_{\sigma_2\sigma_1} \delta_{\sigma_4\sigma_3} D_{V_1}(k_1^2) D_{V_2}(k_2^2) \tag{4.53}$$

For the anomalous couplings, apply the generalized tensor structure in Eq. 4.1, the

[1]Here I include the gluon polarization vector ϵ_ν.

CP-even contribution for color sub-amplitude is

$$\begin{aligned}\mathcal{M}_{B,21,even} &= F_3(k_1k_2g^{\nu\nu'} - k_2^{\nu}k_1^{\nu'})e_{21,\nu}j_{21,\nu'} \\ &= F_3(k_1k_2g^{\nu\nu'}e_{21,\nu}j_{21,\nu'} - e_{21,\nu}k_2^{\nu}j_{21,\nu'}k_1^{\nu'})\end{aligned} \tag{4.54}$$

and the CP-odd contribution for color sub-amplitude is

$$\mathcal{M}_{B,21,odd} = F_3\varepsilon^{\nu\nu'\rho\sigma}k_{1\rho}k_{2\sigma}e_{21,\nu}j_{21,\nu'}. \tag{4.55}$$

The $\mathcal{M}_{B,43}$ (see the bottom row of Fig. 4.1) can be calculated in a similar way, the upper part is

$$\mathcal{M}_{B,43,upper} = -eg_{\sigma_1}^{Vf_2f_1}S_2S_1\delta_{\sigma_2\sigma_1}2\sqrt{\bar{p}_2^0\bar{p}_1^0}D_{V_1}(k_1^2)\langle 2|1\rangle = F_2j_{43,\nu}, \tag{4.56}$$

and the lower part is

$$\begin{aligned}\mathcal{M}_{B,43,lower} &= -eg_sg_{\sigma_3}^{Vf_4f_3}S_4S_3\delta_{\sigma_4\sigma_3}2\sqrt{\bar{p}_4^0\bar{p}_3^0}D_{V_2}(k_2^2)[\langle 4|\,(\not{\epsilon})_{\sigma_3}\,|k_2,3\rangle + \langle 4,k_2|\,(\not{\epsilon})_{\sigma_3}\,|3\rangle] \\ &= F_1e_{43,\nu'}.\end{aligned} \tag{4.57}$$

The final expression for color sub-amplitude $\mathcal{M}_{B,43}$ (in SM) is

$$\mathcal{M}_{B,21} = F_3g^{\nu\nu'}j_{43,\nu}e_{43,\nu'}, \tag{4.58}$$

and for CP-even and CP-odd contributions,

$$\mathcal{M}_{B,43,even} = F_3(k_1k_2g^{\nu\nu'}j_{43,\nu}e_{43,\nu'} - j_{43,\nu}k_2^{\nu}e_{43,\nu'}k_1^{\nu'}) \tag{4.59}$$

$$\mathcal{M}_{B,43,odd} = F_3\varepsilon^{\nu\nu'\rho\sigma}k_{1\rho}k_{2\sigma}j_{43,\nu}e_{43,\nu'}. \tag{4.60}$$

4.4 Implementation in VBFNLO

VBFNLO is a Monte Carlo program designed to accurately simulate various processes in particle physics [21, 81, 82], which not only includes VBF process but also for single and double vector boson production with two jets, and the production of double and triple vector bosons along with a jet, all computed at the NLO precision. VBFNLO also contains the calculation of LO cross sections with an additional jet. Additionally, the program supports the simulation of CP-even and CP-odd VBF Higgs boson production with two jets at NLO QCD accuracy. The program also allows for the specification of arbitrary cuts and offers various scale choices. It supports the utilization of any available parton distribution function (PDF) set through the LHAPDF [83] library. The code was written in FORTRAN. To program the anomalous Higgs boson couplings associated with three jets, the following files are related to the calculation: qqhqq.F, qqh2q2g_me.F, qqh4q_me.F, hjjja.F, and Tmunu.F. Here the file hjjja.F calculates the anomalous couplings at LO , qqh2q2g_me.F and qqh4q_me.F calculates the real emission part, qqhqq.F calculate the matrix elements at born level and finite virtual correction, Tmunu.F is used to calculate the common factor involved in the calculation, i.e. vector boson propagators in Eq. 4.36. The source code of these subroutines are available in the GitHub repository: Anomalous Higgs Boson Couplings. In the following subsections, I will first introduce how to use built-in subroutines to compute the LO matrix element in the SM case. Then I will introduce the subroutine I developed to calculate the matrix element with anomalous couplings for LO, real emission, and virtual correction.

4.4.1 LO Calculation

For the external quarks in helicity eigenstates, one needs to calculate the bra or ket vectors, which is a shorthand notation for two-component spinors. The following subroutine is used:

- $psi0m(n_f, p_i^\mu, sign(i), \psi)$.

In this subroutine, the input will be n_f, which is the number of fermions that bra or ket vectors to be calculated; p_i^μ, which contains the momenta of the quarks; $sign(i)$, which indicates whether particle i is a quark or anti-quark. It will return to a complex array ψ containing a ket or bra vector respective to incoming or outgoing quarks. To attach the gluon to the quark line, it is possible to use the subroutine $bra2r$ or $ket2r$:

- $bar2r(\langle p_i|, chreal, p_i^\mu, sigma, q^\nu, \epsilon_\nu, \langle p_i+q|, (p_i+q)^\mu)$,
- $ket2r(|p_i\rangle, chreal, p_i^\mu, sigma, q^\nu, \epsilon_\nu, |p_i-q\rangle, (p_i-q)^\mu)$,

Here $chreal$ indicates whether one component of $\langle p|$ or $|p\rangle$ is real. $sigma$ is the helicity of the quark. q^μ is the momentum of the gluon, and ϵ_μ is the polarization vector of the gloun. The subroutines will return to new kets or bras that attach the gluon to the quark line with new momentum. After calculating the bras and kets, then one can calculate the current for the quark line, using the subroutine $curr6$:

- $curr(sigmax, \langle p_i|, p_i^\mu, |p_j\rangle, p_j^\mu, j^\mu_{p_ip_j})$,
- $curr6(sigmax, \langle p_i+q|, (p_i+q)^\mu, |p_j\rangle, p_j^\mu, j^\mu_{p_ip_j})$,

where $sigmax$ is the maximum value of the helicity for the current, $\langle k_i|$ and $|k_j\rangle$ should be the output of $pis0m$ with the momenta p_i^μ and p_j^μ, respectively. The output, $j^\mu_{p_ip_j}$, is current for quark line 21 without the gluon emission. In order to calculate the current with the gluon attached, the $\langle p_2|$ needs to be replaced by $\langle p_2+q|$, which is the output from $bra2r$.

Now all the building blocks for the calculation of the LO matrix elements are gathered. Then we can construct the matrix element by calculating the contraction of the current. For example, if we want to contract the current of the upper line e_{21}^μ to the lower line j_{21}^ν, in the SM case, it can be written as

$$g_{\mu\nu}e_{21}^\mu j_{21}^\nu = e_{21}^0 j_{21}^0 - e_{21}^1 j_{21}^1 - e_{21}^2 j_{21}^2 - e_{21}^3 j_{21}^3. \tag{4.61}$$

Then one can multiply the couplings involved in the process, $g_{HVV}, g^{Vf_1f_2}, g^{Vf_3f_4}, g_s$, and the propagator for vector boson $D_{V_1}(k_1^2)$, $D_{V_2}(k_2^2)$ to compute the matrix element.

To implement the anomalous couplings, besides the SM case, both CP-even and CP-odd terms in Eq. 4.1 should be calculated. This subroutine needs to modify the HVV vertex (the black dot in Fig. 4.1) and use the new tensor structure to evaluate the matrix element. Two existing subroutines have already been programmed, `contract_CPE` and `contract_CPO`, can contract the current i.e., e_{21}^{μ} and j_{21}^{ν} for CP-even and CP-odd cases.

- *contract_CPE*$(J_1T_1J_2, J_1, J_2, k_1, k_2)$,
- *contract_CPO*$(J_1T_2J_2, J_1, J_2, k_1, k_2)$.

Here the input will be the current J_1 for the upper part, J_2 for the lower part, k_1 for the momentum of the intermediate vector boson V_1 connected to the 21 quark line, and k_2 for the momentum of the intermediate vector boson V_2 connect to the 43 quark line. *contract_CPE* will return to the value for the CP-even term in Eq. 4.1, $J_1T_1J_2$. And the subroutine *contract_CPO* will return to the value for the CP-odd term in Eq. 4.1, $J_1T_2J_2$. I have developed a new subroutine, $hjjja$, to evaluate the born amplitude with anomalous Higgs boson couplings.

- $hjjja(J_{21}, J_{43}, E_{21}, E_{43}, p_{21}, p_{43}, p_{21,g}, p_{43,g},$
  $D_{V_{21}}, D_{V_{43}}, D_{V_{21,g}}, D_{V_{43,g}}, \mathcal{M}_{21}^{\mu}, \mathcal{M}_{43}^{\mu})$

The input will be the momentum entering the HVV vertex (i.e., $p_{21,g}, p_{43}$), the propagator of the gauge boson (i.e. $D_{V_{21,g}}$, $D_{V_{43}}$), and the calculated current for two quark lines (i.e. E_{21}, J_{21}). After execution, the subroutine will return to the sum of the matrix element for CP-even and CP-odd cases.

The code `anomHiggs.F` is programmed to read in the user input value for the anomalous couplings of HWW and HZZ from `anom_HVV.dat` and then use the Eq. 4.3 and Eq. 4.4 to calculate the numerical values for anomalous couplings. Besides the contraction of the current and the HWW and HZZ couplings, all the other building blocks are the

same as the SM case, so it is straightforward to modify the code snippet and implement the anomalous couplings under the current framework for the LO matrix element. To conclude the program structure for $Hjjj@LO$, first one needs to use $psi0m$ subroutine to define the external quarks, then use $bra2c$ or $ket2c$ to attach the gluon emission to one of the external quark legs. The next step is to use $curr6$ to calculate the quark current with the emission of the gluon (i.e., the upper part shown in Fig. 4.2), and also the quark current without the gluon emission (i.e., the lower part shown in Fig. 4.2). By applying the *contract_CPE* and/or *contract_CPO* to the quark current already calculated in the previous step, and multiply couplings and vector boson propagators (i.e., g_{HVV}, g_{Vff} and $D_V(k^2)$), the color subamplitude is constructed. In Fig 4.2, all the construction subroutines are labeled in different colors and use different rectangles to demonstrate the calculations.

4.4.2 Real Emission

In order to construct the NLO calculation for the Higgs boson plus three jets ($Hjjj@NLO$), one also needs to implement the anomalous Higgs boson couplings to the real emission part. The real emission subroutine in `VBFNLO` was originally developed by Prof. Terrance Figy [5, 51] for SM and was modified by Dr. Michael Rauch to improve the efficiency of the calculation. There are two files programmed for the real emission: `qqh4q_me.F` and `qqh2q2g_me.F`, where `qqh4q_me.F` calculate the matrix element squared for four quarks in the final state and `qqh2q2g_me.F` calculate the matrix element squared for two quarks and two gluons in the final state. Since there are some common factors during the evaluation of the matrix elements, such as couplings and the propagators for vector bosons, I have created the following subroutines in `Tmunu.F` to calculate the anomalous part of the matrix element:

- $contract\_TmnZZ(J_1, J_2, k_1, k_2, J_1TJ_2Z)$,
- $contract\_TmnWW(J_1, J_2, k_1, k_2, J_1TJ_2W)$.

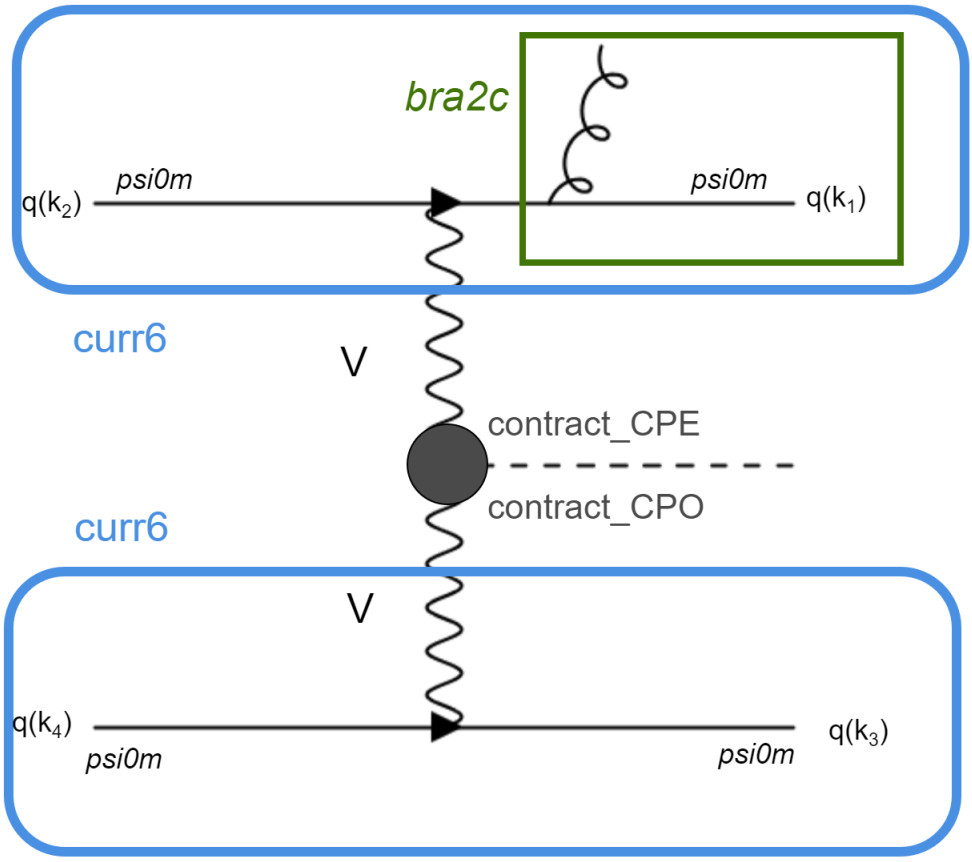

Figure 4.2: This figure shows the construction of the $Hjjj@LO$ with anomalous couplings, where the curly line represents gluon and the dotted line represents Higgs boson.

The subroutine *contract_TmnZZ* contracts the current using the generalized tensor structure in Eq. 4.1 and multiplies by the corresponding Z boson propagators. The input value would be the current J_1, J_2, and the momentum of Z boson k_1 and k_2. The structure of subroutine *contract_TmnWW* is similar to *contract_TmnZZ*, which uses the HWW anomalous couplings and the propagators for W boson.

For the subprocess to have two gluons and two quarks in the final state, the current is categorized into three categories: the current of the quark line attached to one gluon as shown in Fig. 4.3; and the current of quark line attached with two gluons as shown in Fig. 4.4; one intermediate gluon attach the quark line and emits to gluons as shown in

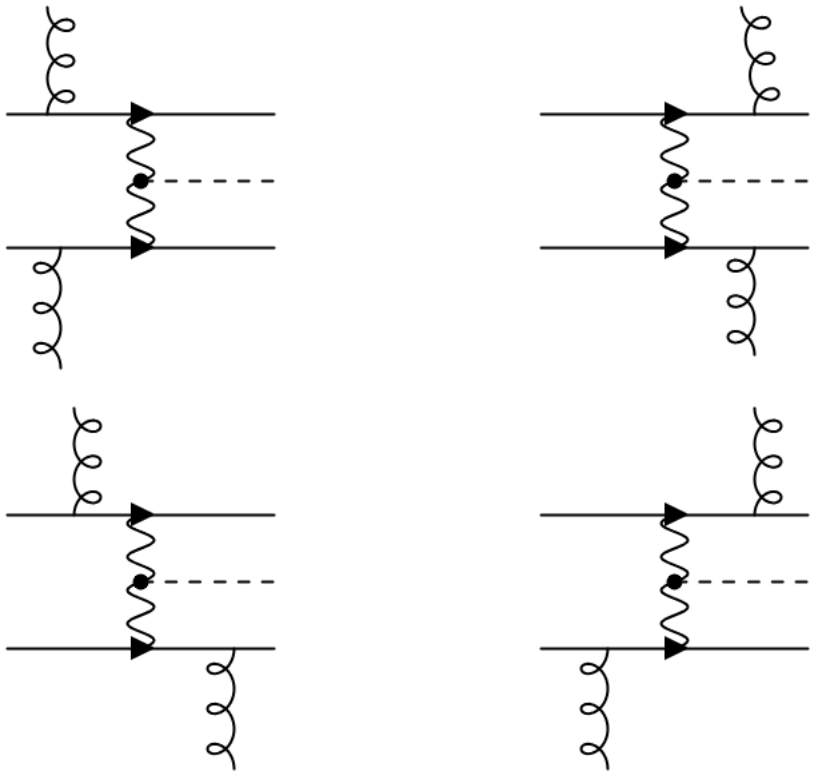

Figure 4.3: Feynman diagrams for the real emission of $Hjjj@NLO$ process that an external gluon attached to both quark lines. The straight line represents quark, the wavy line represents gauge boson (W, Z), the dotted line represents the Higgs boson, and the curly line represents gluon. The black dot represents the HVV vertex.

Fig. 4.5. For Fig 4.3, I did not label the gluon with different letters. In the subroutine, two gluons have different polarization vectors, which means there could be six Feynman diagrams to consider. Fig. 4.4 and Fig. 4.5 only show Feynman diagrams for one possibility, which gluons are emitted from the upper quark line, another possibility would be the gluon emitted from the lower line. These currents can be evaluated using the subroutine *curr*6 with the corresponding inputs. There are six combinations for the current contraction, and each one needs to be programmed for the anomalous part.

For the subprocess to have four quarks in the final state, there are two types of current, one is the quark line without radiation, another is the quark line attached to the intermediate gluon and the two quarks in the final state. To contract the current, there are

four combinations: radiation from the upper line, radiation from the lower line, and the interchange of the quark index between the initial and final states. By applying the subroutine *contract_TmnZZ* and *contract_TmnWW*, the contribution of the anomalous part can be computed and added to the SM matrix elements as Eq. 4.1.

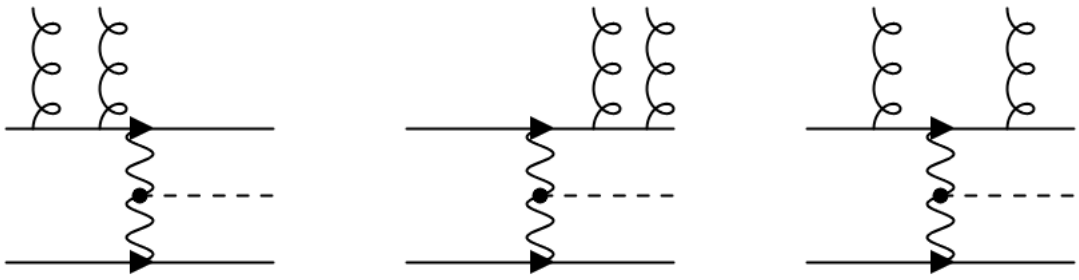

Figure 4.4: Feynman diagrams for the real emission of $Hjjj@NLO$ process that two external gluons attached to one quark line.

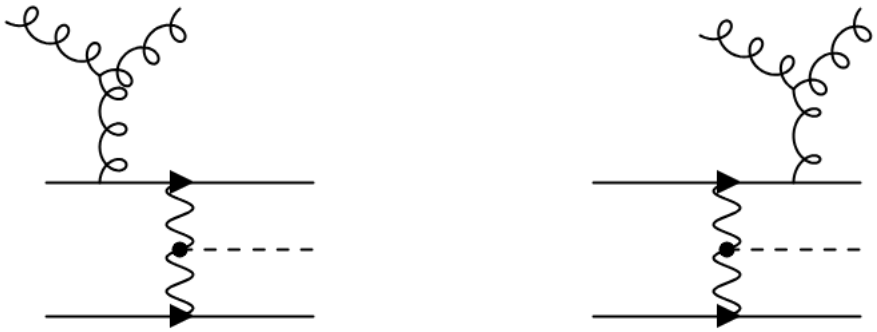

Figure 4.5: Feynman diagrams for the real emission of $Hjjj@NLO$ process that two gluons emission from the same quark line. The straight line represents quark, the wavy line represents gauge boson (W, Z), the dotted line represents the Higgs boson, and the curly line represents gluon. The black dot represents the HVV vertex.

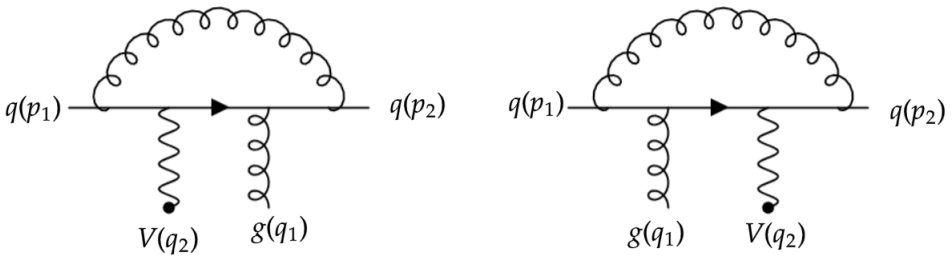

Figure 4.6: Example Feynman diagrams for the progress $q\bar{q} \to Vg$. The straight line represents quark, the wavy line represents gauge boson (W, Z), and the curly line represents gluon. The black dot represents the HVV vertex. A complete set of Feynman diagrams can be found in Ref. [5].

4.4.3 Virtual Correction

The subroutine `coeff.F` is been used to calculate the virtual correction.

- *boxline_vg* $(\psi_1, \psi_2, p_1, p_2, isig, \epsilon^\mu, J, q_1, q_2, \mathcal{M}_\mathcal{B}, \mathcal{M}_{box})$

The subroutine needs the momenta p_1 and p_2, and their spinor ψ_1 and ψ_2; the momenta of the vector boson q_2, and the corresponding quark line current J. Furthermore, the momenta of gluon q_1 and its polarization vector ϵ^μ, and the helicity $isig$ of the quark line has to be given to the subroutine to compute the matrix element of the virtual correction $\mathcal{M}_{box}$. Compared to the SM case, there are two input needs to be modified, current J and $\mathcal{M}_\mathcal{B}$. In the calculation of the CP-even contribution, I have created subroutines *contract_CPEJ1* and *contract_CPEJ2* to calculate the current J for the boxline subroutine:

- contract_CPEJ1(J_1, J_1^μ, p_1, p_2)
- contract_CPEJ2 (J_2, J_2^μ, p_1, p_2)

Similarly to the born level amplitude calculation, there are two parts for the virtual correction, $\mathcal{M}^\mu_{V_{21}}$ and $\mathcal{M}^\mu_{V_{43}}$. Since the position of the input variable is a one-to-one mapping to the values, it is important to write two separate subroutines for each calculation. *contract_CPEJ1* is used for $\mathcal{M}^\mu_{V_{21}}$ and *contract_CPEJ2* is used for $\mathcal{M}^\mu_{V_{43}}$. For the CP-odd contribution, I used the existing subroutine *epscrr*.

- *epscrr*($D^\mu, A^\alpha, B^\beta, C^\rho$)

It will return to the value for the current as the input for the boxline subroutine. Additionally, the born amplitude can be evaluated by using *contract_CPE* and *contract_CPO* subroutine.

CHAPTER 5
TESTS AND COMPARISONS

In this chapter, I will perform different validation checks on the code and show the results. For Higgs boson production associated with three jets at LO, I compare it to the tested Higgs boson production with two jets and add an additional jet. The dipole subtraction check is used for the real part and the gauge invariance test is used for the virtual part. The last check will be the relation between real emissions and virtual corrections.

5.1 LO Check

In order to confirm the born-level matrix elements are programming correctly, one needs to test the results for the calculation of $Hjjj@LO$. In `VBFNLO`, the feature to add one LO additional jet is used for this test. Since the anomalous couplings for Higgs plus two jets at NLO have been implemented and examined [23], I can compare the cross section for Higgs plus three jets at LO to the Higgs plus two jets with one additional LO jet. The results are shown in Tab. 2.

Table 2: This table shows the cross section for the Higgs boson plus two jets with additional LO jets and the Higgs boson plus three jets at LO.

LO	$\sigma_{CP-even}$[fb]	σ_{CP-odd}[fb]	$\sigma_{CP-mixed}$ [fb]
$Hjj@LO + jet$	670.39519 ± 0.20182	512.86790 ± 0.14043	1183.48762±0.34811
$Hjjj@LO$	670.35567 ± 0.20059	512.88934 ± 0.14028	1183.42227±0.34675

In this test, the parameters for the anomalous couplings are set for three different cases: $g_{5e}^{HWW} = g_{5e}^{HZZ} = 0.5$ for CP-even case; $g_{5o}^{HWW} = g_{5o}^{HZZ} = 0.5$ for CP-odd case; $g_{5e}^{HWW} = g_{5e}^{HZZ} = g_{5o}^{HWW} = g_{5o}^{HZZ} = 0.5$ for CP-mixed case, and all other parameters equals zero. As shown in Tab. 2, each column compares the results of the cross section with the Monte Carlo error between the $Hjjj@LO$ and $Hjj@LO$ with one additional jet. All results show that the $Hjjj@LO$ cross section agrees with the cross section for $Hjj@LO$ with one additional jet within the Monte Carlo error. This indicates that the implementation at the Born-level is validated.

5.2 Dipole Subtraction Check

Since dipole subtraction is used to perform numerical calculations involved in the NLO calculation, one can compare the matrix elements square for the real emission and the subtraction term. In the formalism of Catani and Seymour subtraction method, the subtraction terms $d\sigma^A$ act as local counter terms. Thus, they have to exactly cancel the real emission contribution in the singular regions. This property of the subtracted dipoles has been tested numerically for the real emission of the $Hjjj@NLO$ after the implementation of anomalous coupling. In order to confirm the cancellation of collinear singularities, the comparison is made for the individual phase points by taking the ratio of subtraction term and real emission matrix elements squared, $|\mathcal{M}_{sub}|^2/|\mathcal{M}_{real}|^2$. The subroutine written by Michael Raunch was used to make this dipole subtraction check. The $|\mathcal{M}_{sub}|^2/|\mathcal{M}_{real}|^2$ is plotted over the scalar products between the momentum of the quark momentum p_i where $i = 1, 2, 3, 4$ and the gluon momentum p_j where $j = 5, 6$. From the plots, most points were around the line $|\mathcal{M}_{sub}|^2/|\mathcal{M}_{real}|^2 = 1$. As $p_i \cdot p_j \to 0$, the subtraction terms can cancel the real emission contributions resulting in a ratio of real emission cross section divided by dipole cross sections of one. This shows that the dipole method works.

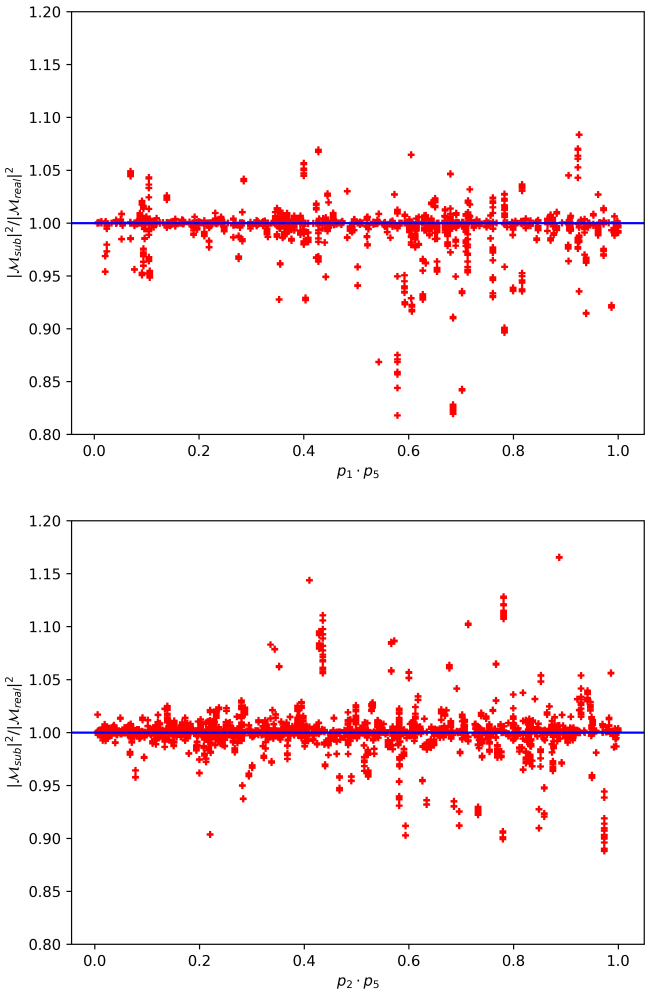

Figure 5.1: Ratio of the real emission matrix element and the subtraction dipoles, in the limits $p_1 \cdot p_5 \to 0$ (left panel) and $p_2 \cdot p_5 \to 0$ (right panel).

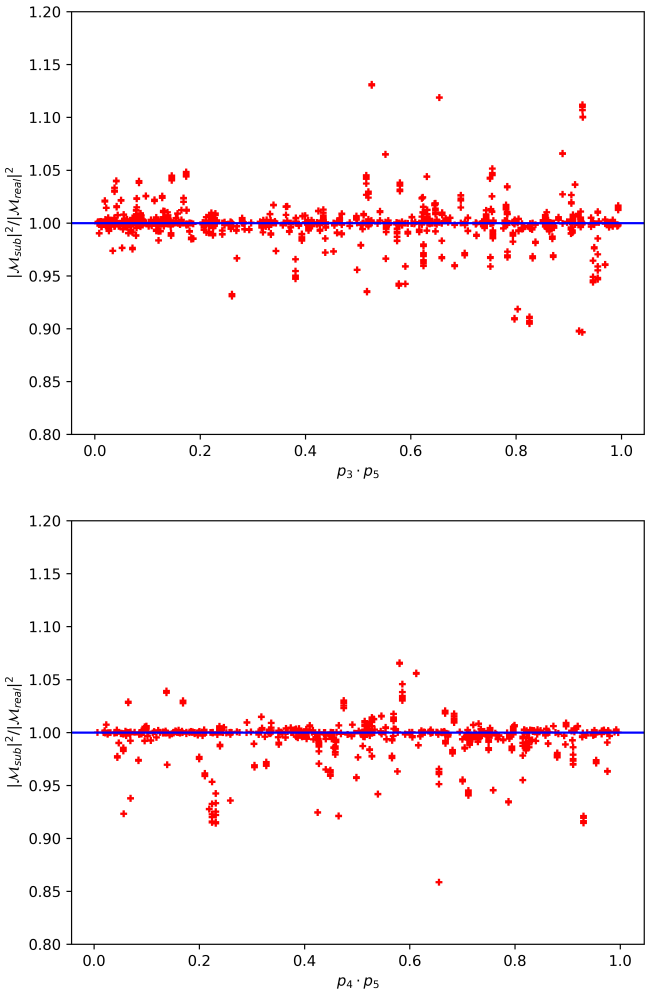

Figure 5.2: Ratio of the real emission matrix element and the subtraction dipoles, in the limits $p_3 \cdot p_5 \to 0$ (left panel) and $p_4 \cdot p_5 \to 0$ (right panel).

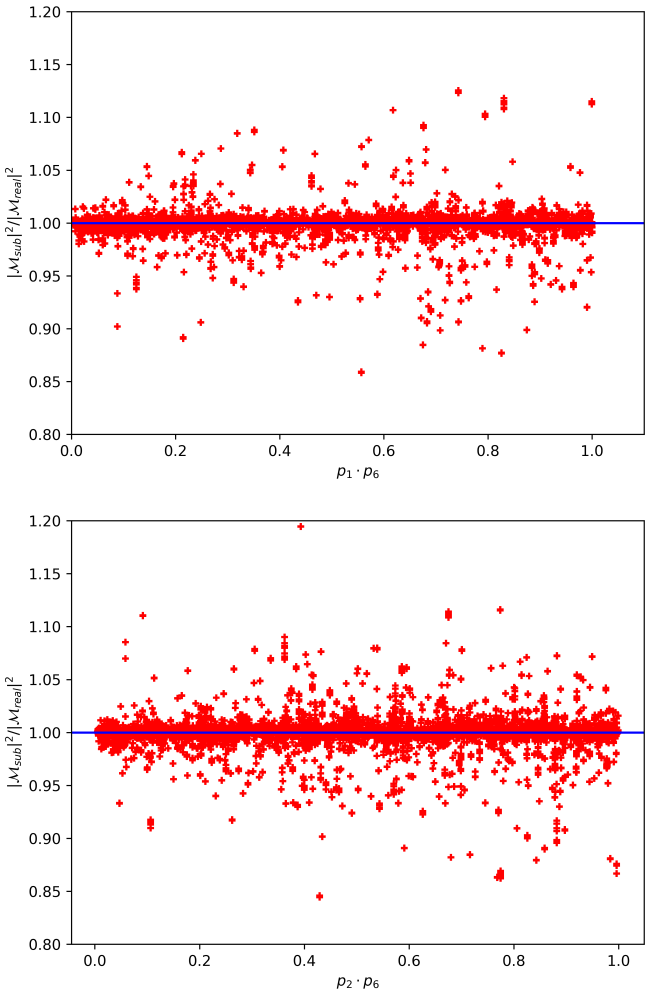

Figure 5.3: Ratio of the real emission matrix element and the subtraction dipoles, in the limits $p_1 \cdot p_6 \to 0$ (left panel) and $p_2 \cdot p_6 \to 0$ (right panel).

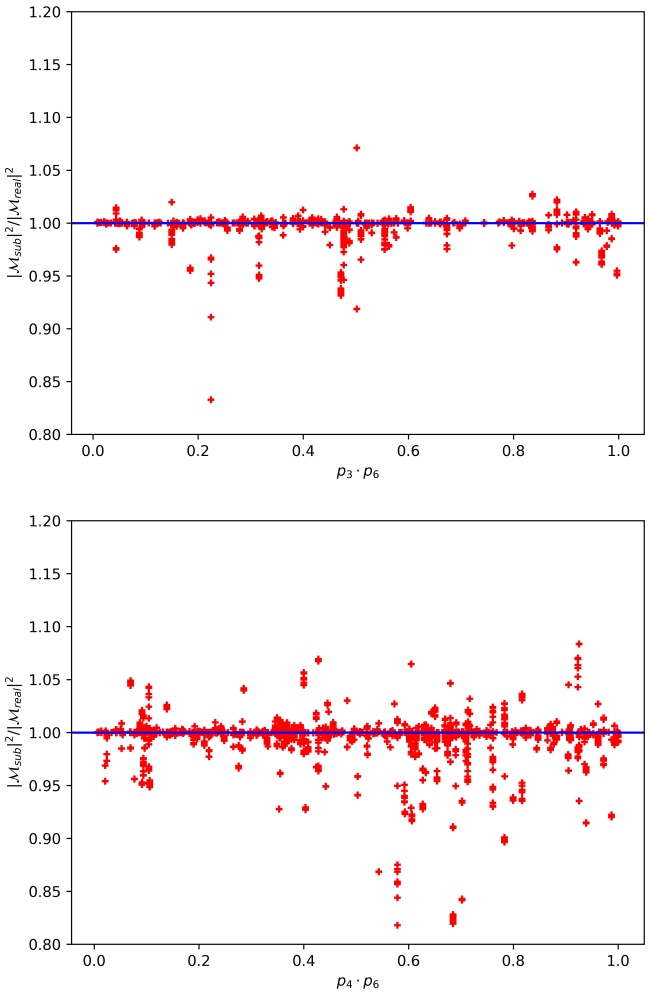

Figure 5.4: Ratio of the real emission matrix element and the subtraction dipoles, in the limits $p_3 \cdot p_6 \to 0$ (left panel) and $p_4 \cdot p_6 \to 0$ (right panel).

5.3 Gauge Invariance Check for Virtual Correction

The virtual contributions can be tested using the property of gauge invariance. For a single diagram, it is not gauge invariant by itself, but the sum of all diagrams contributing to the matrix element is gauge invariant. The Ward identity [84, 85] can be used to test the implementation of the virtual corrections. A solid proof of the Ward identity can be found in Ref. [86]. The virtual matrix element $\mathcal{M}_{virt}$ will be vanished if one replaced the polarization vector ϵ_μ to the momentum p_μ,

$$\epsilon_\mu \mathcal{M}^\mu_{virt} \to p_\mu \mathcal{M}^\mu_{virt} \tag{5.1}$$

This test was programmed to check two parts of virtual correction, $\mathcal{M}^V_{21}$ and $\mathcal{M}^V_{43}$ individually. The original debug code was developed by Prof. Terrance Figy. The histogram was made by taking the ratio of $\mathcal{M}^V_{21}$ to the matrix element $\mathcal{M}_{21}$ and $\mathcal{M}^V_{43}$ to the matrix element $\mathcal{M}_{43}$ for about 500,000 data points. Fig. 5.5 shows the results of the gauge check. On the right panel shows the check for the $\mathcal{M}^V_{21}/\mathcal{M}_{21}$ and the right panel shows the check for $\mathcal{M}^V_{43}/\mathcal{M}_{43}$. From these two histograms, it shows that most of the data points were around 10^{-12}, and this indicated that gauge invariance was satisfied for the virtual correction.

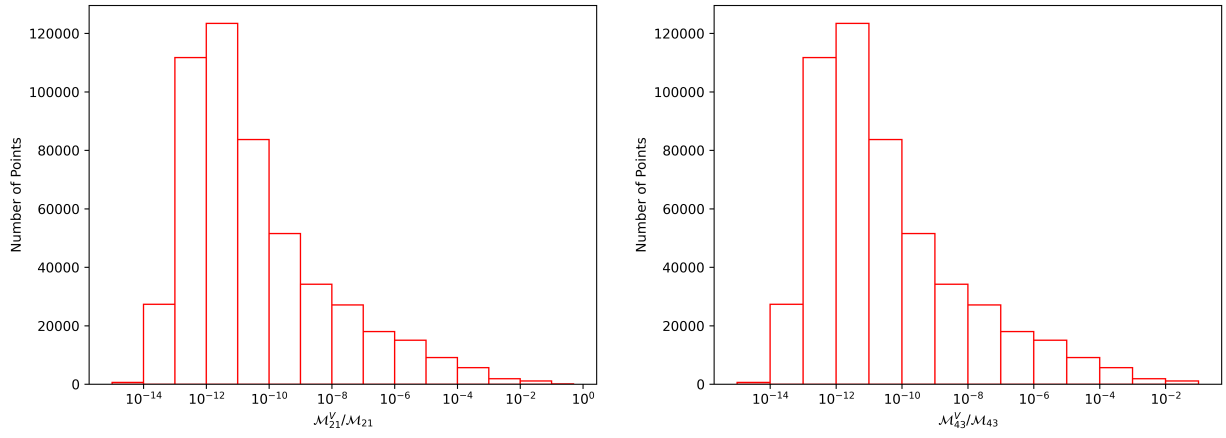

Figure 5.5: Gauge check for virtual corrections.

5.4 Relation Between Real Emission and Virtual Correction

In this section, I will use the properties based on the subtraction method, which is possible to integrate real emission and virtual corrections proportional to the born term. There are two constants that are important to Higgs plus three jets production process: c_{virt} and c_{real}. The sum of these two constants, c_{sum}, should be fixed,

$$c_{sum} = c_{virt} + c_{real} = \frac{\pi^2}{3} - 8 + \frac{2\pi^2}{3} - \frac{13}{2} = \pi^2 - \frac{29}{2}. \tag{5.2}$$

By varying the c_{virt} and c_{real} to different values but keeping the c_{sum} fixed, the NLO cross section should stay the same. The results are shown in Tab. 3. In order to testify the CP-even anomalous couplings, I used the parameter which $g_{5e}^{HWW} = g_{5e}^{HZZ} = 0.5$ for CP-even case, $g_{5o}^{HWW} = g_{5o}^{HZZ} = 0.5$ for CP-odd case, and $g_{5e}^{HWW} = g_{5e}^{HZZ} = g_{5o}^{HWW} = g_{5o}^{HZZ} = 0.5$ for CP-mixed case. All other parameters not specified are zero.

After giving two constants, c_{virt} and c_{real}, for a different value, the total cross section for NLO results is agreed within the numerical error of the Monte Carlo event generator. This confirms that the finite part of the virtual corrections and the real emissions are correct.

Table 3: This table shows the NLO cross section for the Higgs boson plus three jets in three different CP scenarios. Given the different constant c_{virt} and c_{real}, their sum c_{sum} is fixed.

c_{virt}	c_{real}	c_{sum}	$\sigma_{CP-even}$ [fb]	σ_{CP-odd} [fb]	σ_{CP-mix} [fb]
$\frac{\pi^2}{3} - 8$	$\frac{2\pi^2}{3} - \frac{13}{2}$	$\pi^2 - \frac{29}{2}$	595.843598± 7.609827	280.345733± 1.502138	884.456846± 10.910300
$\frac{4\pi^2}{3} - 14$	$-\frac{\pi^2}{3} - \frac{1}{2}$	$\pi^2 - \frac{29}{2}$	602.168175± 7.367263	278.451237± 1.502102	877.085241± 10.064846
-6	$\pi^2 - \frac{17}{2}$	$\pi^2 - \frac{29}{2}$	592.121609± 6.532743	282.803893± 1.208810	893.547709± 6.771830

CHAPTER 6
PHENOMENOLOGY

After developing the anomalous Higgs boson couplings associated with three jets, I can perform the simulation of merged and matched setup in VBF using the HERWIG 7. In this chapter, starting with the introduction to HERWIG 7 and input parameters, three selection cuts will be defined. Then the results of CP-sensitive observables will be presented for merged and matched setup. I will show the results of different CP scenarios and compare the distribution of CP-sensitive observables for $h(2^\star, 3^\star, 4)$, $h(2^\star, 3)$, $h(2^\star) \bigoplus \text{PS}$, and NLO fixed order calculation. Finally, I will look at the comparison of SM results and three different CP scenarios.

6.1 Introduction

A hadron collider has a special axis called the beam axis. The beam axis is parallel to the incoming particles. Usually, the beam axis is chosen to be the z-axis. It is often convenient to describe the four-momentum of a particle by their energy and polar angle θ and azimuthal angle ϕ, where θ represents the angle of the particle with respect to the z-axis, φ is the angle around the beam axis [87].

The energies and momenta of incoming particles are known for particle physics experiments, but the energies and momentum fractions of the respective constituents that interact are not known in advance. The relative motion can be understood as a boost of the constituent system with respect to the lab or beam system. If the constituents move in parallel to the incoming particles, this implies that the overall momentum of the colliding constituents along the beam axis is essentially unknown. It is thus convenient to construct a quantity with good transformation properties under boosts along the beam axis such as rapidity y, transverse momentum p_T, and invariant mass $m_{j_1 j_2}$ [87].

HERWIG 7 [88] is a multi-purpose particle physics event generator. The current version is HERWIG 7.2.3, which is used in this research. It provides all the different simulation steps, such as hard process generation, parton shower, hadronization and

multiple parton interactions (MPI). In this dissertation, I did not include the hadronization and MPI in the simulation. Detailed information and tutorials can be obtained from the website: `https://herwig.hepforge.org/`. The description of computation and documentation can be found in the HERWIG 7.0 release note [88].

`LHC-Matchbox.in` [89] is the input file of the HERWIG 7 event generator. It is already structured in a way that guides the user through the choices for the hard processes [90]. A few "beam parameters" have been modified in this study: beam energy, settings for VBF approximation, selection of the process, selection of matrix element, and shower selection. The usage and a brief guide will be shown in Appendix. Also, the estimated running time for matched and merged setup on the HPC will be discussed in Appendix.

When the HERWIG 7 event generator generates events, a `yoda` file containing data is generated. `Rivet` [91] makes plots from the `yoda` file through the code "rivet-mkhtml". It has many options of plots such as ratio plots, legends, titles, labels, etc. Throughout this dissertation, `Rivet 2.7.2` was used to make plots. All analyses of Higgs production have been performed by `Rivet` .

6.2 General Monte Carlo Input Parameters

To examine the results of the anomalous coupling for the Higgs boson in different scenarios, the HERWIG 7 input parameters are set up in the `HJets-settings.in` file. The settings used are the same as in Ref. [35]. The mass and widths of Z^0 and $W^{\pm}$ gauge bosons are fixed to

$$m_Z = 91.1876 \text{ GeV}, \quad \Gamma_Z = 2.4952 \text{ GeV}, \tag{6.1}$$

$$m_w = 80.385 \text{ GeV}, \quad \Gamma_W = 2.085 \text{ GeV}. \tag{6.2}$$

The Fermi constant is $G_F = 1.16637 \times 10^{-5}$ GeV^{-2} and the G_μ scheme is used to derive the electromagnetic coupling constant and the weak mixing angle via Standard Model

tree-level relations. The Higgs boson mass is set to $m_H = 125.7$ GeV.

For renormalization and factorization scales, the following scale is used:

$$\mu_0 = \frac{1}{2} H_{T,\text{jets}} = \frac{1}{2} \sum_{i \in \text{jets}} p_{T,i}, \tag{6.3}$$

where $p_{T,i}$ is the transverse momentum of the i-th jet. In order to ensure the infrared safety of the scale choice, the anti-k_T jet clustering [92] was used with $R = 0.4$ in the inclusive mode. The recombination method is `E-scheme` and requires each jet to have $p_{T,i} > 5$ GeV. The collider energy $\sqrt{s} = 13$ TeV is used for all simulations. The parton distribution function is `PDF4LHC15_nnlo_100_pdfas` [93] in all simulations with `LHAPDF6` [83]. To be consistent with `PDF4LHC15_nnlo_100_pdfas` settings, the strong coupling constant was chosen as $\alpha_s(M_Z) = 0.118$ and used the five active flavors in the settings.

In order to optimize our analysis and ensure accurate results, there is a set of selection cuts applied for the hard processes involving jets before proceeding with the subsequent parton shower simulation. However, the selection cut at the event generation level is weaker than the analysis cut to ensure enough margin for the study. While in principle a cut may not be necessary for the lowest-order process involving two jets, the cuts are still employed for efficient reasons. On the other hand, other processes of the VBF/VBS kind do require the implementation of generation cuts even at the NLO for the lowest-order process.

To reconstruct jets from the final-state partons, the anti-k_t algorithm as described in the reference [92] and utilize the `fastjet` library [94]. In the inclusive mode, the jet radius parameter is $R = 0.4$ and adopts the `E-scheme` for the recombination method. The minimum transverse momentum required for all jets is set to 10 GeV, and the jet rapidity is constrained within $|y_j| \leq 5$. In scenarios where the lowest final-state parton multiplicity is two partons, such as $h(2^*, 3)$ or $h(2^\star) \bigoplus \text{PS}$, it requires a minimum of two jets.

6.3 Event Selection Cuts

The analysis utilizes the MC analysis toolkit `Rivet 2.7.2` [95] to analyze all simulated events. A specific analysis named `MC_H2JETS` has been developed within the `Rivet` framework, which implements three event selection criteria: inclusive cuts (INCL), tight cuts (TIGHT), and loose cuts (LOOSE).

To combine partons into jets, the anti-k_t algorithm [92] is employed with a radius parameter of $R = 0.4$ in the inclusive mode. The recombination of partons into jets follows the `E-scheme`. Valid jets are required to satisfy certain conditions regarding their transverse momentum $p_{T,j}$ and rapidity y_j. These conditions are as follows:

$$p_{T,j} > 25 \text{ GeV}, \quad |y_j| \leq 4.5. \tag{6.4}$$

The jets are ordered from largest to smallest in jet transverse momentum and labeled jets as j_k with $k = 1, 2, 3...$ being an index. For INCL selection cuts, it requires at least two jets in the event. For the LOOSE selection cuts, there is an additional selection criterion has been included,

$$m_{j_1 j_2} > 200 \text{ GeV}, \quad \Delta y_{j_1 j_2} > 1, \tag{6.5}$$

where $m_{j_1 j_2}$ is the invariant mass of the leading two jets. $\Delta y_{j_1 j_2}$ is the rapidity separation of the two hardest jets defined as $\Delta y_{j_1 j_2} = |y_{j_1} - y_{j_2}|$. For the TIGHT selection cuts, the following additional selection criterion is included,

$$m_{j_1 j_2} > 600 \text{ GeV}, \quad \Delta y_{j_1 j_2} > 4.5, \quad y_{j_1} \cdot y_{j_2} < 0. \tag{6.6}$$

6.4 CP Sensitive Observables

The anomalous HVV couplings will affect the distribution of the Higgs boson production through VBF at LHC. The CP structure of the HVV vertex can be revealed by studying the azimuthal angle between two jets. In general, the azimuthal angle between

the two hardest jets is defined as

$$|\Delta\phi_{j_1 j_2}| = |\phi_{j_1} - \phi_{j_2}| \tag{6.7}$$

The shape of $1/\sigma d\sigma/|\Delta\phi_{j_1 j_2}|$ is sensitive to the CP structure [23, 71]. As shown in Fig. 6.1 (top), I plot the distribution of $|\Delta\phi_{j_1 j_2}|$ for $h(2^\star) \bigoplus \mathrm{PS}$ for three cases: pure CP-even, pure CP-odd, and the CP-mixed. For the plots in this section, the anomalous couplings are:

- pure CP-even: $g_{5e}^{HWW} = g_{5e}^{HZZ} = 0.5$,
- pure CP-odd: $g_{5o}^{HWW} = g_{5o}^{HZZ} = 0.5$,
- CP-mixed: $g_{5e}^{HWW} = g_{5o}^{HWW} = g_{5e}^{HZZ} = g_{5o}^{HZZ} = 0.5$.

For all three CP scenarios, it is set that no SM contribution, i.e., $a_1 = 0$ in Eq. 4.1, and $\Lambda = 480$. The color legends for these distribution plots are red lines for the CP-mixed case, blue lines for the purely CP-even case, green lines for the purely CP-odd case, and orange lines for the SM case. The plots are made against the SM scenario so that the reference in each ratio plot is the SM results, and the distributions are normalized to compare three scenarios of anomalous couplings. The error bars shown in the figures are the Monte Carlo error. For purely CP-even couplings, the cross section is suppressed at 90 degrees, while for purely CP-odd couplings, the cross section is suppressed at 0 and 180 degrees. From the ratio plot in Fig. 6.1 (top), it is clear that purely CP-odd couplings have a peak at 90 degrees while purely CP-even couplings have a dip. The plot range is set from 0 to π since it calculated the absolute value of $\Delta\phi_{j_1 j_2}$. When both CP-even and CP-odd couplings of the same strength are present, i.e., in the CP-mixed case, the dips cancel out and result in a distribution without the characteristic curve. For the merged setup $h(2^\star, 3)$ and $h(2^\star, 3^\star, 4)$, there is a similar pattern shown in Fig. 6.2 and Fig. 6.3, in which the CP-mixed distribution lost the sinusoidal shape. However, the distribution of $|\Delta\phi_{j_1 j_2}|$ can

still be useful when compared to purely CP-even and CP-odd anomalous couplings.

Since Eq. 6.7 takes the absolute value of the difference between ϕ_{j_1} and ϕ_{j_2}, it lost information contained in the sign of the azimuthal angle between the tagging jets. It may initially appear challenging to define this sign unambiguously in pp collisions because the azimuthal angle changes sign when viewed from the opposite beam direction. However, one must consider the correlation of the tagging jets with the two distinct beam directions. When defining $\Delta\phi_{j_f j_b}$ as the azimuthal angle of the "away" jet minus the azimuthal angle of the "toward" jet, exchanging the two beam directions preserves the sign of $\Delta\phi_{j_f j_b}$ [23].

$\Delta\phi_{j_f j_b}$ is define as

$$\Delta\phi_{j_f j_b} = \begin{cases} \phi_{j_1} - \phi_{j_2}, & y_{j_1} > y_{j_2} \\ \phi_{j_2} - \phi_{j_1}, & y_{j_1} < y_{j_2} \end{cases} \tag{6.8}$$

In order to make $\Delta\phi_{j_f j_b} \in [-\pi, \pi]$, $\Delta\phi_{j_f j_b}$ also satisfies

$$\Delta\phi_{j_f j_b} = \begin{cases} \Delta\phi_{j_f j_b} + 2\pi, & \Delta\phi_{j_f j_b} < -\pi \\ \Delta\phi_{j_f j_b} - 2\pi, & \Delta\phi_{j_f j_b} > \pi \end{cases} \tag{6.9}$$

For the normalized four-momenta of the proton beams such as b_+ and b_-, while p_+ and p_- represent the four-momenta of the tagging jets. p_+ points into the same detector hemisphere as b_+ and p_- points the opposite detector hemisphere. Then

$$\begin{aligned} \epsilon_{\mu\nu\rho\sigma} b_+^\mu p_+^\nu b_-^\rho p_-^\sigma &= 2 p_{T,+} p_{T,-} \sin(\phi_+ - \phi_-) \\ &= 2 p_{T,+} p_{T,-} \sin \Delta\phi_{j_f j_b} \end{aligned} \tag{6.10}$$

provides the sign of $\Delta\phi_{j_f j_b}$ and it is a parity-odd observable. The definition in Eq. 6.10 is invariant under the interchange $(b_+, p_+) \to (b_-, p_-)$.

The distribution of $\Delta\phi_{j_f j_b}$ with TIGHT selection cuts are shown in the bottom row

of Fig. 6.1 for $h(2^\star) \bigoplus \mathrm{PS}$, Fig. 6.2 for $h(2^\star, 3)$, and Fig. 6.3 for $h(2^\star, 3^\star, 4)$ with three scenarios of purely anomalous couplings and the SM case. In the case of mixed CP-even and CP-odd couplings, the positions of the maxima shift to $\frac{\pi}{4}$ and the minima at $\frac{3\pi}{4}$. The observed shift in the $\Delta\phi_{j_f j_b}$ distribution further indicates the loss of information in the mixed CP case. Specifically, when folding the $\Delta\phi_{j_f j_b}$ distribution at $\Delta\phi_{j_f j_b} = 0$, the positions of the dips do not align, resulting in the characteristic curve as shown in Fig. 6.1. Both the $h(2^\star, 3)$ and $h(2^\star, 3^\star, 4)$ share similar features as $h(2^\star) \bigoplus \mathrm{PS}$, when including the sign information of $\Delta\phi_{j_f j_b}$, the CP-mixed case shift positions of dips.

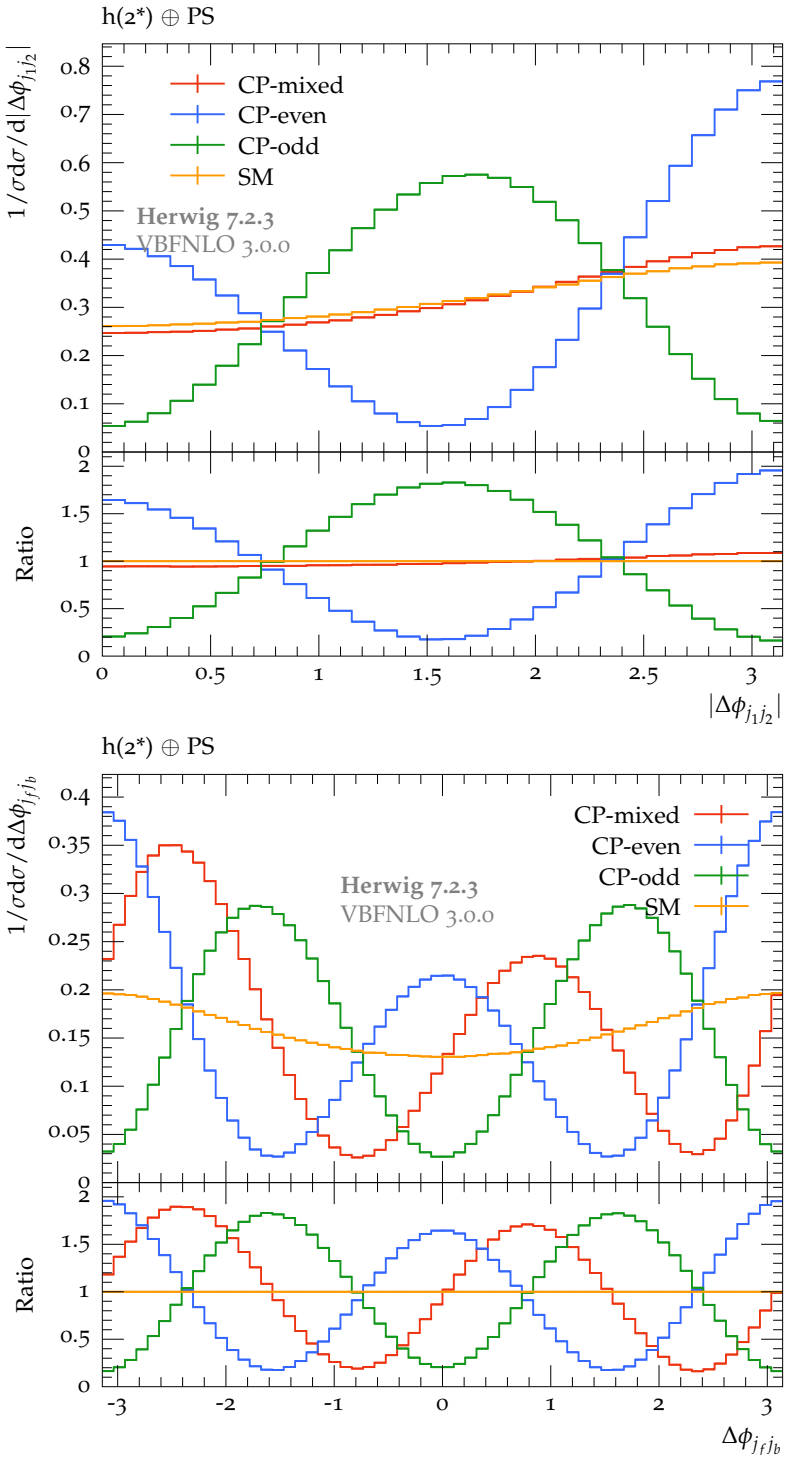

Figure 6.1: The distribution for of $|\Delta\phi_{j_1 j_2}|$ (top) and $\Delta\phi_{j_f j_b}$ (bottom) for matched setup $h(2^\star) \bigoplus$ PS using TIGHT selection cuts.

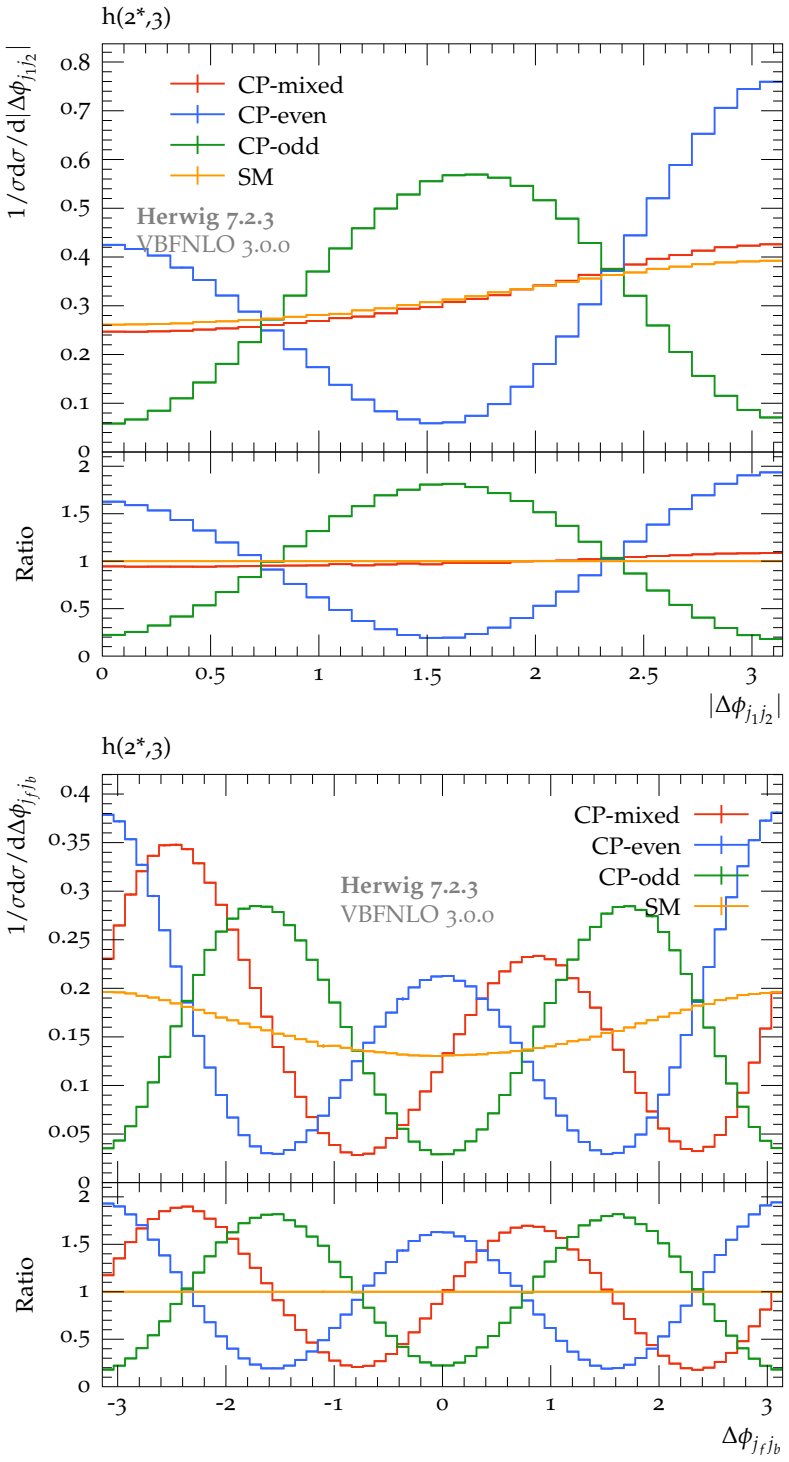

Figure 6.2: The distribution for of $|\Delta\phi_{j_1 j_2}|$ (top) and $\Delta\phi_{j_f j_b}$ (bottom) for merged setup $h(2^\star, 3)$ using TIGHT selection cuts.

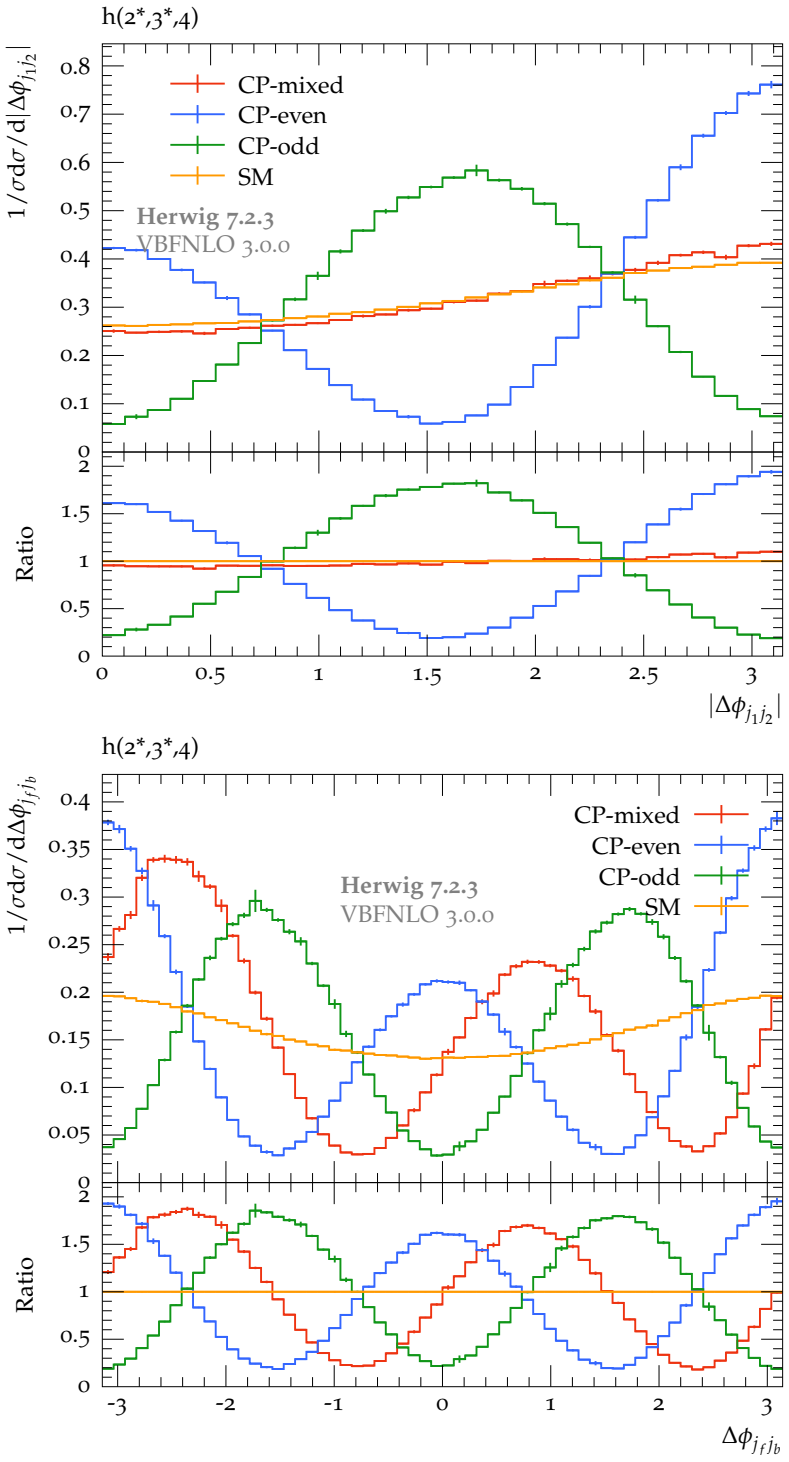

Figure 6.3: The distribution for of $|\Delta\phi_{j_1j_2}|$ (top) and $\Delta\phi_{j_fj_b}$ (bottom) for merged setup $h(2^\star, 3^\star, 4)$ using TIGHT selection cuts.

While in Fig. 6.1-6.3, I have shown that the CP structure of the Higgs boson vertex can be discerned by investigating the azimuthal angle between the two jets, the CP structure can also be studied through a modified azimuthal angle ϕ_2 [96] between q_a and q_b. Define ϕ_2 as

$$\phi_2 = \angle(\mathbf{q}_{a\perp}, \mathbf{q}_{b\perp}), \tag{6.11}$$

where

$$q_a = \sum_{j\in\{\text{jets:}y_j<y_h\}} p_j, \quad q_b = \sum_{j\in\{\text{jets:}y_j>y_h\}} p_j, \tag{6.12}$$

Here divide the observable jets into two groups by rapidity of Higgs boson, making the jets separated from the Higgs boson direction. $\mathbf{q}_{a\perp}$ and $\mathbf{q}_{b\perp}$ are the transverse component of the $\mathbf{q}_a$ and $\mathbf{q}_b$. Since there is rapidity and invariant mass cuts in the TIGHT selection cuts, the observable ϕ_2 should show a similar distribution as $\Delta\phi_{j_f j_b}$.

The distribution of the ϕ_2 is shown in Fig. 6.4-6.6 for $h(2^\star) \bigoplus \text{PS}$,$h(2^\star, 3)$, and $h(2^\star, 3^\star, 4)$ with TIGHT selection cuts. It can be seen that the ϕ_2 results share a number of key features compared to the distribution of $\Delta\phi_{j_f j_b}$. The three anomalous coupling scenarios are distinguishable by the shape of the observable ϕ_2 distribution. Again, even have the same strength as the CP-even and CP-odd couplings, the CP-mixed case still presents a characteristic curve with a shift of $\frac{\pi}{4}$ compared to the CP-even or CP-odd case.

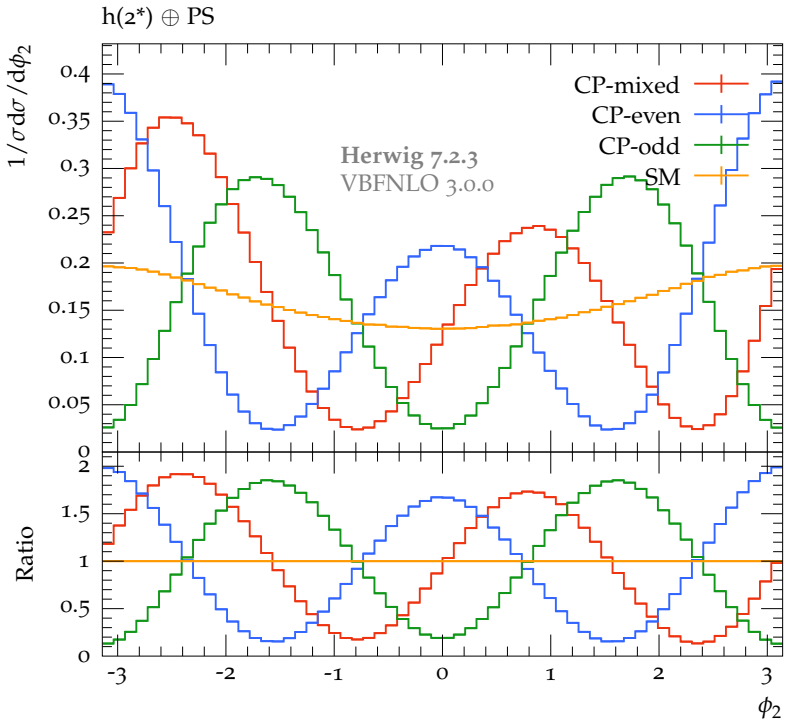

Figure 6.4: Distributions of ϕ_2 for $h(2^\star) \bigoplus \mathrm{PS}$ using TIGHT cuts.

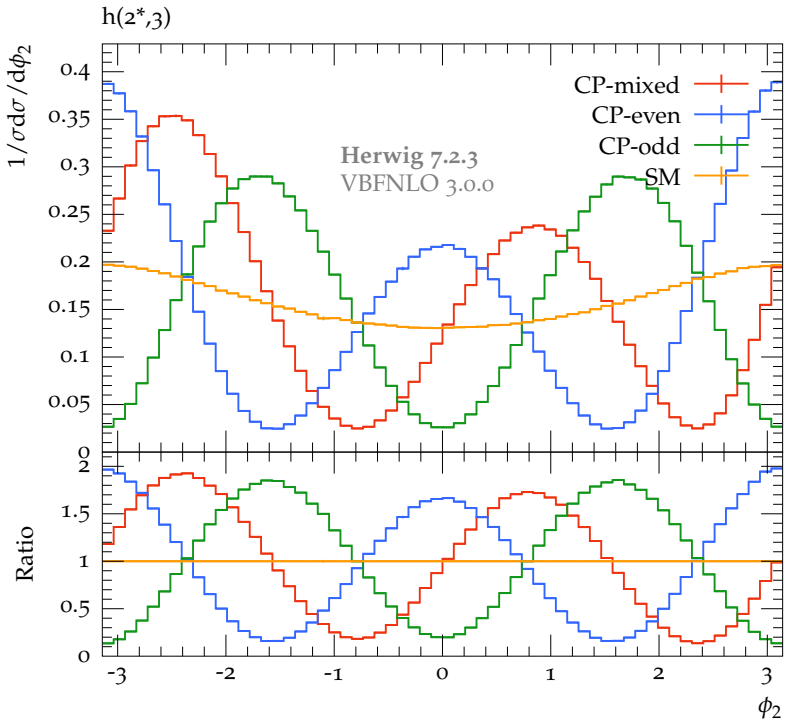

Figure 6.5: Distributions of ϕ_2 for $h(2^\star, 3)$ using TIGHT cuts.

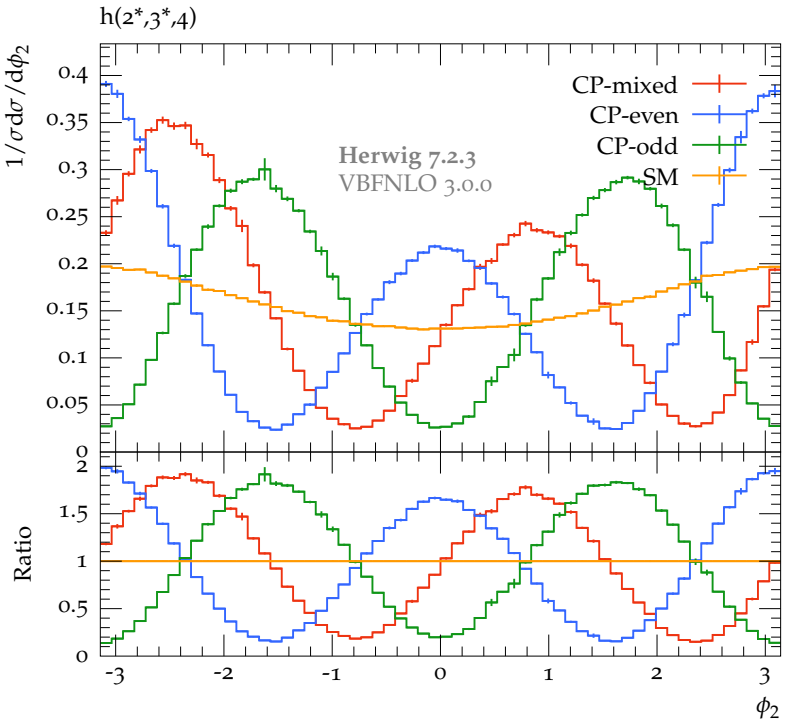

Figure 6.6: Distributions of ϕ_2 for merged setup $h(2^\star, 3^\star, 4)$ using TIGHT selection cuts.

6.5 Comparison Between Matching and Merging Results

As pointed out at the beginning of this chapter, both merging and matching frameworks in HERWIG 7 were used in the calculation of Higgs production with anomalous couplings. The difference between the merged setup and matched setup is shown in the following figures, where the merged setups are $h(2^\star, 3^\star, 4)$ and $h(2^\star, 3)$, the matched setup $h(2^\star) \bigoplus \text{PS}$, and the fixed NLO $h(2^\star)$ calculation. Let's start with the invariant mass distribution of the two leading jets in Fig. 6.7 for the four merged and matched setups, where the INCL and LOOSE selection cuts are applied. The $m_{j_1 j_2}$ distribution of $h(2^\star) \bigoplus \text{PS}$ and $h(2^\star)$ are deviated 10% and 15% from $h(2^\star, 3^\star, 4)$ at the beginning of the Fig. 6.7 with INCL cuts. When $m_{j_1 j_2} > 300$ GeV, the merged setup and the matched setup have agreement. After applying the LOOSE cut, as shown at the bottom of Fig. 6.7, merged and matched setups only have the differences due to the Monte Carlo error when $m_{j_1 j_2} > 300$ GeV. Fig. 6.8 presents the distribution of $\Delta y_{j_1 j_2}$ with INCL and TIGHT selection cuts. The ratio plot uses $h(2^\star, 3^\star, 4)$ as the reference. It can be seen that $h(2^\star)$

and $h(2^\star) \bigoplus \text{PS}$ are deviated 10% at the $\Delta y_{j_1 j_2} \in [0, 1]$. The $h(2^\star, 3)$ deviates 2% from the $h(2^\star, 3^\star, 4)$ setups in the same region. After applying the TIGHT cuts, the fixed order calculation $h(2^\star)$ deviates at the tail of the $\Delta y_{j_1 j_2}$ due to the Monte Carlo error. All other setups have an agreement.

In Fig. 6.9, I have shown the distribution of $|\Delta\phi_{j_1 j_2}|$ and the signed version azimuthal angle difference between the tagging jets, $\Delta\phi_{j_f j_b}$ for CP-mixed case. It can be observed that the fixed order calculation and matched setup agree with the merged setup $h(2^\star, 3^\star, 4)$ for distribution of $|\Delta\phi_{j_1 j_2}|$. However, for the distribution of $\Delta\phi_{j_f j_b}$, $h(2^\star) \bigoplus \text{PS}$ and $h(2^\star)$ shows 15% difference at $-\frac{\pi}{4}$ and $\frac{3\pi}{4}$. For CP-even couplings, $h(2^\star) \bigoplus \text{PS}$ deviates 20% at the dip of the distribution for $|\Delta\phi_{j_1 j_2}|$ in Fig. 6.10 and fixed order calculation $h(2^\star)$ shows 20% difference at the $\pi/2$. At the bottom plot of Fig. 6.10, $h(2^\star) \bigoplus \text{PS}$ deviate at $-\pi/2$ and $\pi/2$ for the quantity of 20% from the $h(2^\star, 3^\star, 4)$. The distribution of $|\Delta\phi_{j_1 j_2}|$ and $\Delta\phi_{j_f j_b}$ with CP-odd coupling is shown in Fig. 6.11. After applying the TIGHT selection cuts, the matched setup $h(2^\star) \bigoplus \text{PS}$ is smaller than the merged setup $h(2^\star, 3^\star, 4)$ for 15% at $|\Delta\phi_{j_1 j_2}| = 0$ and $|\Delta\phi_{j_1 j_2}| = 0$. Also, the $h(2^\star) \bigoplus \text{PS}$ deviates from $h(2^\star, 3^\star, 4)$ setups at $\Delta\phi_{j_f j_b} = -\pi$, $\Delta\phi_{j_f j_b} = 0$, and $\Delta\phi_{j_1 j_2} = \pi$ for 15% in the bottom plot of Fig. 6.11. Fig. 6.12 and Fig. 6.13 present the distribution of ϕ_2 for the CP-mixed, CP-even, and CP-odd anomalous couplings. Again, matched setup $h(2^\star) \bigoplus \text{PS}$ and fixed order calculation differ at the dips of the distribution as excepted and also observed in the distribution of $\Delta\phi_{j_f j_b}$.

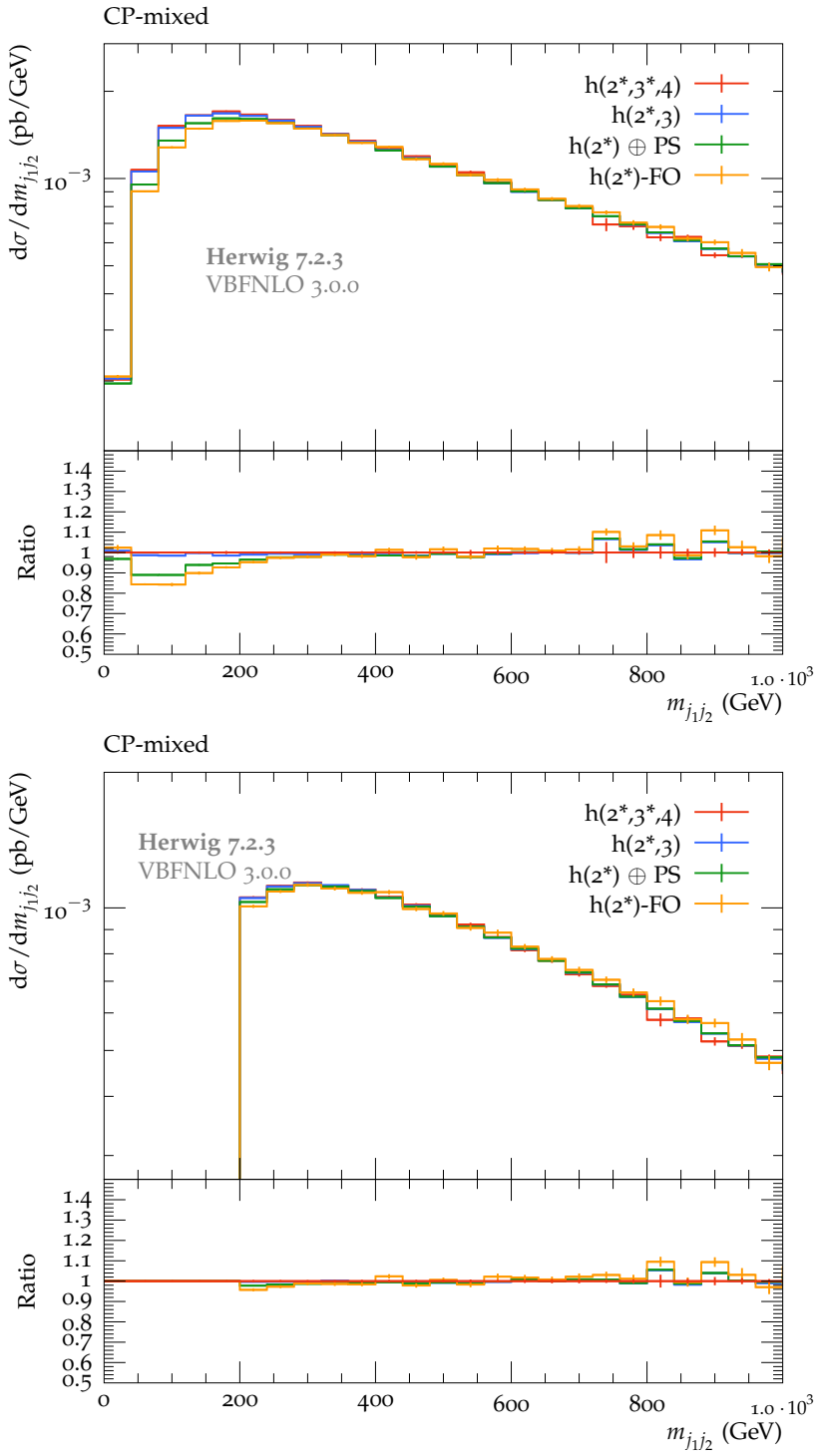

Figure 6.7: The distribution of $m_{j_1 j_2}$ with INCL cuts (top) and LOOSE cuts (bottom) for CP-mixed anomalous couplings. The ratio plot compared $h(2^\star, 3^\star, 4)$, $h(2^\star, 3)$, $h(2^\star) \bigoplus \mathrm{PS}$, and $h(2^\star)$ fixed order for NLO calculation, with the merged setup $h(2^\star, 3^\star, 4)$ as the reference.

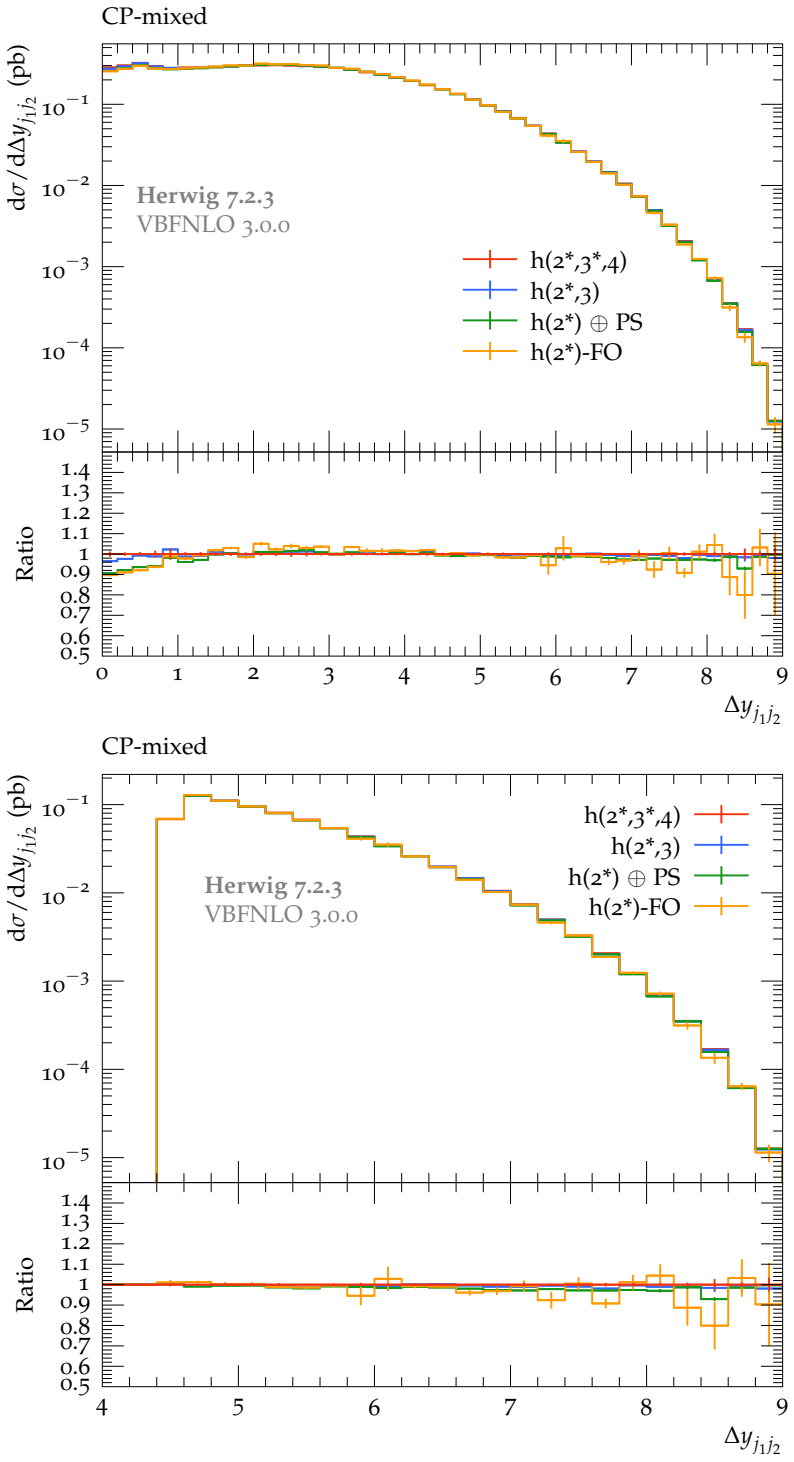

Figure 6.8: The distribution of $\Delta y_{j_1 j_2}$ with INCL cuts (top) and TIGHT cuts (bottom) for CP-mixed anomalous couplings. The ratio plot compared $h(2^\star, 3^\star, 4)$, $h(2^\star, 3)$, $h(2^\star) \bigoplus \mathrm{PS}$, and $h(2^\star)$ fixed order for NLO calculation, with the merged setup $h(2^\star, 3^\star, 4)$ as the reference.

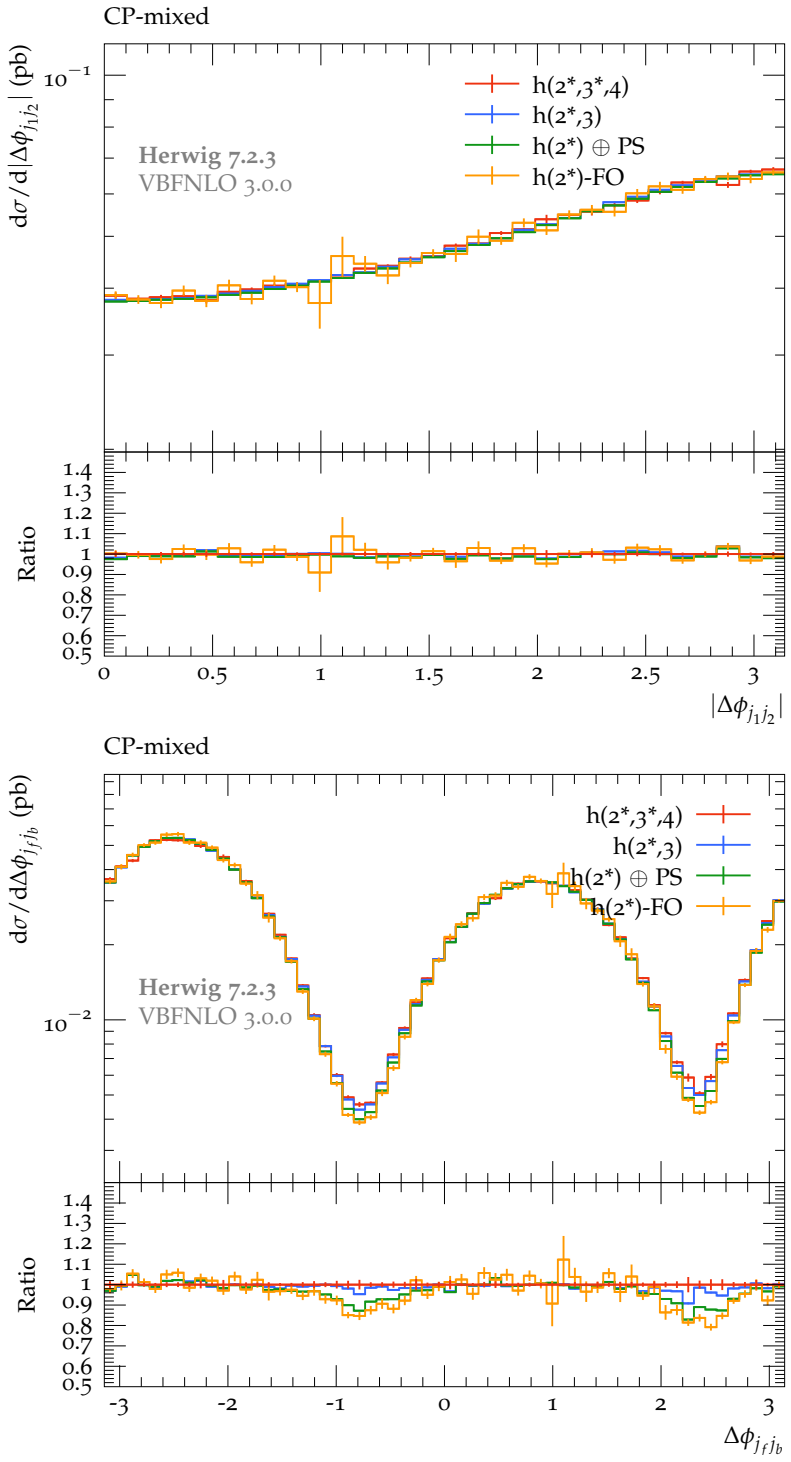

Figure 6.9: The distribution of $|\Delta\phi_{j_1 j_2}|$ (top) and $\Delta\phi_{j_f j_b}$ (bottom) for CP-mixed anomalous couplings with TIGHT cuts.

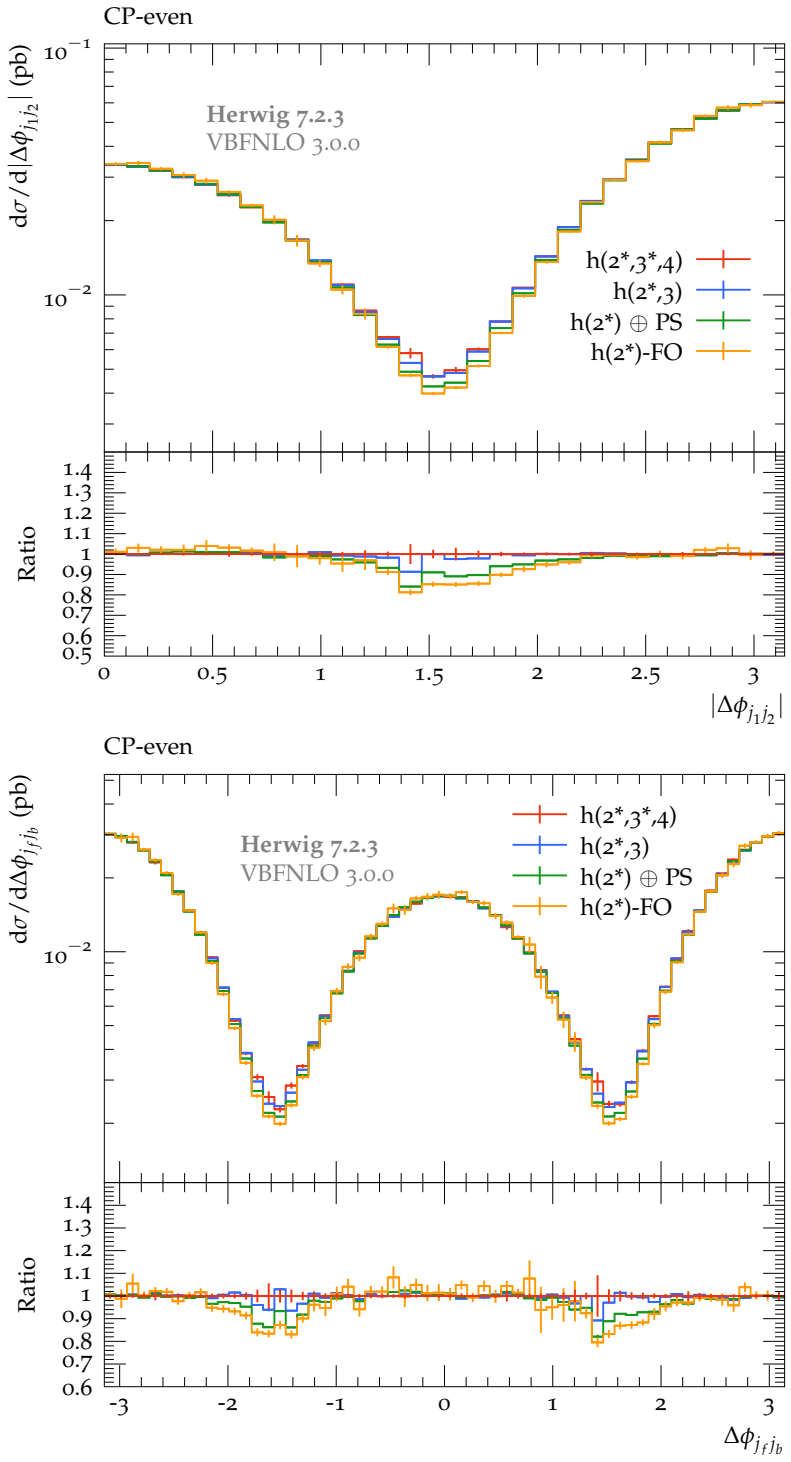

Figure 6.10: The distribution of $|\Delta\phi_{j_1 j_2}|$ (top) and $\Delta\phi_{j_f j_b}$ (bottom) for CP-even anomalous couplings with TIGHT cuts.

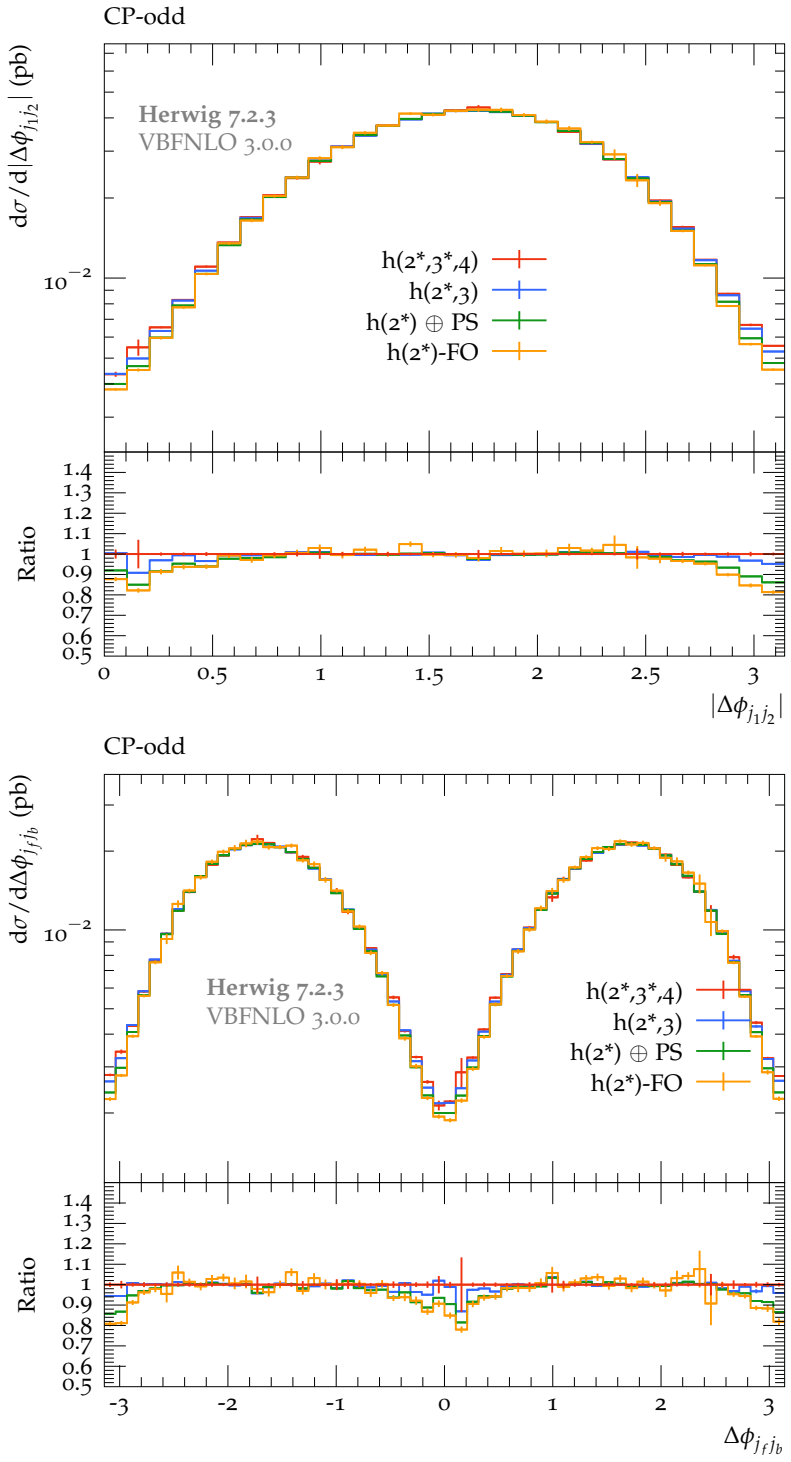

Figure 6.11: The distribution of $|\Delta\phi_{j_1 j_2}|$ (top) and $\Delta\phi_{j_f j_b}$ (bottom) for CP-odd anomalous couplings with TIGHT cuts.

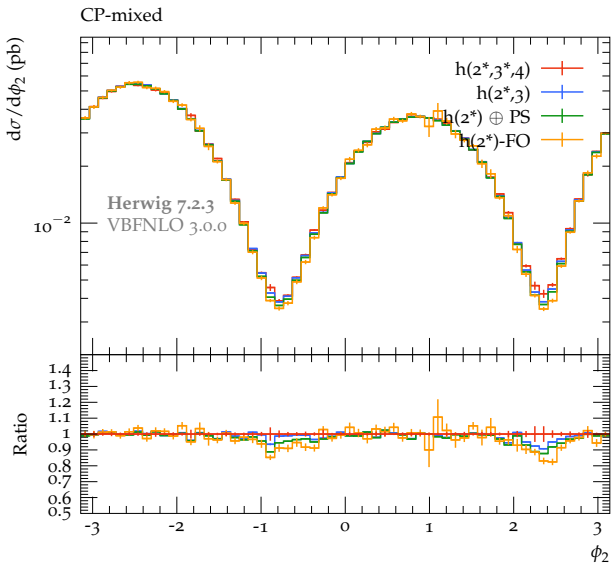

Figure 6.12: The distribution of ϕ_2 for CP-mixed anomalous couplings with TIGHT cuts.

6.6 Comparison Between Anomalous Couplings and SM

This section collects key results for the comparison between the three scenarios of anomalous couplings: CP-even, CP-odd, and CP-mixed, to SM prediction. The kinematic observables shown in the plots are the rapidity gap between two leading jets, the hardest jet rapidity distribution, and the distribution of the transverse momentum for the first leading jet. Let's first consider the distribution of the $\Delta y_{j_1 j_2}$ for $h(2^\star) \bigoplus \mathrm{PS}$. In Fig. 6.14, all cases with anomalous couplings show different behavior compared to the SM case. For the distribution of the rapidity gap (see Fig. 6.14 and Fig. 6.15), the CP structure shows a different pattern as compared to the SM distribution. At the bottom plot of Fig. 6.14, the rapidity distribution of the first leading jet displays the fact that in the case of anomalous couplings, the jets are more central than in the SM case. The same glaring difference appears in the $h(2^\star, 3^\star, 4)$ setups as shown in Fig.6.15, which offer a tool to discriminate about different parity assignments. Fig. 6.16 shows the normalized transverse momentum distribution of the first leading jet p_{T,j_1}, it can be seen that three CP scenarios start to deviate from SM at $p_{T,j_1} = 20$ GeV. The plots have also shown that the distribution of transverse momentum can not sufficiently distinguish between different CP structures.

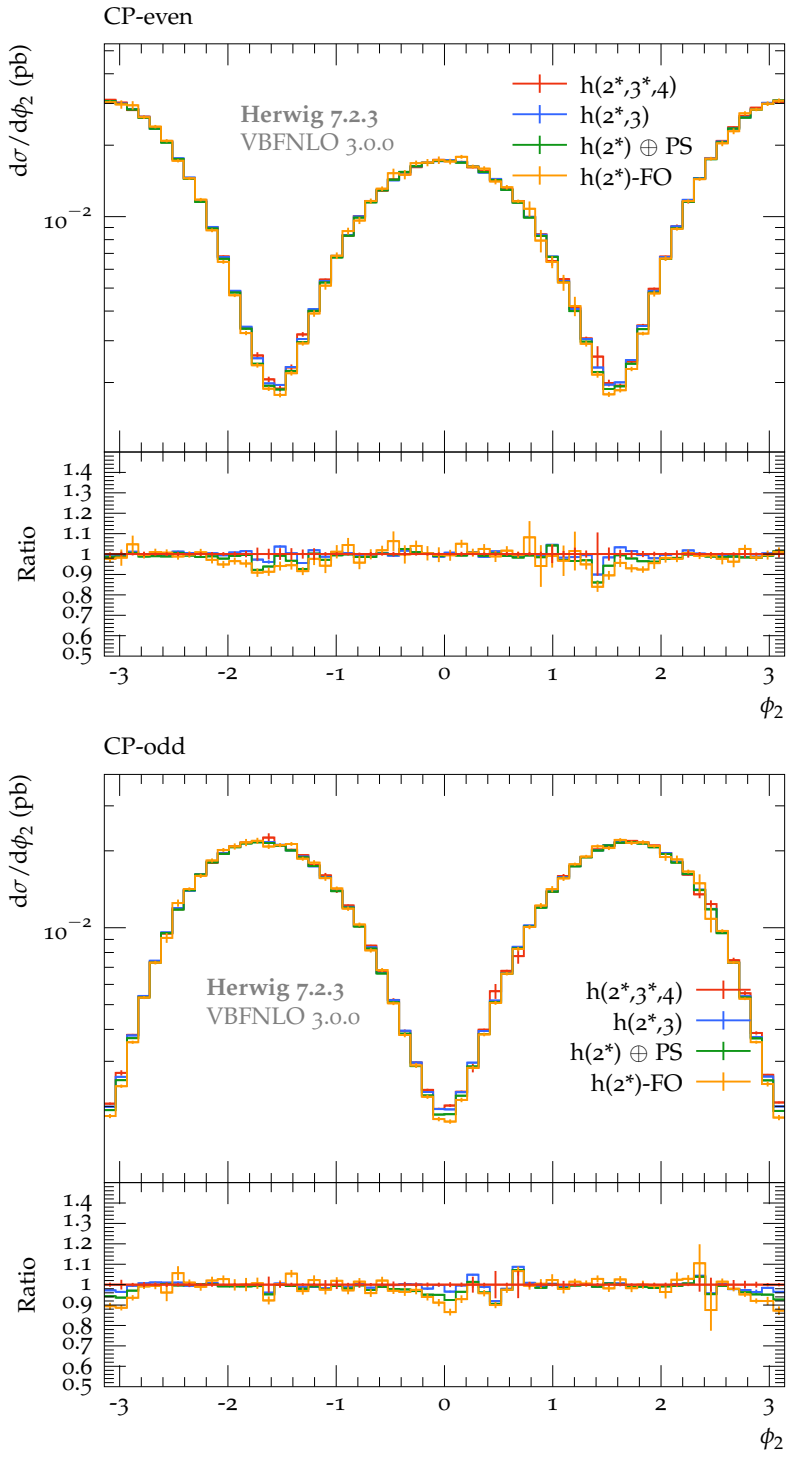

Figure 6.13: The distribution of ϕ_2 for CP-even (top) and CP-odd (bottom) anomalous couplings with TIGHT cuts.

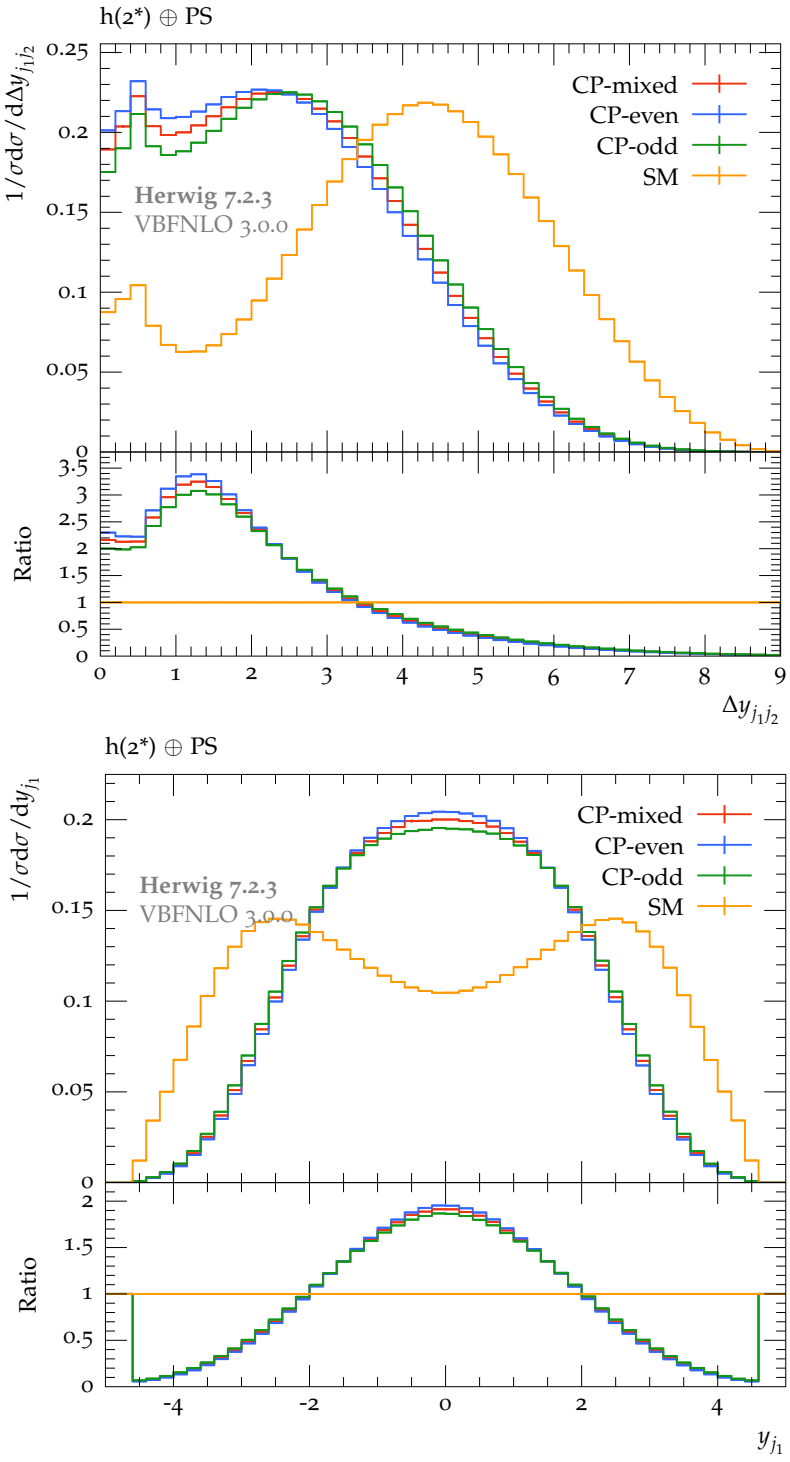

Figure 6.14: The distribution of $\Delta y_{j_1 j_2}$ (top) and y_{j_1} (bottom) for $h(2^\star) \oplus$ PS with INCL cuts.

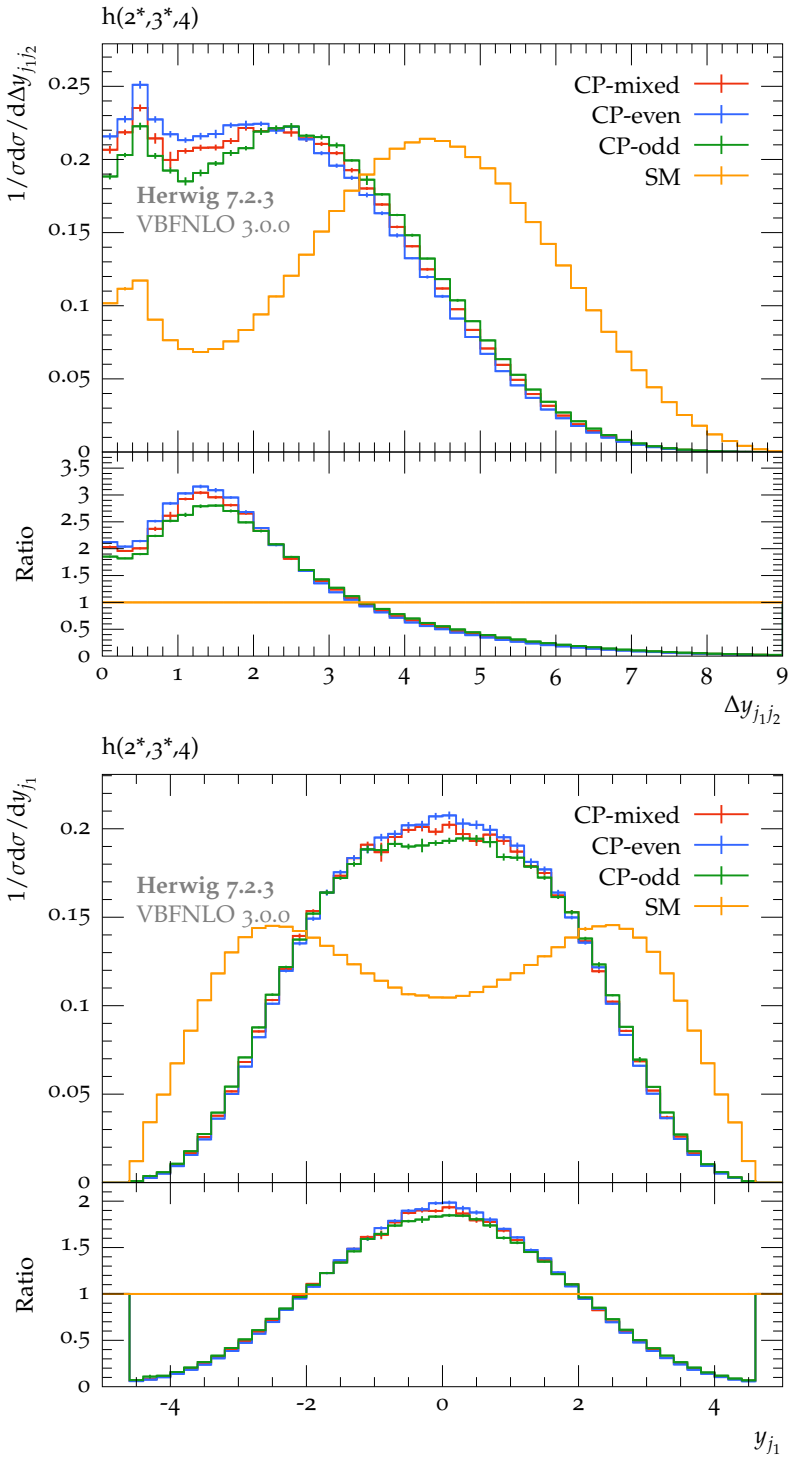

Figure 6.15: The distribution of $\Delta y_{j_1 j_2}$ (top) and y_{j_1} (bottom) for $h(2^\star, 3^\star, 4)$ with INCL cuts.

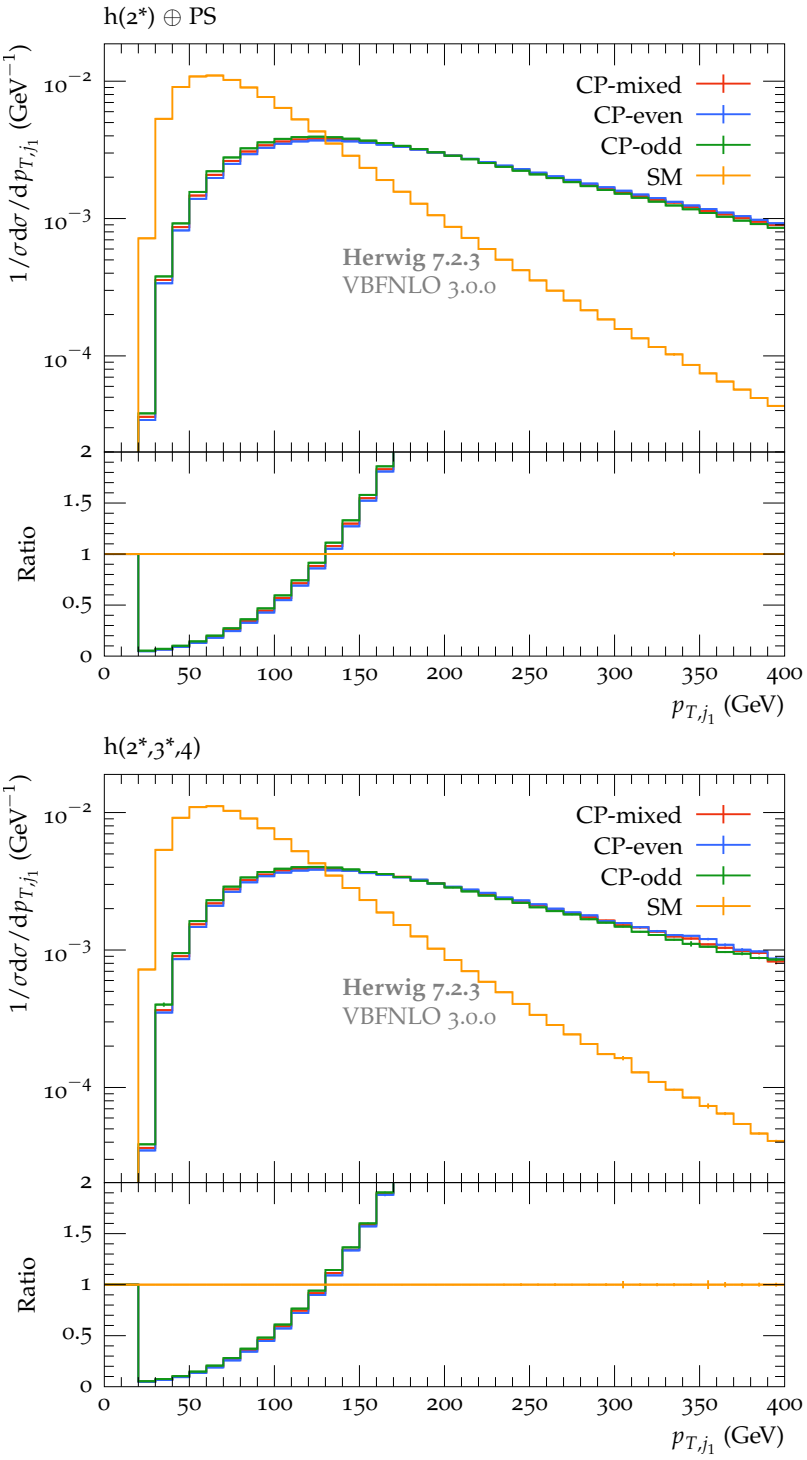

Figure 6.16: The distribution of P_{T,j_1} for $h(2^\star) \bigoplus \text{PS}$ (top) and $h(2^\star, 3^\star, 4)$ (bottom) with INCL cuts.

CHAPTER 6
CONCLUSIONS AND OUTLOOK

Although the anomalous Higgs couplings via VBF has already available in `VBFNLO`, in order to present results using the matching and merging framework provided by Herwig 7, I have implemented the anomalous coupling for Higgs plus three jets production. The programs are written in `Fortran` and implemented into the `VBFNLO` in a numerically stable way. I have applied a dedicated system of checks and balances to verify this implementation. Checks include verification against available automated matrix elements implemented in `VBFNLO` for LO, dipole subtraction check for real emission, and gauge test for virtual correction relying on the Ward identity. I have reviewed the Standard Model and the calculation for the NLO cross section in Chapter 2. In addition, I also briefly introduced the Catani-Seymour subtraction method which is used in the NLO calculation for Higgs plus three jets production. In Chapter 3, matched and merged setups for Higs boson plus two jets are discussed and the results on the numerical calculations are presented using `HJets` and `VBFNLO` via Herwig 7.

The detailed implementation of the design of numerical building blocks for LO, real emission, and virtual correction are discussed in Chapter 4. I also introduced the helicity amplitude method and demonstrated the calculation of $Hjjj@LO$. In order to program the generalized tensor structure and combine it into the existing Higgs boson plus three jets subroutines, I have created several subroutines to calculate the CP-even or CP-odd structure for all parts of the NLO cross section.

All parts of the code have been carefully checked. In particular, LO cross sections and distributions have been compared with the already checked results and take advantage of the feature in `VBFNLO` that adds additional LO jets. Furthermore, Ward identity tests for the virtual contributions have been implemented and the cancellation of divergences in the real emission against the counter-terms, as given by the subtraction method has been checked.

The phenomenology results are presented in Chapter 6. The Monte Carlo event generator HERWIG 7 is used to generate the events for fixed order calculation $h(2^\star)$, matched setup $h(2^\star) \bigoplus \text{PS}$, merged setup $h(2^\star, 3)$, and $h(2^\star, 3^\star, 4)$. The generated events are analyzed by `Rivet` to create the `yoda` file and make plots. Several observables can be studied to extract the CP structure of the HVV vertex, and I have shown the distribution of these observables in different CP scenarios. I have compared the predictions for Higgs plus two jets in matched and merged framework via HERWIG 7 and find that for all anomalous coupling cases, for two jet observables $\Delta y_{j_1 j_2}$ and $m_{j_1 j_2}$ there is a deviation up to 10% between matched setup and merged setup when only applied INCL cuts. While after applying the TIGHT cuts, the merged setups $h(2^\star, 3^\star, 4)$ and matched setups $h(2^\star) \bigoplus \text{PS}$ are in good agreement. For CP-sensitive observables, the deviation between matched setup and the merged setup occurs in the dips of the distribution. The fixed order calculation $h(2^\star)$ deviates up to 20% compared with the merged setup in all three CP scenarios.

The source code I developed in this dissertation will become online at GitHub [2] and is suitable for merging into `VBFNLO`. It provides a computational tool for both experimentalists and theorists to investigate possible CP violation searches via VBF Higgs boson production. The tools and techniques I presented are for the study of Higgs boson couples to W or Z bosons. The Higgs boson anomalous coupling that has not been studied in this dissertation is the Higgs boson couples to γ and/or Z boson. Another development one can make anomalous Higgs boson coupling implementation to the full calculation of Higgs boson production provided by `HJets` [55–58].

[2] https://github.com/tinghuagithub/Anomalous-Higgs-Boson-Couplings

REFERENCES

REFERENCES

[1] BeoShock, "The computing for this project was performed on the BeoShock Research Cluster at WSU, which is funded by Academic Affairs, Liberal Arts Sciences, College of Engineering, Barton School of Business, and the Office of Research.," *https://www.wichita.edu/services/hpc/hpc-user-policy.php*.

[2] Beocat, "The computing for this project was performed on the Beocat Research Cluster at Kansas State University, which is funded in part by NSF grants CNS-1006860, EPS-1006860, EPS-0919443, ACI-1440548, CHE-1726332, and NIH P20GM113109.," *https://support.beocat.ksu.edu/Docs/Policy*.

[3] "A detailed map of Higgs boson interactions by the ATLAS experiment ten years after the discovery," *Nature*, vol. 607, no. 7917, pp. 52–59, 2022. [Erratum: Nature 612, E24 (2022)].

[4] R. L. Workman *et al.*, "Review of Particle Physics," *PTEP*, vol. 2022, p. 083C01, 2022.

[5] T. M. Figy, "NLO QCD corrections to the jet activity in Higgs boson production via vector-boson fusion," other thesis, 2006.

[6] S. Weinberg, "A model of leptons," *Phys. Rev. Lett.*, vol. 19, pp. 1264–1266, Nov 1967.

[7] A. Salam, "Weak and Electromagnetic Interactions," *Conf. Proc. C*, vol. 680519, pp. 367–377, 1968.

[8] S. L. Glashow, "Partial Symmetries of Weak Interactions," *Nucl. Phys.*, vol. 22, pp. 579–588, 1961.

[9] "The Standard Model," *https://cds.cern.ch/record/1997201*, 2012.

[10] P. W. Higgs, "Broken Symmetries and the Masses of Gauge Bosons," *Phys. Rev. Lett.*, vol. 13, pp. 508–509, 1964.

[11] F. Englert and R. Brout, "Broken symmetry and the mass of gauge vector mesons," *Phys. Rev. Lett.*, vol. 13, pp. 321–323, Aug 1964.

[12] G. Aad *et al.*, "Observation of a new particle in the search for the Standard Model Higgs boson with the ATLAS detector at the LHC," *Phys. Lett. B*, vol. 716, pp. 1–29, 2012.

[13] S. Chatrchyan *et al.*, "Observation of a New Boson at a Mass of 125 GeV with the CMS Experiment at the LHC," *Phys. Lett. B*, vol. 716, pp. 30–61, 2012.

[14] G. Aad *et al.*, "Evidence for the spin-0 nature of the Higgs boson using ATLAS data," *Phys. Lett. B*, vol. 726, pp. 120–144, 2013.

[15] A. Collaboration, "Test of cp-invariance of the higgs boson in vector-boson fusion production and its decay into four leptons," 2023.

[16] G. Gamow, "Expanding universe and the origin of elements," *Phys. Rev.*, vol. 70, pp. 572–573, 1946.

[17] R. Aaij *et al.*, "Amplitude analysis of $B^{\pm} \to \pi^{\pm}K^{+}K^{-}$ decays," *Phys. Rev. Lett.*, vol. 123, no. 23, p. 231802, 2019.

[18] J. H. Christenson, J. W. Cronin, V. L. Fitch, and R. Turlay, "Evidence for the 2π Decay of the K_2^0 Meson," *Phys. Rev. Lett.*, vol. 13, pp. 138–140, 1964.

[19] J. Baglio, J. Bellm, G. Bozzi, M. Brieg, F. Campanario, C. Englert, B. Feigl, J. Frank, T. Figy, F. Geyer, *et al.*, "Vbfnlo: A parton level monte carlo for processes with electroweak bosons–manual for version 2.7. 0," *arXiv preprint arXiv:1107.4038*, 2011.

[20] J. Baglio, J. Bellm, F. Campanario, B. Feigl, J. Frank, T. Figy, M. Kerner, L. Ninh, S. Palmer, M. Rauch, *et al.*, "Release note-vbfnlo 2.7. 0," *arXiv preprint arXiv:1404.3940*, 2014.

[21] K. Arnold *et al.*, "VBFNLO: A Parton level Monte Carlo for processes with electroweak bosons," *Comput. Phys. Commun.*, vol. 180, pp. 1661–1670, 2009.

[22] T. Figy, V. Hankele, and D. Zeppenfeld, "Next-to-leading order QCD corrections to Higgs plus three jet production in vector-boson fusion," *JHEP*, vol. 02, p. 076, 2008.

[23] V. Hankele, G. Klamke, D. Zeppenfeld, and T. Figy, "Anomalous Higgs boson couplings in vector boson fusion at the CERN LHC," *Phys. Rev. D*, vol. 74, p. 095001, 2006.

[24] F. Maltoni, K. Mawatari, and M. Zaro, "Higgs characterisation via vector-boson fusion and associated production: NLO and parton-shower effects," *Eur. Phys. J. C*, vol. 74, no. 1, p. 2710, 2014.

[25] P. Artoisenet *et al.*, "A framework for Higgs characterisation," *JHEP*, vol. 11, p. 043, 2013.

[26] N. D. Christensen and C. Duhr, "FeynRules - Feynman rules made easy," *Comput. Phys. Commun.*, vol. 180, pp. 1614–1641, 2009.

[27] J. Alwall, M. Herquet, F. Maltoni, O. Mattelaer, and T. Stelzer, "MadGraph 5 : Going Beyond," *JHEP*, vol. 06, p. 128, 2011.

[28] M. Bahr *et al.*, "Herwig++ Physics and Manual," *Eur. Phys. J. C*, vol. 58, pp. 639–707, 2008.

[29] J. Bellm *et al.*, "Herwig 7.0/Herwig++ 3.0 release note," *Eur. Phys. J. C*, vol. 76, no. 4, p. 196, 2016.

[30] S. Platzer and S. Gieseke, "Dipole Showers and Automated NLO Matching in Herwig++," *Eur. Phys. J. C*, vol. 72, p. 2187, 2012.

[31] J. Bellm *et al.*, "Herwig 7.2 release note," *Eur. Phys. J. C*, vol. 80, no. 5, p. 452, 2020.

[32] S. Alioli *et al.*, "Update of the Binoth Les Houches Accord for a standard interface between Monte Carlo tools and one-loop programs," *Comput. Phys. Commun.*, vol. 185, pp. 560–571, 2014.

[33] T. Binoth *et al.*, "A Proposal for a Standard Interface between Monte Carlo Tools and One-Loop Programs," *Comput. Phys. Commun.*, vol. 181, pp. 1612–1622, 2010.

[34] S. Catani and M. H. Seymour, "A general algorithm for calculating jet cross sections in nlo qcd," *Nuclear Physics B*, vol. 485, no. 1-2, pp. 291–419, 1997.

[35] T. Chen, T. M. Figy, and S. Plätzer, "NLO multijet merging for Higgs production beyond the VBF approximation," *Eur. Phys. J. C*, vol. 82, no. 8, p. 704, 2022.

[36] J. Campbell, J. Huston, and F. Krauss, *The black book of quantum chromodynamics: a primer for the LHC era*. Oxford University Press, 2018.

[37] S. Weinberg, "A Model of Leptons," *Phys. Rev. Lett.*, vol. 19, pp. 1264–1266, 1967.

[38] C.-N. Yang and R. L. Mills, "Conservation of Isotopic Spin and Isotopic Gauge Invariance," *Phys. Rev.*, vol. 96, pp. 191–195, 1954.

[39] S. Dawson, "Introduction to Electroweak Symmetry Breaking," *AIP Conf. Proc.*, vol. 1116, no. 1, pp. 11–34, 2009.

[40] A. Djouadi, "The Anatomy of electro-weak symmetry breaking. I: The Higgs boson in the standard model," *Phys. Rept.*, vol. 457, pp. 1–216, 2008.

[41] W. Hollik, "Quantum field theory and the Standard Model," in *2009 European School of High-Energy Physics*, 12 2010.

[42] F. Halzen and A. D. Martin, *QUARKS AND LEPTONS: AN INTRODUCTORY COURSE IN MODERN PARTICLE PHYSICS*. 1984.

[43] M. L. Mangano, "Introduction to QCD," in *1998 European School of High-Energy Physics*, pp. 53–97, 1998.

[44] P. Skands, "Introduction to QCD," in *Theoretical Advanced Study Institute in Elementary Particle Physics: Searching for New Physics at Small and Large Scales*, pp. 341–420, 2013.

[45] D. J. Gross and F. Wilczek, "Ultraviolet Behavior of Nonabelian Gauge Theories," *Phys. Rev. Lett.*, vol. 30, pp. 1343–1346, 1973.

[46] H. D. Politzer, "Reliable Perturbative Results for Strong Interactions?," *Phys. Rev. Lett.*, vol. 30, pp. 1346–1349, 1973.

[47] R. Ellis, W. Stirling, and B. Webber, "Qcd and collider physics," 1996.

[48] S. Höche, "Introduction to parton-shower event generators," in *Journeys Through the Precision Frontier: Amplitudes for Colliders: TASI 2014 Proceedings of the 2014 Theoretical Advanced Study Institute in Elementary Particle Physics*, pp. 235–295, World Scientific, 2016.

[49] A. Buckley, J. Butterworth, S. Gieseke, D. Grellscheid, S. Höche, H. Hoeth, F. Krauss, L. Lönnblad, E. Nurse, P. Richardson, *et al.*, "General-purpose event generators for lhc physics," *Physics Reports*, vol. 504, no. 5, pp. 145–233, 2011.

[50] M. H. Seymour, "Jets in QCD," *AIP Conf. Proc.*, vol. 357, pp. 568–587, 1996.

[51] T. Figy, C. Oleari, and D. Zeppenfeld, "Next-to-leading order jet distributions for Higgs boson production via weak boson fusion," *Phys. Rev. D*, vol. 68, p. 073005, 2003.

[52] J. Bellm, G. Nail, S. Plätzer, P. Schichtel, and A. Siódmok, "Parton Shower Uncertainties with Herwig 7: Benchmarks at Leading Order," *Eur. Phys. J. C*, vol. 76, no. 12, p. 665, 2016.

[53] S. Platzer and S. Gieseke, "Coherent Parton Showers with Local Recoils," *JHEP*, vol. 01, p. 024, 2011.

[54] S. Gieseke, P. Stephens, and B. Webber, "New formalism for QCD parton showers," *JHEP*, vol. 12, p. 045, 2003.

[55] F. Campanario, T. M. Figy, S. Plätzer, and M. Sjödahl, "Electroweak Higgs Boson Plus Three Jet Production at Next-to-Leading-Order QCD," *Phys. Rev. Lett.*, vol. 111, no. 21, p. 211802, 2013.

[56] F. Campanario, T. M. Figy, S. Plätzer, and M. Sjödahl, "NLO QCD Corrections to Electroweak Higgs Boson Plus Three Jet Production at the LHC," *PoS*, vol. RADCOR2013, p. 042, 2013.

[57] F. Campanario, T. M. Figy, S. Plätzer, and M. Sjodahl, "Beyond the t-channel Approximation: Next-to-Leading Order QCD Corrections to Electroweak Higgs Boson Production Plus Three Jets Production at the LHC," *PoS*, vol. LL2014, p. 025, 2014.

[58] F. Campanario, T. M. Figy, S. Plätzer, M. Rauch, P. Schichtel, and M. Sjödahl, "Stress testing the vector-boson-fusion approximation in multijet final states," *Phys. Rev.*, vol. D98, no. 3, p. 033003, 2018.

[59] S. Frixione and B. R. Webber, "Matching NLO QCD computations and parton shower simulations," *JHEP*, vol. 06, p. 029, 2002.

[60] P. Nason, "A New method for combining NLO QCD with shower Monte Carlo algorithms," *JHEP*, vol. 11, p. 040, 2004.

[61] A. Buckley *et al.*, "A comparative study of Higgs boson production from vector-boson fusion," *JHEP*, vol. 11, p. 108, 2021.

[62] L. Lonnblad and S. Prestel, "Matching Tree-Level Matrix Elements with Interleaved Showers," *JHEP*, vol. 03, p. 019, 2012.

[63] L. Lönnblad and S. Prestel, "Merging Multi-leg NLO Matrix Elements with Parton Showers," *JHEP*, vol. 03, p. 166, 2013.

[64] L. Lonnblad and S. Prestel, "Unitarising Matrix Element + Parton Shower merging," *JHEP*, vol. 02, p. 094, 2013.

[65] J. Bellm, S. Gieseke, and S. Plätzer, "Merging NLO Multi-jet Calculations with Improved Unitarization," *Eur. Phys. J. C*, vol. 78, no. 3, p. 244, 2018.

[66] S. Catani, B. Webber, and G. Marchesini, "QCD coherent branching and semiinclusive processes at large x," *Nucl. Phys. B*, vol. 349, pp. 635–654, 1991.

[67] M. Sjodahl, "ColorFull – a C++ library for calculations in SU(Nc) color space," *Eur. Phys. J.*, vol. C75, no. 5, p. 236, 2015.

[68] F. Campanario, "Towards pp -> VVjj at NLO QCD: Bosonic contributions to triple vector boson production plus jet," *JHEP*, vol. 10, p. 070, 2011.

[69] S. Catani, Y. L. Dokshitzer, M. H. Seymour, and B. R. Webber, "Longitudinally invariant K_t clustering algorithms for hadron hadron collisions," *Nucl. Phys. B*, vol. 406, pp. 187–224, 1993.

[70] S. D. Ellis and D. E. Soper, "Successive combination jet algorithm for hadron collisions," *Phys. Rev. D*, vol. 48, pp. 3160–3166, 1993.

[71] T. Figy and D. Zeppenfeld, "QCD corrections to jet correlations in weak boson fusion," *Phys. Lett. B*, vol. 591, pp. 297–303, 2004.

[72] W. Buchmuller and D. Wyler, "Effective Lagrangian Analysis of New Interactions and Flavor Conservation," *Nucl. Phys. B*, vol. 268, pp. 621–653, 1986.

[73] K. Hagiwara, S. Ishihara, R. Szalapski, and D. Zeppenfeld, "Low-energy effects of new interactions in the electroweak boson sector," *Phys. Rev. D*, vol. 48, pp. 2182–2203, 1993.

[74] P. Achard *et al.*, "Search for anomalous couplings in the Higgs sector at LEP," *Phys. Lett. B*, vol. 589, pp. 89–102, 2004.

[75] M. C. Gonzalez-Garcia, "Anomalous Higgs couplings," *Int. J. Mod. Phys. A*, vol. 14, pp. 3121–3156, 1999.

[76] G. J. Gounaris, F. M. Renard, and N. D. Vlachos, "Tests of anomalous Higgs boson couplings through e- e+ —> H Z and H gamma," *Nucl. Phys. B*, vol. 459, pp. 51–74, 1996.

[77] B. Grzadkowski and J. Wudka, "Higgs boson production at e+ e- colliders: A model independent approach," *Phys. Lett. B*, vol. 364, pp. 49–54, 1995.

[78] K. Hagiwara, R. D. Peccei, D. Zeppenfeld, and K. Hikasa, "Probing the Weak Boson Sector in e+ e- —> W+ W-," *Nucl. Phys. B*, vol. 282, pp. 253–307, 1987.

[79] K. Hagiwara, R. Szalapski, and D. Zeppenfeld, "Anomalous Higgs boson production and decay," *Phys. Lett. B*, vol. 318, pp. 155–162, 1993.

[80] K. Hagiwara and D. Zeppenfeld, "Amplitudes for Multiparton Processes Involving a Current at e+ e-, e+- p, and Hadron Colliders," *Nucl. Phys. B*, vol. 313, pp. 560–594, 1989.

[81] J. Baglio *et al.*, "VBFNLO: A Parton Level Monte Carlo for Processes with Electroweak Bosons – Manual for Version 2.7.0," 7 2011.

[82] J. Baglio *et al.*, "Release Note - VBFNLO 2.7.0," 2014.

[83] A. Buckley, J. Ferrando, S. Lloyd, K. Nordström, B. Page, M. Rüfenacht, M. Schönherr, and G. Watt, "LHAPDF6: parton density access in the LHC precision era," *Eur. Phys. J. C*, vol. 75, p. 132, 2015.

[84] J. C. Ward, "An Identity in Quantum Electrodynamics," *Phys. Rev.*, vol. 78, p. 182, 1950.

[85] Y. Takahashi, "On the generalized ward identity," *Il Nuovo Cimento (1955-1965)*, vol. 6, no. 2, pp. 371–375, 1957.

[86] M. E. Peskin and D. V. Schroeder, *An Introduction to quantum field theory*. Reading, USA: Addison-Wesley, 1995.

[87] E. Daw, "Lecture 7-rapidity and pseudorapidity," 2012.

[88] J. Bellm, S. Gieseke, D. Grellscheid, S. Plätzer, M. Rauch, C. Reuschle, P. Richardson, P. Schichtel, M. H. Seymour, A. Siódmok, *et al.*, "Herwig 7.0/herwig++ 3.0 release note," *arXiv preprint arXiv:1512.01178*, 2015.

[89] S. Plätzer and S. Gieseke, "Dipole showers and automated nlo matching in herwig++," *The European Physical Journal C*, vol. 72, no. 11, p. 2187, 2012.

[90] D. Rauch, "Automated nlo calculations with massive quarks in herwig++," Master's thesis, Karlsruhe Institute of Technology, Dec. 2014.

[91] A. Buckley, J. Butterworth, D. Grellscheid, H. Hoeth, L. Lönnblad, J. Monk, H. Schulz, and F. Siegert, "Rivet user manual," *Computer Physics Communications*, vol. 184, no. 12, pp. 2803–2819, 2013.

[92] M. Cacciari and G. P. Salam, "Dispelling the N^3 myth for the k_t jet-finder," *Phys. Lett.*, vol. B641, pp. 57–61, 2006.

[93] J. Butterworth, S. Carrazza, A. Cooper-Sarkar, A. D. Roeck, J. Feltesse, S. Forte, J. Gao, S. Glazov, J. Huston, Z. Kassabov, and et al., "Pdf4lhc recommendations for lhc run ii," *Journal of Physics G: Nuclear and Particle Physics*, vol. 43, p. 023001, Jan 2016.

[94] M. Cacciari, G. P. Salam, and G. Soyez, "FastJet User Manual," *Eur. Phys. J.*, vol. C72, p. 1896, 2012.

[95] A. Buckley, J. Butterworth, D. Grellscheid, H. Hoeth, L. Lönnblad, J. Monk, H. Schulz, and F. Siegert, "Rivet user manual," *Computer Physics Communications*, vol. 184, p. 2803–2819, Dec 2013.

[96] J. R. Andersen, K. Arnold, and D. Zeppenfeld, "Azimuthal Angle Correlations for Higgs Boson plus Multi-Jet Events," *JHEP*, vol. 06, p. 091, 2010.

APPENDIX

APPENDIX

The Herwig 7 Usage Example

To use HERWIG 7 to generate the event for a specific process, first need to activate the HERWIG environment by

```
$ source /where/herwig/install/bin/activate
```

The HERWIG 7 needs to read the input files through the "build" step, and it can be parallelized by providing n integration jobs through

```
$ Hewrig build --maxjobs=n LHC-H-Merging.in
```

After this, a `.run` file will be created, but subprocess integration has been postponed to the next step, which can then be run via:

```
$ Hewrig integrate --jobid=k LHC-H-Merging.run
```

where $n \in [0, n-1]$. To integrate all n jobs using

```
$ for k in {0..n-1};\
do (./Herwig integrate --jobid=$k LHC-H-Merging.run &); done
```

Then parallel event generation can be performed by using a number of jobs with different random seeds,

```
$ Herwig run --seed=426738 LHC-H-Merging.run
```

After the generation of events is finished, there will be a `yoda` file (i.e., `LHC-H-Merging.yoda`). One can merge `yoda` files with different random seeds to improve statistics via

```
$ yodamerge -o LHC-final.yoda LHC-1.yoda LHC-2.yoda
```

where `LHC-final.yoda` is the output after merging, `LHC-H-Merging-1.yoda` and `LHC-H-Merging-2.yoda` are intermediate `yoda` file with different random seeds.

The `LHC-Matchbox.in` file and `LHC-H-Merging.in` file is used as the input file for HERWIG 7 event generator. In this study, `LHC-Matchbox.in` is used as the input for $h(2^\star)$ fixed order calculation and $h(2^\star) \bigoplus \text{PS}$, while the `LHC-H-Merging.in` is used for the merged setup, i.e. $h(2^\star, 3)$ and $h(2^\star, 3^\star, 4)$. An example input file `LHC-H-Merging.in` for the calculation of $h(2^\star, 3^\star, 4)$ at 13 TeV is shown in the following. All the input files used in this dissertation and the `VBFNLO` code I developed are in the GitHub repository: "Anomalous Higgs Boson Couplings".

HERWIG 7 adds a new feature to help reduce the running time for merged setup by dividing the event generation process into chunks. Using this feature, for example, I can set up 5 chunks for the $h(2^\star, 3^\star, 4)$ process and then run event generation jobs in parallel based on different chunks. This can reduce the running time for a single event generation run. Then I can add the chunk results to get the final results. For the estimation of the running time on HPC (based on the single CPU core and 2 GB memory) of the merged setup $h(2^\star, 3^\star, 4)$, it takes about 5 hours to generate $1,000,000$ events. In order to have good statistics for $h(2^\star, 3^\star, 4)$ runs, I have generated $8,000,000$ events for 250 individual runs with different random seeds for each chunk. And I divided the event generation into 10 chunks. For the merged setup $h(2^\star, 3)$, it takes about 3.5 hours to generate $1,000,000$ events. I have executed 200 parallel runs, each generating $10,000,000$ events, and divided the process into 5 chunks. For the matched setup $h(2^\star) \bigoplus \text{PS}$, the running time for one million events is about 1.5 hours, and I execute 200 runs with $10,000,000$ events for each run.

In order to use the `VBFNLO` for matrix elements and read input for parameters for anomalous couplings, `anom_HVV.dat` is also needed in the working directory. An example of setting CP-even and CP-odd couplings is shown below. In this example, I only show one part of the file, which is the parameterization I used in the dissertation, and the complete file can be found on GitHub. I used the first parameterization, and set $g_{5e}^{HWW} = g_{5e}^{HZZ} = g_{5o}^{HWW} = g_{5o}^{HZZ} = 0.5$.

```
------------------------------set anomalous HVV couplings
------------------------------Parametrisation: Phys. Lett. B591, 297
PARAMETR1  = .true.    ! switch for this parametrisation;
!on(=.true.) or off(=.false.)
LAMBDA5    = 480.0d0   !lambda5
G5E_HWW    = 0.5d0     ! g5e_hww, CP-even
G5E_HZZ    = 0.5d0     ! g5e_hzz
G5E_HGG    = 0.0d0     ! g5e_hgg
G5E_HGZ    = 0.0d0     ! g5e_hgz
G5O_HWW    = 0.5d0     ! g5o_hww, CP-odd
G5O_HZZ    = 0.5d0     ! g5o_hzz
G5O_HGG    = 0.0d0     ! g5o_hgg
G5O_HGZ    = 0.0d0     ! g5o_hgz
```